TAMPERE UNIVERSITY OF TECHNOLOGY

MATTI MARJANEN

DESIGN AND IMPLEMENTATION OF AN INDUCTION MOTOR DRIVE TEST BENCH

Master of Science thesis

Examiner: Prof. Teuvo Suntio
The examiner and the topic were approved in the Faculty of Computing and Electrical Engineering Council meeting on 3.6.2015

TIIVISTELMÄ

TAMPEREEN TEKNILLINEN YLIOPISTO
Sähkötekniikan koulutusohjelma
Marjanen, Matti: Oikosulkumoottorikäytön testipenkin suunnittelu ja rakennus
Diplomityö, 70 sivua, 31 liitesivua
Elokuu 2015
Pääaine: Tehoelektroniikka
Tarkastajat: Prof. Teuvo Suntio
Avainsanat: oikosulkumoottorkäyttö, vektoriohjaus, sähkömoottorikäytön testipenkki, dSPACE

Tehopuolijohteiden nopea kehitys viime vuosikymmenien aikana on mahdollistanut myös sähkömoottorikäyttöjen nopean kehityksen. Nykyinen taajuusmuuttajateknologia mahdollistaa oikosulkumoottoreiden nopean ja tarkan säädön, mikä ei ole ollut mahdollista ennen taajuusmuuttajia. Tämän takia halpa ja käyttövarma oikosulkumoottori taajuusmuuttajalla ohjattuna on korvannut monissa teollisuuden sovelluksissa kalliimman ja enemmän huoltoa vaativan tasasähkömoottorin. Tämän vuoksi tehoelektroniikan opintoihin keskittyvien sähkötekniikan diplomi-insinöörien on tärkeää tuntea oikosulkumoottorikäyttöihin liittyvät ilmiöt.

Tällä hetkellä Tampereen teknillisen yliopiston Sähkötekniikan laitoksella on valittavana useita sähkömoottorikäyttöihin liittyviä kursseja. Sähkömoottorikäytön mallinnukseen keskittyvällä kurssilla oli tarvetta kehittää tehtävän harjoitustyön sisältöä käytännönläheisempään suuntaan. Tätä varten oli suunniteltu rakennettavaksi oikosulkumoottorikäytön testaukseen tarkoitettu testipenkki. Tämän työn aiheena on kyseisen testipenkin suunnittelu sekä rakennus.

Kyseinen testipenkki suunniteltiin käyttäen dSPACE laitteistoa, joka on tarkoitettu säätöjärjestelmien prototyyppien nopeaan testaukseen ja simulointiin. Tämä laitteisto käyttää Matlab Simulink ympäristöä mallien rakentamiseen ja juuri tämän takia se on erityisen hyödyllinen myös opetuskäytössä. Moottoreiksi valittiin kaksi 2.2kW oikosulkumoottoria ja kaupalliset taajuusmuuttajat hankittiin pääosin turvallisuussyistä. Nämä muodostivat testipenkin rungon. Lisäksi useita mittapiirejä sekä muita antureita rakennettiin sekä ostettiin.

Testipenkin rakennuksen loppuvaiheessa mittauspiirien toimintaa verifioitiin ensin käyttämällä moottoreita takaisinkytkemättömällä ohjausjärjestelmällä ja tarpeelliset muutokset tehtiin piireihin ja malliin. Tämän jälkeen suora oikosulkumoottorin vektorisäätö toteutettiin ja testipenkin takaisinkytketyn ohjauksen toiminta testattiin.

ABSTRACT

TAMPERE UNIVERSITY OF TECHNOLOGY
Master's Degree Programme in Electrical Engineering
MARJANEN, MATTI : Design and implementation of an induction motor drive test bench
Master of Science Thesis, 70 pages, 31 Appendix pages
August 2015
Major: Power Electronics
Examiner: Prof. Teuvo Suntio
Keywords: induction motor, vector control, field oriented control, electric motor test bench, dSPACE

Fast development of power electronics components in recent decades has enabled improvements also in electric drives technology. Present inverter technology has made it possible to accurately control an induction motor, which has previously been complicated. Therefore, inexpensive, robust and low-maintenance induction motors supplied with inverters have replaced more expensive and complicated motors in many industrial applications. Thus, it is important for power electronics engineers to be familiar with the control and phenomena of induction motor drives.

Currently, the Department of Electrical Engineering at TUT has a range of courses regarding electric motor drives. However, there was a demand for equipment, which would enable students to verify their model and control of an induction motor drive in practice. This thesis introduces the design and construction of an induction motor test bench for these purposes.

The test bench is based on a dSPACE rapid control prototyping system. This enables the use of Matlab Simulink in model building, which makes it especially beneficial for teaching purposes. Since, modelling and simulation in the courses are conducted in that environment. Two 2.2 kW induction motors were selected as the base of this test bench. Furthermore, commercial converters were purchased to ensure safe operation. In addition to the main hardware, multiple other components had to be purchased or designed and manufactured. These included components such as current measurement circuits, voltage measurement circuits, incremental encoder for speed measurement, torque measurement component and an external power supply for these circuits.

Open-loop control was used to verify the operation of the measurement circuitry after construction of the test bench. Then required modifications were made to improve the measurements. After this, a vector control system was implemented in Simulink, which was then used to verify the closed-loop operation possibilities of the test bench.

PREFACE

This thesis was done in the Department of Electrical Engineering at Tampere University of technology. The thesis was part of a project for developing laboratory equipment for teaching purposes and funded by the Department of Electrical Engineering. The supervisor of the work was M.Sc. Jenni Rekola and examiner Prof. Teuvo Suntio.

I want to thank my supervisor, examiner and the whole power electronics team for the received support and guidance during this work. Furthermore, I want to express my gratitude also to my family, girlfriend and friends for all the support I have received during my studies and the thesis work.

Tampere 22.5.2015

Matti Marjanen
Opiskelijankatu 4 F 342
33720 Tampere

CONTENTS

LIST OF ABBREVIATIONS AND SYMBOLS

ABBREVIATIONS

AC	Alternating current
DAC	Digital-to-analog converter
DC	Direct current
DSP	Digital signal processor
IGBT	Insulated-gate bipolar transistor
IM	Induction motor
PWM	Pulse width modulation
RCP	Rapid control prototyping
RTI	Real time interface
TTL	Transistor-transistor logic
PCB	Printed circuit board

SYMBOLS

$\mathbf{a}$	Unit vector $1\angle 120°$
$\mathbf{a}^2$	Unit vector $1\angle -120°$
f	Frequency [Hz]
I	Current RMS value
i	Current instantaneous value
$\vec{i}$	Current space vector
L	Inductance
I'	Recuded current RMS value
m_a	Amplitude modulation ratio
n	Speed [rpm]

P	Number of poles
p	Number of pair of poles
P	Power
R	Resistance
s	Slip
U	Swiching state vector
U	Voltage RMS value
u	Voltage instantaneous values
$\vec{u}$	Voltage space vector
$\hat{U}$	Voltage amplitude
ω	Speed [rad/s]
ψ	Flux instantaneous value

SUBSCRIPTS

A	Phase A
B	Phase B
C	Phase C
c	Core loss
car	Carrier signal
DC	Dc-bus
LL	Line-to-line value
$L1$	Phase 1
$L2$	Phase 2
$L3$	Phase 3
α	Space vector real component in stationary reference frame

β	Space vector imaginary component in stationary reference frame
0	Space vector zero component in stationary reference frame
x	Stator quantity space vector real component in stator reference frame
y	Stator quantity space vector imaginary component in stator reference frame
u	Rotor quantity space vector real component in stator reference frame
v	Rotor quantity space vector imaginary component in stator reference frame
U	Phase U
V	Phase V
W	Phase W
d	Space vector real component in rotor flux reference frame
q	Space vector imaginary component in rotor flux reference frame
r	Rotor
rl	Rotor loss
$r\sigma$	Rotor leakage
s	Stator
$s\sigma$	Stator leakage
$1an$	Fundamental frequency component

1. INTRODUCTION

Currently electric motors are responsible for majority of the electricity consumption globally. Mid-sized motors ranging from 0.75 kW to 375 kW in output power have the largest share in energy consumption among all electric motors [1]. The largest portion of these are asynchronous motors. Due to high share in electricity consumption, there is also wide potentials for improving electric motor operation and efficiency. One solution for gaining improvements in efficiency is to use variable frequency drives for motor control [1]. Multiple companies in the Finnish industry are focused on this technology. Hence, there are substantial possibilities for power electronics engineers to work at this field after graduation from technical universities. Therefore, it is important to teach engineering students who are focusing on power electronics, the theory and practice behind electric drives.

Currently the Department of Electrical Engineering at Tampere University of Technology has a wide range of available courses regarding electric motor theory and practice. However, there has been a demand for a system that would enable students to investigate and verify the control design of an induction motor in practice. This thesis focuses on designing and building this type of test system for the forthcoming course DEE-34016 Modeling and Control of Electric Drives.

This thesis can be divided into five main chapters. After the introduction, the theory regarding direct vector-controlled induction motor drives is presented in the second chapter. This is carried out by first introducing induction motor structure and theory. Next three-phase AC-AC frequency converter structure and modulation techniques are presented. After this, the next section present the theory regarding vector-control system and introduces the induction motor space vector model. Finally, the system is simulated and results are showed and evaluated.

The third chapter focuses on the construction of the test bench and all of the used components are presented. In the beginning, the main components including the motors, converters and dSPACE control system are introduced. The second section in this chapter is devoted to additional circuitry such as measurement and control circuits. The final part then presents the completed system.

The fourth chapter focuses on testing the system functionality by measurements. The obtained measurement results are evaluated and compared with the simulations gained from the theory introduced in the second chapter. The test cases can be

divided into three categories. First, speed response of the system is tested without loading the motor. Next, a load step change is applied to the motor. Finally, the third section tests the motor drive operation during induction motor field weakening region. This part shows that the design and implementation of this test system was successful, but also some parts had to be left for completion in a later time due to tight schedule.

Finally the fifth chapter concludes the thesis. In this chapter a recap of what was done is given and the suitability of this test system for teaching purposes is evaluated. In the end some future views regarding the use of the test bench are presented.

2. INDUCTION MOTOR DRIVE THEORY

This chapter is devoted to the basic concepts of an induction motor drive. The first section covers induction motor theory from the structure of the device to the single phase equivalent circuit model. The second section then covers the basic structure of a three-phase AC-AC frequency converter and the third section introduces the basic modulation techniques used with these converters. Finally, the last section covers the vector controlled induction motor drive model used in the course where this test bench will be employed.

2.1 Induction motor

Currently, induction motor is the workhorse of the industry. It is the most used electric motor type in the industry, since it is relatively cheap and robust. Furthermore, it is even suitable for inflammable work environments such as sawmills and chemical factories. Especially, the development of the converter technology has enabled quite accurate control of the induction motor. Thus making possible the utilization of induction motor even in applications which require accurate speed control. This section describes the working principles, structures and steady-state equivalent circuit of an induction motor.

2.1.1 Induction motor structure

There are two main types of induction motors: a wound rotor induction motor and a cage rotor induction motor. This chapter focuses only on the latter one, because the test bench was implemented with a cage rotor type induction motor. The structure of a cage rotor IM consists of two fundamental parts which are the stator winding and the cage rotor. These parts are shown in Figure 2.1 where part of the induction motor frame and stator has been removed. This reveals the laminated cage rotor connected to the shaft and stator winding surrounding it. Furthermore, additional structures are sometimes added to the design of the motor in order to gain some desired features depending on the application.

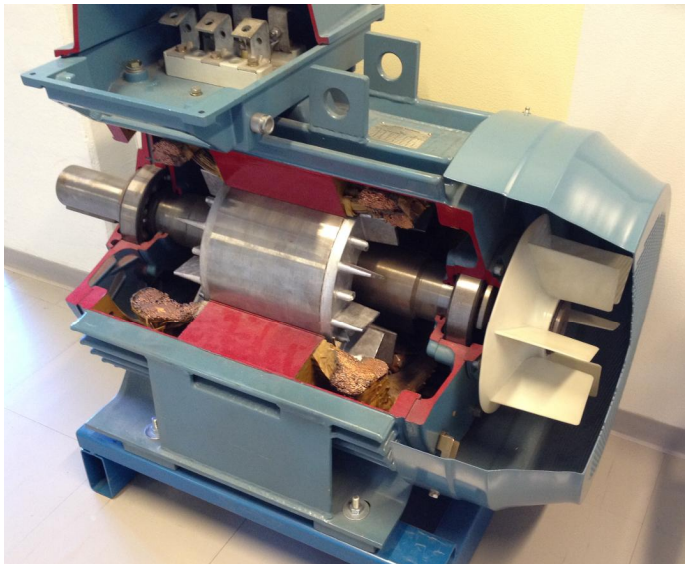

Figure 2.1: Induction motor with frame and stator windings partly removed.

The cage rotor consists of conduction bars made from a conductive material. Usually they are made of aluminium or copper and both ends of the bars are short circuited with shorting rings. The right side in Figure 2.2 illustrates the main structure of the cage used in the rotor.

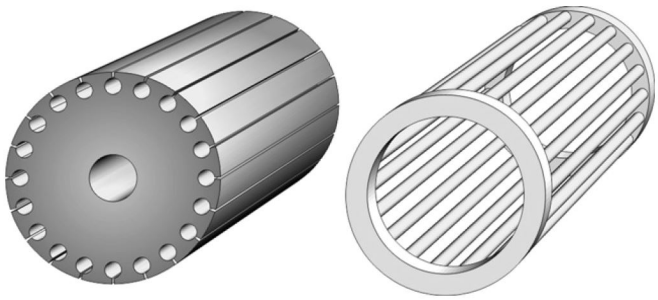

Figure 2.2: The laminated rotor core structure on the left and the rotor cage on the right. [2]

This type of cage is then placed inside a laminated core to minimize magnetic leakage and eddy current losses. Main structure of this laminated rotor core is shown on the left in Figure 2.2. Furthermore, the conduction bars are usually not placed completely parallel to the direction of the shaft, as shown in Figure 2.2, but in a slight angle. This technique is called skewing and it reduces cogging effect that might cause a blocked rotor situation [3]. Furthermore, this technique reduces the magnetic hum and noise produced by the motor. The previously described rotor structure is the most used in the field. However, different variations regarding to the shape and size of the bars are used. Sometimes even a double-cage rotor is used

to gain desired features.

The other main part is the stationary stator. Induction motor stator consists of wound coils. These usually consist of round copper wires or moulded flat copper structures. The coils are placed in a laminated structure as the cage rotor to avoid eddy current losses and to minimize magnetic leakage.

Together the moving rotor and the stationary stator form a magnetic circuit. By applying sinusoidal voltage to the stator windings it is possible to create a rotating magnetic field in the air gap between the stator and the rotor. The rotational speed of the magnetic field is called synchronous speed and defined in (2.1).

$$n_s = \frac{120 f_s}{p}, \tag{2.1}$$

where f_s is the frequency of the voltage applied to the stator and p is the number of poles in the motor. The definition of pole is discussed later on this chapter.

This rotating magnetic field induces voltages to the bars in the cage rotor according to the Faraday's law of induction. Since the bars are short circuited with the shorting rings at both ends, current starts to flow in them. Thus, creating a magnetic field in the rotor bars. However, the sinusoidal current in the rotor lags behind the stator current causing a difference in the two magnetic fields. This induces torque to the rotor bars creating rotational movement of the shaft.

The torque production in an induction motor is based on this difference between the speeds of the stator magnetic field and the rotor magnetic field. Without the difference, the rotor bars would experience a stationary magnetic field and no voltage would be induced to the rotor and therefore, no torque would be produced. Hence, induction motors always rotates slower than the magnetic field induced by the stator windings. This difference is called slip and it is defined in (2.2).

$$s = \frac{n_s - n_r}{n_s} \cdot 100\% = \frac{\omega_s - \omega_r}{\omega_s} \cdot 100\%, \tag{2.2}$$

where n_s is the synchronous speed in rpm, n_r is the actual rotational speed of the motor shaft in rpm, and ω_s and ω_r are rotational speed values in rad/s.

The number of poles defines the number of magnetic poles per one phase in the motor. In a single phase induction motor with a single stator winding, the pole count is two since the sinusoidal voltage applied to the winding generates a rotating magnetic field that has one negative and one positive pole. With a two pole structure one sinusoidal voltage period causes the rotor to spin 360°. When dividing the single stator winding into two, the pole count doubles to four. This causes the rotor to

revolve only 180° in one voltage period. Figure 2.3 represents a principles of the difference between two and four pole single-phase IM.

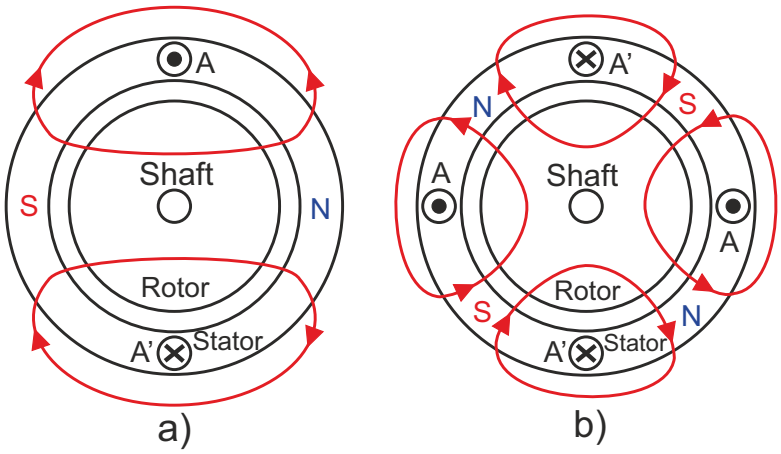

Figure 2.3: Illustration of a single phase two pole motor on the left and single phase four pole motor on the right

The outer ring illustrates the stator and the inner circle the rotor. The circles in the stator illustrate the stator windings where dot means that the current flows out of the page and x means that current flow is into the page. The red lines represent the magnetic field created by the stator current. Red S points south pole of the magnetic field and the blue N the north pole. These figures express only a single moment during the rotation of a motor and in reality the magnetic field is constantly rotating due to the sinusoidal current. Furthermore, all of the parts described and drawn here are greatly simplified. This figure illustrates the working principle of a single-phase motor, but the three-phase motor works similarly. The only difference being the three different stator windings, one for each phase.

2.1.2 Induction motor steady-state model

In order to thoroughly investigate the phenomena of an induction motor, it is important to constitute equivalent circuit model. Induction motor can be considered as a transformer by thinking that the stator is the primary and the rotor is the secondary winding. If the rotor is locked induction motor functions similar to a transformer, but it has an air gap in its magnetic circuit. Due to the air gap between the stator and rotor majority of the magnetic flux is consumed in the gap since permeability of air is remarkably lower compared to the laminated iron core of stator and rotor. However, when considering squirrel cage motor, there is no connectors for the secondary winding, as the squirrel cage is the secondary winding. Hence, the secondary is actually short circuited. Furthermore, when the motor shaft starts to rotate, the

electrical properties of the secondary will change due to changed circumstances. The difference becomes more evident when you compare loads of a transformer and an induction motor. The load of an induction motor is the mechanical counter torque applied to the shaft. Whereas with a transformer it is usually a simple impedance or resistance. The problem that arises is how to convert the mechanical load to correspond to an electrical load. This might seem as a problematic question. However, a relation between slip and rotor resistance has been recognized. When considering all matters above, the per-phase equivalent circuit of a three-phase induction motor can be constituted as shown in Figure 2.4.

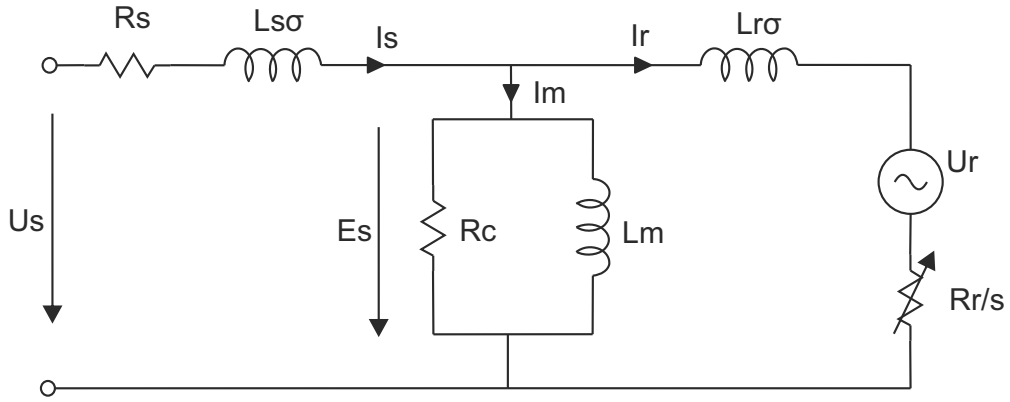

Figure 2.4: Induction motor per-phase steady-state equivalent circuit.

In Figure 2.4, R_s is stator resistance and $L_{s\sigma}$ is stator leakage inductance. These terms illustrate the electrical properties of the stator windings. The parallel term R_c is used to describe the core losses that occur in the laminated iron core. Whereas L_m is magnetization inductance. I_m is the magnetization current drawn from the supply at no-load situation to magnetize the motor. $L_{r\sigma}$ is rotor leakage inductance and term R_r is rotor resistance. In practice all of these values for the induction motor equivalent circuit are calculated using no-load and blocked rotor test measurements [4]. Furthermore, the term U_r denotes the counter voltage created by the induced rotor flux.

The resistance value R_r/s changes according to the slip. Hence, the greater the slip is the higher current is drawn into the rotor resulting in greater produced power [2]. This can be considered with two extreme conditions s=1 and s=0. The first corresponds to condition where rotor is not rotating and term R_r/s is equal to rotor resistance, which is low due to well conducting squirrel cage bars. This situation results in high current at the rotor side and also at the stator side where the current is drawn from. Hence, high power is injected to the shaft. The other condition where s=0 corresponds to a situation where shaft is rotating at synchronous

speed. In reality this is not possible, since induction motor requires slip to magnetize the rotor. However, during no-load situation rotational speed is quite close to synchronous speed and during this the slip can be considered as zero. This results in a situation where term R_r/s goes to infinity and current in the rotor reduces close to zero. The only current drawn from the supply in this situation is due to magnetization and core-losses. Thus, the power injected to the shaft is near zero and only the power required to magnetization and to overcome friction is taken from the source.

The term R_r/s is normally divided into two different terms. The first is R_r and describes the rotor losses due to resistance of rotor bars. The second is $(R_r(1 - s))/s$ and it describes the actual mechanical power of the motor shaft. Using this equivalent circuit it is possible to calculate mechanical power injected to the shaft. First, either the rotor variables need to be reduced into stator or vice versa using the transformation ratio between stator and rotor. After this the power transferred through the air gap in a three-phase motor can be calculated using (2.3) [4].

$$P_r = 3I_r'^2 \frac{R_r'}{s}, \tag{2.3}$$

where rotor variables are reduced to stator and described with prime. After this the losses in the rotor can be calculated by means of (2.4).

$$P_{rl} = 3I_r'^2 R_r' \tag{2.4}$$

Using these two equations, the resulting electromechanical power can be calculated using (2.5).

$$P_M = P_r - P_{rl} = 3I_r'^2 \frac{1-s}{s} R_r' \tag{2.5}$$

These equations can be used when motor is examined from the stator side. Furthermore, this model applies to induction motor only during the steady-state operation and further development is required when dynamic behaviour is examined. The derivation of this is done later in this thesis during the examination of vector control system. This concludes the review of induction motor theory and next section is devoted for frequency converter.

2.2 Three-phase AC-AC frequency converter

Frequency converter is required to control the speed of an AC motor. Main function for an AC-AC frequency converter is to rectify grid voltage and after that form the desired AC waveforms for the motor. There are wide variety of differently implemented AC-AC frequency converters and multiple topologies exist. However, in this section we consider one basic and most common topology that is also utilized in this test bench.

This topology consists of two active three-phase two-level converters and a capacitor in the DC side. Both of them may operate as rectifier or inverter depending on the operation region of the motor. However, in the default situation the grid side converter operates as a rectifier supplying power to the DC-bus and the motor side bridge works as an inverter supplying power for the rotating motor. The power flow is reversed during the dynamic braking situations and these converters change their operation to opposite.

Figure 2.5 illustrates the fundamental circuit diagram of a considered AC-AC converter. In addition to the three-phase IGBT bridges, L- or LCL-type filter has to be inserted at the grid side to decrease the disturbances in the currents caused by high frequency switching. Filter is not required at the motor side since the motor has inductive and resistive properties as the previous section induction model described.

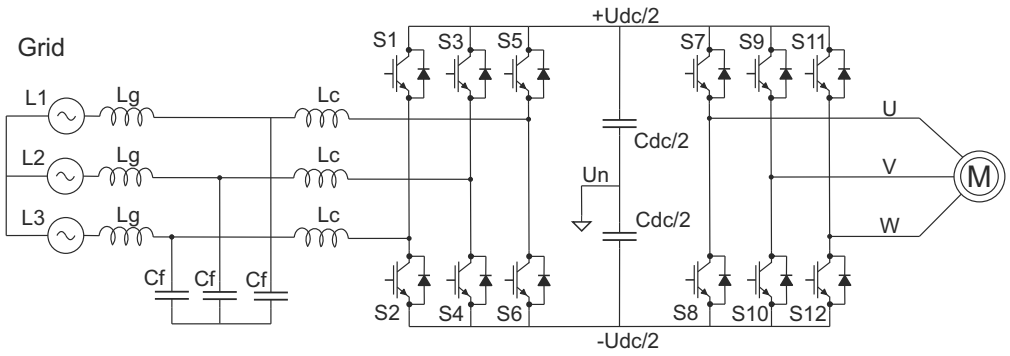

Figure 2.5: Three-phase two-level AC-AC frequency converter with active grid side bridge and LCL-filter.

Both the grid-side and motor-side converters can be controlled by different pulse width modulation (PWM) techniques. There are multiple different PWM schemes and two of the most common of these are described next.

The first and most frequently used method is the carrier based PWM. In this scheme, each of the sinusoidal three-phase reference voltage signals are compared to

a triangular carrier signal that has considerably greater frequency than the reference signal. This is the switching frequency of the semiconductors. Figure 2.6 illustrates this operation principle. Figure 2.6 (a) shows the three-phase reference signals for each phase V_{ca}, V_{cb} and V_{cc} where the subscript c refers to control. They are displayed in the same figure with carrier signal V_{Δ}. Figures 2.6 (b) and (c) then illustrate the produced PWM output voltage for phases a and b respectively. Finally, Figure 2.6 (d) shows the resulting ab line-to-line voltage with fundamental component V_{o1}.

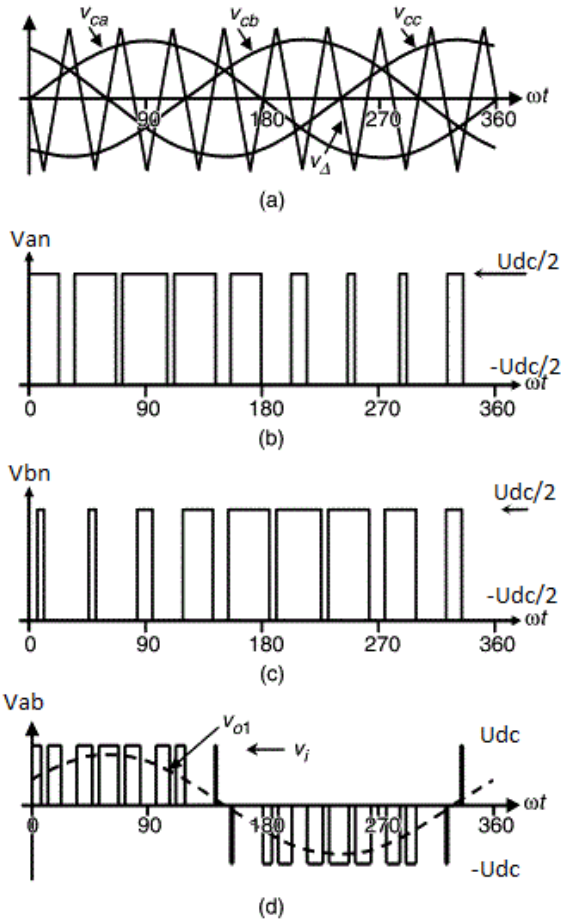

Figure 2.6: Three-phase carrier based PWM waveforms [5].

When the reference signal is greater than the carrier, the upper switch in that phase leg is conducting and the lower is switched off. This way the positive voltage of the DC bus is seen in the AC side. When the reference drops below the carrier signal, opposite switching happens and the negative DC bus voltage is seen on the AC side. The resulting line-to-line waveforms are PWM and they contain harmonic components in addition to the desired fundamental waveform. The spectrum can be calculated using Fourier transform.

Amplitude of the fundamental wave can be changed by varying the amplitude of the reference wave. The relation between the amplitudes of the carrier and reference

waves is called amplitude modulation ratio and usually denoted by m_a. It can be calculated using (2.6).

$$m_a = \frac{\hat{U}_{ref}}{\hat{U}_{car}}, \tag{2.6}$$

where $\hat{V}_{ref}$ is amplitude of the sinusoidal reference and $\hat{V}_{car}$ is amplitude of the triangular carrier wave. When m_a is between 0 and 1.0 the converter is said to be in linear modulation region. This refers to the fact that amplitude of the fundamental frequency wave varies linearly with respect to the amplitude modulation ratio. Amplitude of the fundamental frequency component of the output voltage during the linear modulation region can be calculated using (2.7)

$$\hat{U}_{1an} = m_a \frac{U_{dc}}{2}, \tag{2.7}$$

where U_{dc} is the DC-bus voltage and $\hat{U}_{1an}$ is the amplitude of the produced line voltage fundamental frequency component. This produces line-to-line rms voltage at the fundamental frequency given by (2.8).

$$U_{LL1} = \frac{\sqrt{3}}{\sqrt{2}} U_{1an} = \frac{\sqrt{3}}{2\sqrt{2}} m_a U_{dc} \approx 0.612 m_a U_{dc} \tag{2.8}$$

However, this equation applies only at the linear modulation region. The region when m_a is greater than 1.0 is called over modulation region. The maximum rms line-to-line voltage of the fundamental wave at this region is approximately $0.78U_{dc}$ when the modulation ration is so high that converter switches to square wave operation. However, in this region the harmonic content of the voltage increases substantially. There are also ways to improve the voltage waveforms at the linear region, but those are not discussed in this section.

Another widely used three-phase converter modulation technique is space vector modulation. In this method, the symmetrical three-phase voltage references are first transformed into a single complex space-vector. This transformation is conducted using the Clarke's transformation method introduced in (2.9) where u_A, u_B and u_C are the phase voltages and $\mathbf{u}$ is the generated reference space vector.

$$\mathbf{u} = \begin{bmatrix} u_\alpha \\ u_\beta \\ u_0 \end{bmatrix} = \frac{2}{3} \begin{bmatrix} 1 & -\frac{1}{2} & -\frac{1}{2} \\ 0 & \frac{\sqrt{3}}{2} & -\frac{\sqrt{3}}{2} \\ \frac{1}{2} & \frac{1}{2} & \frac{1}{2} \end{bmatrix} \begin{bmatrix} u_A \\ u_B \\ u_C \end{bmatrix} \tag{2.9}$$

This space vector has three different parts called α, β and zero components. However, it can be assumed that in this situation the phase voltage references must be symmetrical, which leads to a form where the zero component is cancelled out and only u_α and u_β remain. This cancellation occurs only with symmetrical voltages quantities. The resulting form is shown in 2.10.

$$\mathbf{u} = \begin{bmatrix} u_\alpha \\ u_\beta \end{bmatrix} = \frac{2}{3} \begin{bmatrix} 1 & -\frac{1}{2} & -\frac{1}{2} \\ 0 & \frac{\sqrt{3}}{2} & -\frac{\sqrt{3}}{2} \end{bmatrix} \begin{bmatrix} u_A \\ u_B \\ u_C \end{bmatrix} \tag{2.10}$$

This can be also changed to a form given in (2.11)

$$\mathbf{u} = \frac{2}{3}(u_A + \mathbf{a}u_B + \mathbf{a}^2 u_C) \tag{2.11}$$

$$\mathbf{a} = e^{j\frac{2}{3}\pi} = 1\angle 120°$$

$$\mathbf{a}^2 = e^{-j\frac{2}{3}\pi} = 1\angle -120°,$$

where $\mathbf{a}$ is the unit vector at an angle of 120° and $\mathbf{a}^2$ the unit vector at an angle of -120°. After the three-phase voltage references have been transformed into single vector, next task is to define all different switching states that can be achieved with a two level three-phase converter. These switching combinations apply only with a two-level converter because other multi-level topologies have more states. There are eight different combinations altogether with this topology since only one switch on each leg can conduct at one time. Otherwise the switches would short circuit the DC-bus. These different states produce eight voltage vectors at AC side terminals. As can be seen from Figure 2.5, each leg can produce Udc/2 or -Udc/2 phase voltage at the AC-side. With this knowledge it is possible to define a switching vector for each of these eight states also by (2.12) [12].

$$\mathbf{U} = \frac{2}{3}(S_{12} + S_{34}e^{j\frac{2}{3}\pi} + S_{56}e^{-j\frac{2}{3}\pi}) \tag{2.12}$$

where S_{12}, S_{34} and S_{56} define which switch in each leg is conducting. Thus, the value of each of these is either 1 when upper switch is conducting or 0 when lower is conducting. The subscripts refer to the legs of the grid side bridge in Figure 2.5. Equation (2.12) is then used to calculate all the different vectors given in Table 2.1, where the conduction states of each of the three legs are presented as stated above. Hence, six active vectors and two zero vectors are produced.

Table 2.1: All switching states of two-level three-phase converter.

Vector	S_{12}	S_{12}	S_{12}	Produced vector
$\mathbf{U}_0$	0	0	0	0
$\mathbf{U}_1$	1	0	0	$\frac{2}{3}U_{dc}$
$\mathbf{U}_2$	1	1	0	$\frac{2}{3}U_{dc}e^{j\frac{1}{3}\pi}$
$\mathbf{U}_3$	0	1	0	$\frac{2}{3}U_{dc}e^{j\frac{2}{3}\pi}$
$\mathbf{U}_4$	0	1	1	$\frac{2}{3}U_{dc}e^{j\pi}$
$\mathbf{U}_5$	0	0	1	$\frac{2}{3}U_{dc}e^{j\frac{4}{3}\pi}$
$\mathbf{U}_5$	1	0	1	$\frac{2}{3}U_{dc}e^{j\frac{5}{3}\pi}$
$\mathbf{U}_7$	1	1	1	0

All of these vectors are then illustrated with an example reference vector in a complex plane in Figure 2.7. It can be noticed that these vectors form six different sectors on the $\alpha\beta$-plain, which are used to define the required state vectors during the modulation.

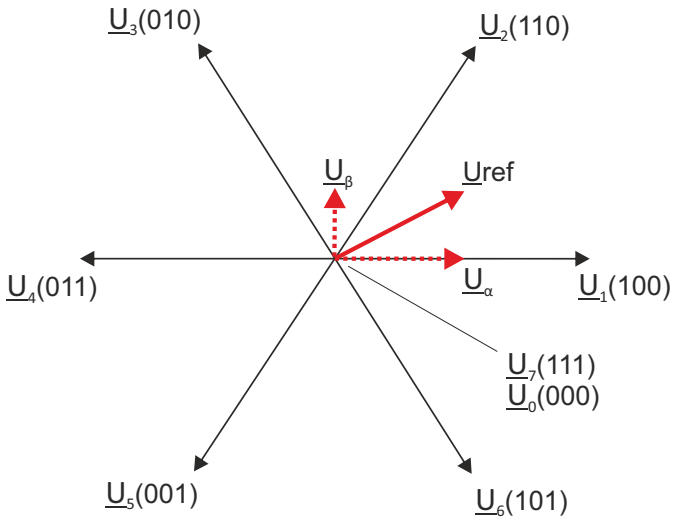

Figure 2.7: Two-level three-phase converter switching vectors.

Now all of these eight vectors can be used to produce the desired voltage according to the reference. This is executed first by defining in which sector the reference vector is located. The state vectors located at the sides of this sector are then used in modulation. For instance $\mathbf{U}_0$, $\mathbf{U}_1$ and $\mathbf{U}_2$ would be used to form the reference vector seen in Figure 2.7 since it is located in the first sector. Finally the durations for each switching vector are defined using volt-second balance over one switching

cycle [12]. Thus, the desired voltage at the output is achieved.

This section introduced a short introduction to one AC-AC frequency converter topology and to two fundamental converter modulation techniques. There are multiple variations of these and also completely different modulation methods and topologies used in this field. However, the purpose for this section was not to introduce novel strategies or compare used ones, but to give an overview to the fundamentals of AC-AC converters since they are the most vital element in AC-drives.

2.3 Induction motor vector control

Vector control of an electric motor was initially developed in Germany by Blaschke, Hasse and Leonhard in 1970s for the purpose of improving induction motor control [7] [8]. Currently different control methods based on this are used in many applications including synchronous and asynchronous electric motors. Also in this thesis a direct vector control method is used. Therefore, this section presents theory required to implement induction motor vector control. First space vector theory is reviewed, which is then followed by introduction to induction motor space vector model and finally control system is presented with results acquired by simulation.

2.3.1 Space vector theory

In induction motor vector control, the three-phase quantities are transformed into a single complex vector in order to ease the mathematical derivation. Hence, it is important to first discuss theory regarding space vectors. The instantaneous three-phase quantities can be given as shown in (2.13)-(2.15). In this derivation, x has been chosen as the variable, but it is replaced with voltage, current or flux during the model construction depending on analysed variable.

$$x_A(t) = \hat{x}\cos(\omega_{sv}t + \phi) = \frac{\hat{x}}{2}(e^{j(\omega_{sv}t+\phi)} + e^{-j(\omega_{sv}t+\phi)}) \tag{2.13}$$

$$x_B(t) = \hat{x}\cos(\omega_{sv}t - \frac{2\pi}{3} + \phi) = \frac{\hat{x}}{2}(\mathbf{a}^2 e^{j(\omega_{sv}t+\phi)} + \mathbf{a}e^{-j(\omega_{sv}t+\phi)}) \tag{2.14}$$

$$x_C(t) = \hat{x}\cos(\omega_{sv}t - \frac{4\pi}{3} + \phi) = \frac{\hat{x}}{2}(\mathbf{a}e^{j(\omega_{sv}t+\phi)} + \mathbf{a}^2 e^{-j(\omega_{sv}t+\phi)}) \tag{2.15}$$

These equations express each of the three-phase instantaneous values at time t. Variable $\hat{x}$ is the amplitude of sinusoidal phase quantity. Using these equations, a space vector presentation can be derived as given in (2.16). In this, the phase shift between different phase quantities has been represented with unit vectors $\mathbf{a} = -1/2 + j\sqrt{3}/2 = 1\angle 120°$ and $\mathbf{a}^2 = -1/2 - j\sqrt{3}/2 = 1\angle -120°$.

$$\frac{2}{3}(x_A(t) + \mathbf{a}x_B(t) + \mathbf{a}^2 x_C(t)) = \hat{x}e^{j(\omega_{sv}t+\phi)} = \vec{x}_{sv}, \tag{2.16}$$

Constant 2/3 is required to obtain amplitude invariant transformation. This transformation results in a space vector rotating at angular speed ω_{sv} on the complex plain. All of this can be also represented in a matrix form introduced originally by E. Clarke as given in (2.17).

$$\vec{x}_{sv} = \begin{bmatrix} x_\alpha(t) \\ x_\beta(t) \\ x_0(t) \end{bmatrix} = \frac{2}{3} \begin{bmatrix} 1 & -\frac{1}{2} & -\frac{1}{2} \\ 0 & \frac{\sqrt{3}}{2} & -\frac{\sqrt{3}}{2} \\ \frac{1}{2} & \frac{1}{2} & \frac{1}{2} \end{bmatrix} \begin{bmatrix} x_A(t) \\ x_B(t) \\ x_C(t) \end{bmatrix} \tag{2.17}$$

Equation 2.17 divides the space vector x_{sv} into three different components called α-, β- and zero-component. However, induction motor quantities can be considered symmetrical due to symmetrical windings in the stator and in the rotor. This assumption results in $x_0 = 0$. This is due to the fact that the sum of three-phase sinusoidal symmetrical components is zero at every moment. This reduces (2.17) to the one shown in (2.18).

$$\vec{x}_{sv} = \begin{bmatrix} x_\alpha(t) \\ x_\beta(t) \end{bmatrix} = \frac{2}{3} \begin{bmatrix} 1 & -\frac{1}{2} & -\frac{1}{2} \\ 0 & \frac{\sqrt{3}}{2} & -\frac{\sqrt{3}}{2} \end{bmatrix} \begin{bmatrix} x_A(t) \\ x_B(t) \\ x_C(t) \end{bmatrix}, \tag{2.18}$$

where the α term is real part and β term imaginary part of the space vector. As noted above, this transformation generates the space vector that rotates at angular frequency ω_{sv} at the stationary complex plain. The reverse transform back to three phase quantities is shown in (2.19).

$$\begin{bmatrix} x_A(t) \\ x_B(t) \\ x_C(t) \end{bmatrix} = \begin{bmatrix} 1 & 0 \\ -\frac{1}{2} & \frac{\sqrt{3}}{2} \\ -\frac{1}{2} & -\frac{\sqrt{3}}{2} \end{bmatrix} \begin{bmatrix} x_\alpha(t) \\ x_\beta(t) \end{bmatrix} \tag{2.19}$$

In some applications, it is required to transform the frame of reference out of the stationary frame into another. This way it is possible to transform sinusoidally alternating α- and β-components to scalar values. Transformation to an arbitrary reference frame with angle θ_k can be performed with (2.20).

$$\vec{x}^k_{sv} = \hat{x}e^{j(\theta-\theta_k)} = \vec{x}e^{-j\theta_k}, \tag{2.20}$$

where $\vec{x}_{sv}^{k}$ is the vector $\vec{x}$ transformed to reference frame k. θ is the angle of the vector $\vec{x}$ and θ_k is the angle of the rotating reference frame. This transformation can also be presented in matrix form with the vector separated into two components x and y by

$$\vec{x}_{sv}^{k} = \begin{bmatrix} x_x(t) \\ x_y(t) \end{bmatrix} = \begin{bmatrix} cos(\theta_k) & sin(\theta_k) \\ -sin(\theta_k) & cos(\theta_k) \end{bmatrix} \begin{bmatrix} x_\alpha(t) \\ x_\beta(t) \end{bmatrix}, \tag{2.21}$$

and the reverse transform back to stationary reference frame by

$$\vec{x}_{sv}^{k} = \begin{bmatrix} x_\alpha(t) \\ x_\beta(t) \end{bmatrix} = \begin{bmatrix} cos(\theta_k) & -sin(\theta_k) \\ sin(\theta_k) & cos(\theta_k) \end{bmatrix} \begin{bmatrix} x_x(t) \\ x_y(t) \end{bmatrix} \tag{2.22}$$

These equations are required to construct the space vector model of an induction motor. The derivation is presented next in this section.

2.3.2 Induction motor space vector model

This section introduces induction motor space vector model that is used to simulate the phenomena and operation of induction motor test bench before actual construction. This model is also used during the course for which this test bench is designed. Hence, for verification purposes the simulations are compared with the results obtained from the actual test system measurements.

In the beginning, some fundamental simplifications are made to ease calculations. First, flux density in the air gap is assumed to be sinusoidally distributed and harmonic components are neglected. Secondly, saturation of stator and rotor as well as iron losses are neglected. Finally, reactances and resistances are assumed to be constant, eventhough, especially, rotor resistance is quite temperature dependent. [8]

The complete derivation has been left out from this section, but it can be found in multiple sources in the literature such as [8] and [9]. Nevertheless, induction motor voltage equations in arbitrary frame of reference rotating at an angular velocity ω_k are represented in (2.23) and (2.24).

$$\vec{u}_s^{k} = R_s\vec{i}_s^{k} + \frac{d\vec{\psi}_s^{k}}{dt} + j\omega_k\vec{\psi}_s^{k} \tag{2.23}$$

$$\vec{u}_r^{k} = R_s\vec{i}_r^{k} + \frac{d\vec{\psi}_r^{k}}{dt} + j(\omega_k - \omega_r)\vec{\psi}_r^{k}, \tag{2.24}$$

where superscript k denotes the frame of reference, subscript s refers to stator and r to rotor quantities as well as R denotes resistances of stator and rotor. Furthermore,

$\vec{\psi}$ is flux vector, $\vec{i}$ is current vector, ω_k and ω_r are rotational velocities of reference frame k and rotor respectively. Equations (2.25) and (2.26) represent flux equations also in arbitrary reference frame k.

$$\vec{\psi}_s^k = L_s\vec{i}_s^k + L_m\vec{i}_r^k \tag{2.25}$$

$$\vec{\psi}_r^k = L_r\vec{i}_r^k + L_m\vec{i}_s^k, \tag{2.26}$$

where L_s is the self-inductance of the stator, L_r the self-inductance of the rotor and L_m the magnetizing inductance. These inductances can be calculated using (2.27) and (2.28).

$$L_s = L_{s\sigma} + L_m \tag{2.27}$$

$$L_r = L_{r\sigma} + L_m, \tag{2.28}$$

where L_m is magnetization inductance, $L_{s\sigma}$ stator leakage inductance and $L_{r\sigma}$ rotor leakage inductance, which were introduced previously in the induction motor theory part. The instantaneous active power consumed by the induction motor can be expressed in vector form with (2.29). However, this power expression assumes symmetrical three-phase quantities.

$$p = \frac{2}{3}(\vec{u}_s\vec{i}_s^*), \tag{2.29}$$

where $\vec{u}_s$ is stator voltage vector and $\vec{i}_s^*$ is complex conjugate of stator current vector. Using (2.23)-(2.28), an induction motor space-vector per phase equivalent circuit in reference frame k can be drawn. This is shown in Figure 2.8.

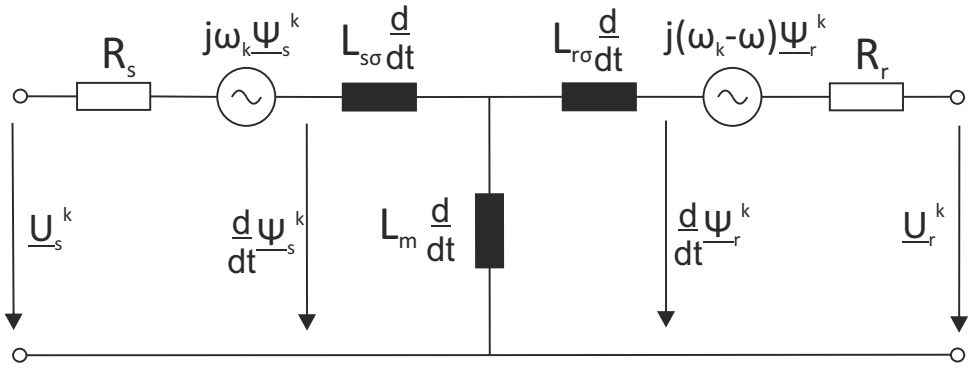

Figure 2.8: Induction motor space vector model.

This model is primarily built to study dynamic behaviour of an induction motor equipped with three-phase rotor winding. However, this also applies to a single squirrel cage IM with certain inaccuracy [9]. Furthermore, the assumptions made in the beginning of this section introduce some inaccuracies in the modelling. A model based on the equations introduced in this section was constructed in Simulink. Appendix A presents the derivation of the necessary equations and figures on the constructed Simulink model more thoroughly. After this, the vector control system was designed for the induction motor model which is discussed in the next section.

2.3.3 Vector control system

Previously DC motors have dominated variable frequency drive industry due to their extremely simple control possibilities. The produced electromagnetic torque of a DC motor can be expressed with a relatively simple equation by

$$t_{edc} = ci_f i_a = c_1 \psi_f i_a, \tag{2.30}$$

where the motion of the rotor can simply be changed by controlling torque-producing armature current i_a or flux-producing current i_f. Parameters c and c_1 are constants which are defined according to the motor. Furthermore, these components are scalar type, thus control can be implemented with a simple system. However, one major disadvantage with DC motors is their complicated structure with commutator and multiple compensation windings.

Control of a squirrel-cage induction motor is far more complicated compared to a DC motor. Difficulties in monitoring currents and flux of the rotor would complicate the control. Furthermore, flux produced by the stator is revolving which further complicates the control design [8]. However, the mechanical torque production phenomenon of an induction motor does not greatly differ from the one in DC motor. It is possible to define the components of induction motor currents which are responsible for flux-production and torque-production. This requires modelling the induction motor using space-vector theory. By extracting these two different components, it is possible to control separately the torque-producing component and flux-producing component. Hence, the control becomes faster and more precise. The induction motor instantaneous electromotive torque relation in phase-vector form is shown in (2.31).

$$t_e = \frac{2}{3} p \vec{\psi}_s \times \vec{i}_s \tag{2.31}$$

where $\vec{\psi}_s$ is the stator flux vector, $\vec{i}_s$ the stator current vector and p is the number

of pair of poles. The torque equation is not dependent on the frame of reference but it is the same in everyone. This torque equation can also be presented in component form in different reference frames shown in (2.32) and (2.33).

$$t_e = \frac{2}{3}p(\psi_\alpha i_\beta - \psi_\beta i_\alpha) \tag{2.32}$$

$$t_e = \frac{2}{3}p(\psi_x i_y - \psi_y i_x) \tag{2.33}$$

where α and β denote the stationary reference frame, and x and y the rotor flux reference frame.

Previously induction motors were mostly controlled by U/f-control in which the frequency and voltage amplitude are increased or decreased keeping the relation between these two constant [8]. However, this control method is inaccurate and slow [8]. The developing of vector control started in 1970s but, since it requires more computational capacity, it actually could be used only after the development of microcontrollers and integrated circuits. Currently, the calculation process of a vector control system raises no problems with present-day processing powers of microcontrollers and DSPs.

There are multiple different vector control system implementations for induction motor drive purposes. The main difference between these implementations is the method how magnetic flux amplitude and angle is defined. In direct vector control, these quantities are calculated with flux model using measured values such as current, voltage and/or rotor angle. Whereas in indirect vector control flux and flux angle are calculated using measured rotor angle and current reference value. This section discusses only the principles of direct voltage based vector control system that uses measured rotor angle and currents to calculate the flux and flux angle. Block diagram of this system is presented in Figure 2.9. In this implementation, motor currents and rotor angle are measured. The measured currents are then transformed into a single current vector using the Clarke transformation method introduced in space-vector theory. This vector has two components: real part i_α and imaginary part i_β. These currents and the rotor angle are then used to calculate flux amplitude and rotor flux angle using flux model. This calculated flux is then used as a feedback for flux controller. Reference for the flux is calculated according to the speed of rotor angle. In practice, the flux amplitude reference is held at a constant value when motor is operated below nominal speed and motor is driven with constant torque. However, when nominal speed is exceeded the motor is shifted to field weakening region and flux reference starts to drop linearly with respect to the speed.

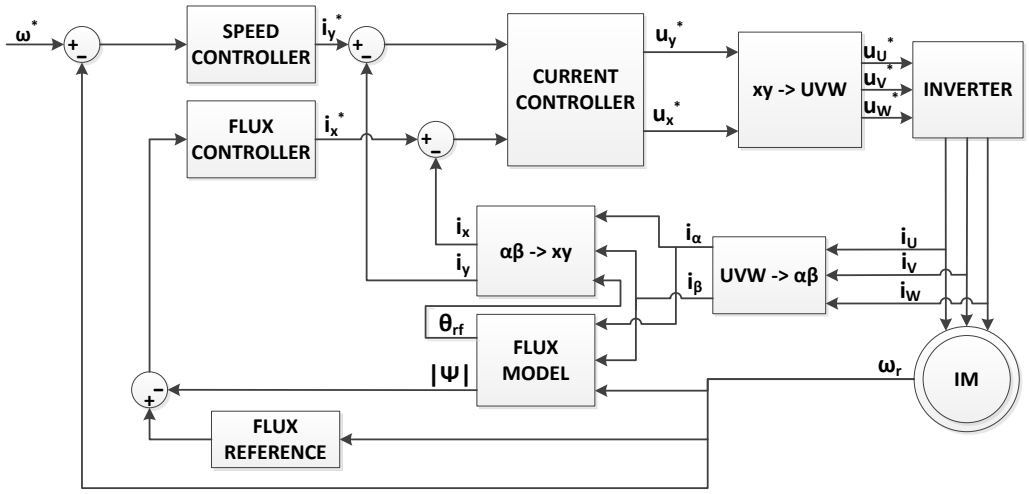

Figure 2.9: Voltage control based direct vector control system block diagram.

In this region, motor is operating with constant power since torque is decreasing with respect to increasing rotational speed. Error between reference and calculated flux is then fed to flux controller which produces reference value for stator current real part in rotor flux reference frame. Speed error is fed to speed controller which produces the stator current imaginary part reference value in rotor flux reference frame. Hence, stator current i_x part is used to control the electromotive torque and this way the rotational speed of the rotor, and i_y part is used to control the stator flux amplitude. The measured currents require transformation to rotor flux reference frame which transforms the sinusoidal α and β currents to scalar values, since rotor flux reference frame is rotating at the same speed as the stator current vector. Finally, the error of both stator current components are fed to current controller which produces the reference voltages. These are then transformed back to three-phase voltages and duty cycles for controlling the converter switches.

The operation of this vector control system was simulated using the induction motor space-vector model introduced in earlier sections. A more thorough derivation of equations regarding the motor model are derived in Appendix A. Also figures and descriptions of the Simulink model are presented in there. The next and final section of this chapter is presenting the simulation results achieved by the constructed model. These were then used as the basis for constructing the real test system.

2.4 Simulation results

This section is devoted to presenting the simulation results obtained with a model which is explained more in detail in Appendix A. Different situations were used to simulate the responses of the system. The response to changing speed reference

and load torque in motor region were tested. Furthermore, tests for operation in field weakening as well as in generator region were conducted. With these types of tests, it was possible to tune the controller parameters to appropriate values in order to achieve the desired responses. The tuning is safer and easier to conduct with simulation, since possible over currents or over speeds with the real system can be avoided. Furthermore, the simulations provide useful information regarding the current and voltage levels and this way eases the design of measurement circuitry. Lastly, the actual test bench control system is constructed using Simulink. Hence, after simulating the behaviour of the drive with a induction motor model, it is easy to replace the model with the real hardware by including real-time measurements from the motor. The device used for this purpose is presented in chapter 3 regarding the building process and the test bench components.

2.4.1 Acceleration and deceleration test

In the first simulation, an acceleration ramp of 1000 rpm/s from speed 0 rpm to 2000 rpm was given as a reference speed and after two seconds of constant speed a deceleration ramp from 2000 rpm to 0 rpm in two seconds was given as reference. During this simulation the motor was not loaded. The speed response of the system is in Figure 2.10 where the red curve is the reference given for the control system and blue is the response of the motor drive. As can be seen from this figure, the control system is able to quite accurately follow the reference speed. Figure 2.11 gives a extended view on the acceleration and deceleration ramps. A small overshoot of approximately 5 rpm is apparent when speed achieves the reference steady-state speed and also some delay at the speed response is visible during the transition between constant speed to deceleration. These simulations give only the response for the speed controller part. Hence, also flux and current controller responses need to be studied.

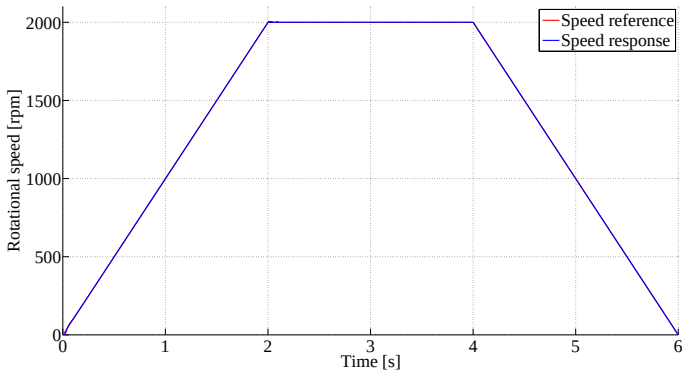

Figure 2.10: Simulated acceleration and deceleration response without motor load.

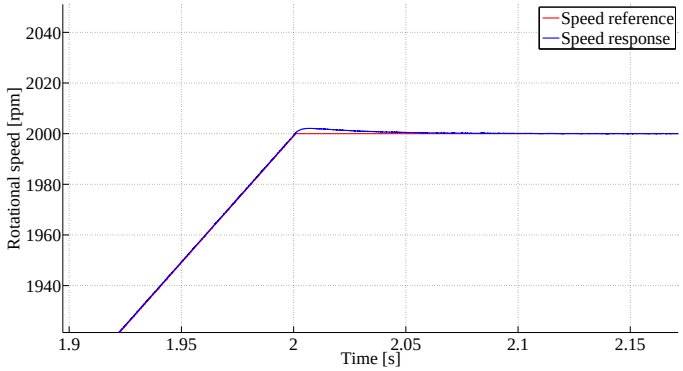

(a)

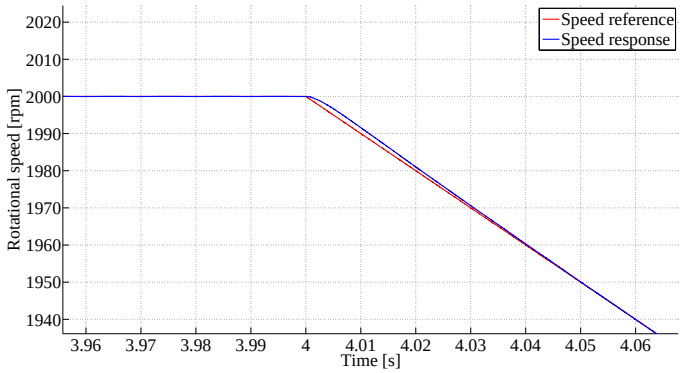

(b)

Figure 2.11: Extended view of the speed response (a) acceleration ramp and (b) deceleration ramp.

Figure 2.12 shows the electromotive torque produced by the motor and the load torque applied to the motor shaft. As can be seen from the figure, the torque during the acceleration is approximately 0.3 Nm and when 2000 rpm constant speed is achieved, the torque stays zero. When the deceleration begins, torque switches to negative compared to the acceleration situation. Red curve shows the load torque which in this simulation was kept at constant zero. There is some oscillation occurring at the electromotive torque and at higher speeds, the oscillation is higher. However, this torque curve is consistent with the speed response seen in the previous figures, since it is positive during the acceleration, zero during the constant speed and negative during the deceleration. This torque curve is achieved by changing the stator current i_{sy} component value. Figure 2.13 shows this current and if it is compared to the torque curve, it is obvious that the produced electromotive torque has a relation with this current.

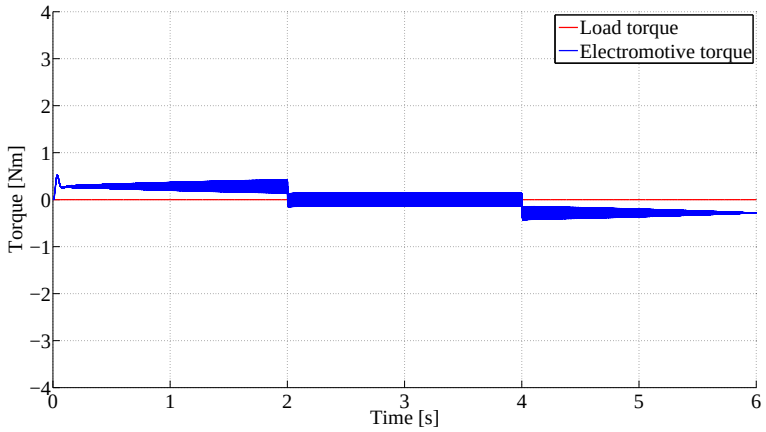

Figure 2.12: Simulated torque during acceleration and deceleration without motor load.

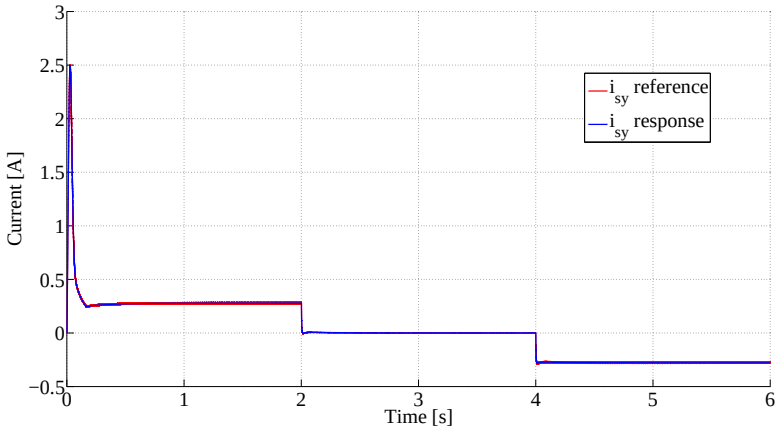

Figure 2.13: Simulated stator current i_{sy} in rotor flux reference frame during acceleration test.

Figures 2.14 and 2.15 show the magnetic flux absolute value and the stator current component that is responsible for creating the magnetization. As can be seen from the flux figure, the magnetization is kept constant while motor operates below nominal speed. In the beginning of the simulation, the flux is increased with a slope to avoid excessively high currents during the start. If the flux would be changed, with an infinite slope step the flux controller would increase the i_{sx} reference greatly and then the fast current controller would create high peaking current. This was discovered to be problematic during the real drive start and the slope had to be added to act as a soft start for the drive. After the flux has been created, the changes in it are quite slow, and since the motor almost always operates below nominal speed, the flux controller is only required to keep the flux constant during the disturbances induced by load changes.

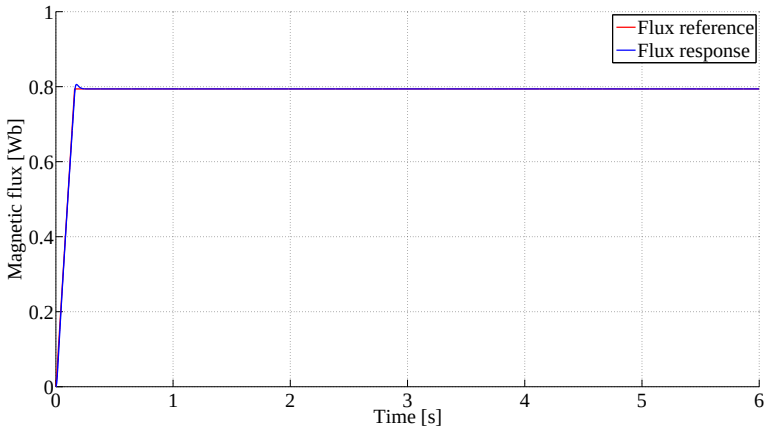

Figure 2.14: Magnetic flux absolute value of the induction motor during acceleration simulation.

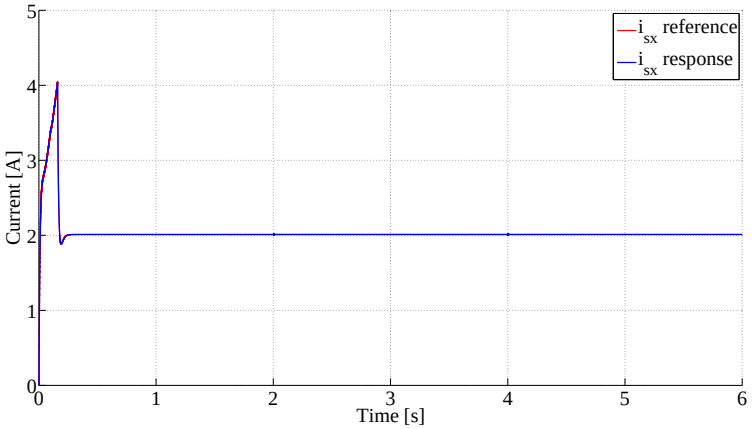

Figure 2.15: Stator current real part in rotor flux reference frame during acceleration simulation.

Figure 2.16 shows the three-phase stator currents during this simulation. It should be noted that the current amplitude in each phase remains constant during the whole simulation apart from the transients in the beginning. In this test, the motor is running without any load, which means that the motor requires current only to magnetization and to overcome the losses induced by resistances of the stator and the rotor windings. Although torque is needed during the acceleration, it is small compared to magnetization as can be seen from Figures 2.13 and 2.15. Hence, the three-phase currents seen in the figure are mainly for magnetization and the acceleration of the motor can be noticed as the increasing frequency of the currents.

This simulation gave information about the no-load behaviour of this system. It was used to verify the operation of the vector control system without disturbances. A ramp type speed reference was given instead of a step change, since the motors

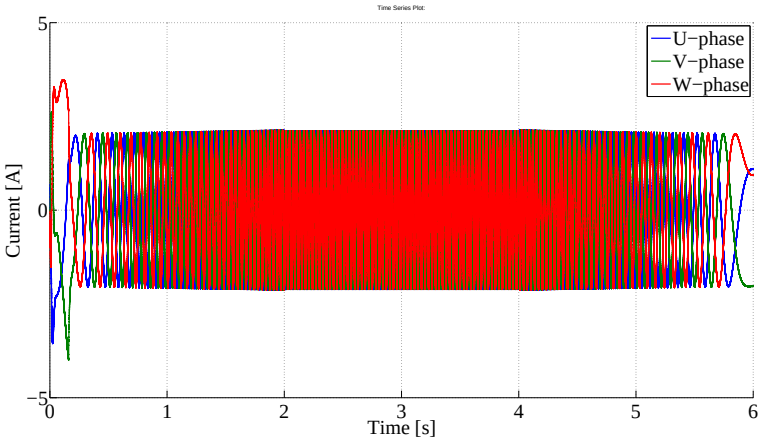

Figure 2.16: Stator three-phase currents during acceleration test simulation.

are generally accelerated with this type of speed references, because step change in speed would stress the mechanical parts such as shafts and other parts of the process system. Furthermore, the currents in the motor would increase drastically during the start up. After this simulation, the response of the drive had to be verified under loaded conditions and this is presented in the next section.

2.4.2 Load torque step change test

In this section, the motor was driven with constant speed of 2000 rpm and first a step change from 0 Nm to 3 Nm was conducted in the load torque. After the system had stabilized, a step from 3 Nm to -3 Nm was made to the load torque. Hence, with the second step the motor changed its state from motor to generator. 3 Nm was selected since it is approximately half of the nominal torque 7.54 Nm of the used motor. Phenomena caused by these load changes were then studied. Figure 2.17 shows the load torque applied to the motor shaft with red and the electromotive torque produced by the motor in blue. Furthermore, Figure 2.18 shows the speed reference and response during these two different load torque steps. The speed figure has been focused to enable a better view on the effects of load torque on the motor speed.

The step at 2 second from 0 to 3 Nm in load torque causes the speed to decrease approximately 23 rpm before the speed controller starts to increase the electromotive torque to achieve the speed reference. After 0.2 seconds the speed is again achieved and there is no error between the reference and the actual value. This predicts that the motor control is able to accurately follow the speed reference even with loaded situations. During the second step at 3 seconds marker the load torque changes direction and steps to -3 Nm. This results that the shaft speed increases

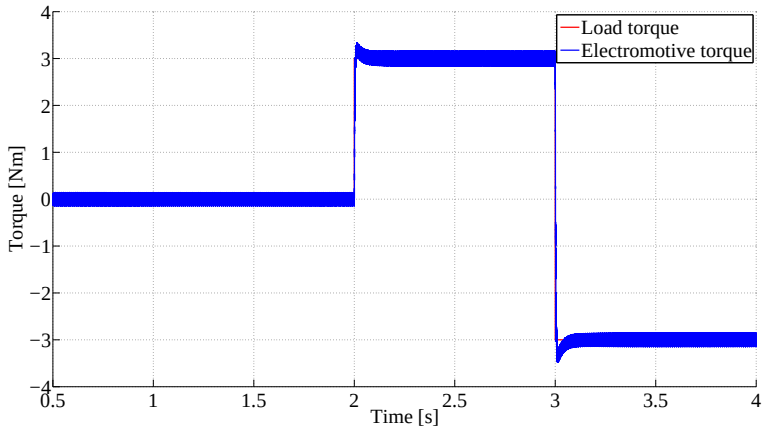

Figure 2.17: Load torque and electromotive torque during simulation.

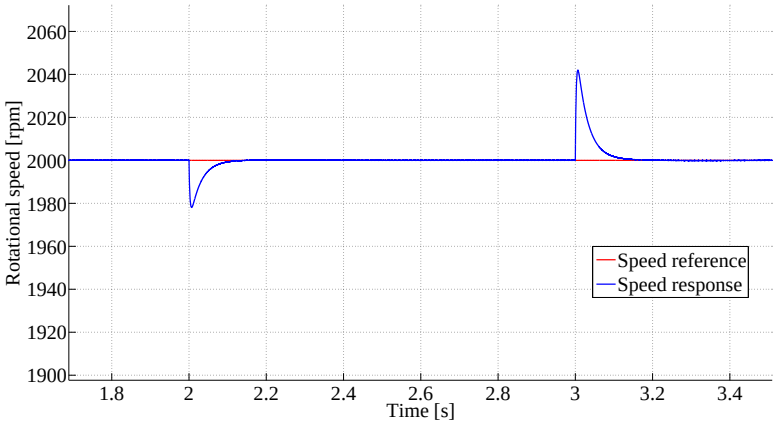

Figure 2.18: Simulated speed response during two step changes in load torque.

to approximately 2043 rpm before the speed controller again achieves the reference value. After this step change the motor is operating as a generator and the power is transferred to frequency converter DC-bus and from there to the grid. Figures 2.19 and 2.20 present the stator currents i_{sy} and i_{sx} in rotor flux reference frame respectively. When current i_{sy} is compared with load, the electromotive torque similarities can be noticed. Hence, it can be stated also in here that torque is controlled with this current component as mentioned in the vector control theory part. It can also be seen, that when motor is operating as a generator, this current component switches its sign compared to motor operation. Even though change in motor torque does not directly affect stator current i_{sx}, small disturbances can be seen in the simulated current waveform because of cross coupling. However, this is only during the load steps, and everywhere else the current is constant due to operating below nominal speed.

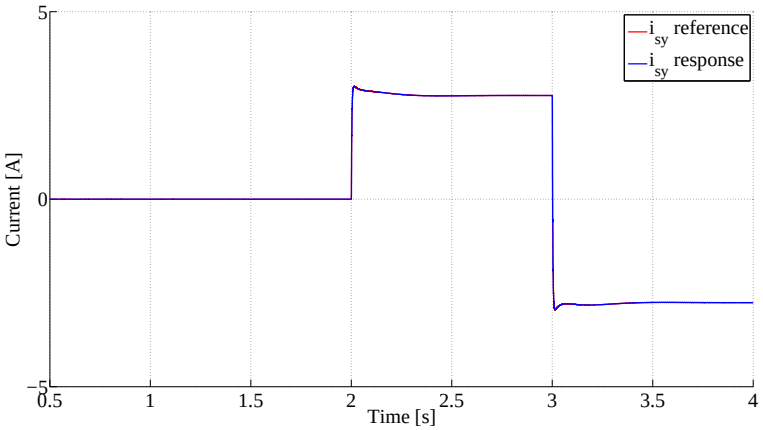

Figure 2.19: Simulated stator current real and imaginary components in rotor flux reference frame.

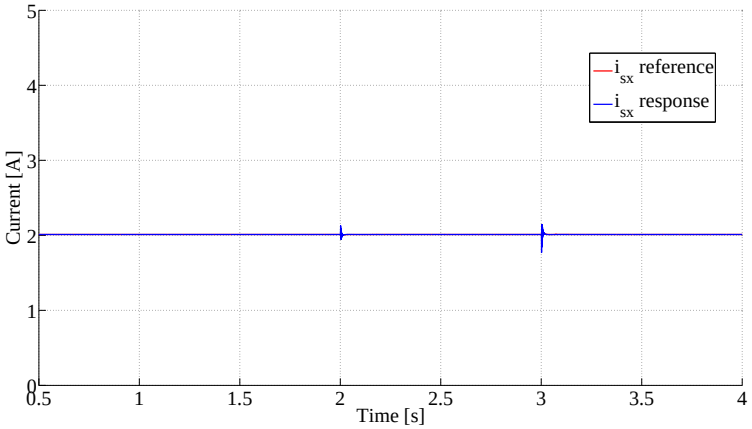

Figure 2.20: Speed response during two step changes in load torque.

The final Figure 2.21 in this section illustrates the simulated three-phase stator currents during the change from loaded motor operation to generator mode. This can be seen from the currents by investigating them at 3 s in the time axis. It can be noted that each of the three-phase currents change their phase by 180° which explains the changed power flow direction.

After this simulation two fundamental phenomena regarding induction motor drives have been studied and simulated. These included the responses for speed reference change and load torque change. The final part is to study the induction motor drive phenomena when the motor speed exceeds the nominal and operation switches to field weakening region. Simulations for this are presented in the next section.

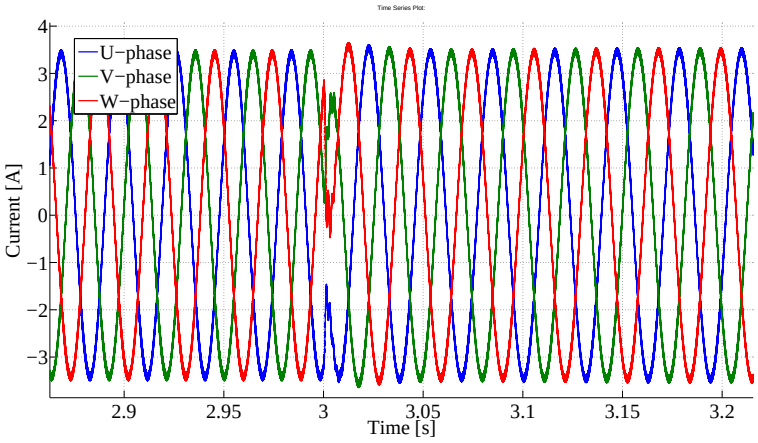

Figure 2.21: Three-phase currents during load torque step from 3 Nm to -3 Nm.

2.4.3 Operation in the field weakening region

In the final simulation, the operation of the motor drive running above nominal speed in the field weakening region of the motor was studied. A acceleration ramp from 0 rpm to 3100 rpm was given as a speed reference for the motor. Slope of this ramp was kept in constant 3000 rpm/s. When the motor had stabilized at 3100 rpm, a torque step of 3 Nm was applied to the motor. Figure 2.22 shows speed reference and response. This indicates that the motor control is working also above nominal speed, since the response is still satisfactory.

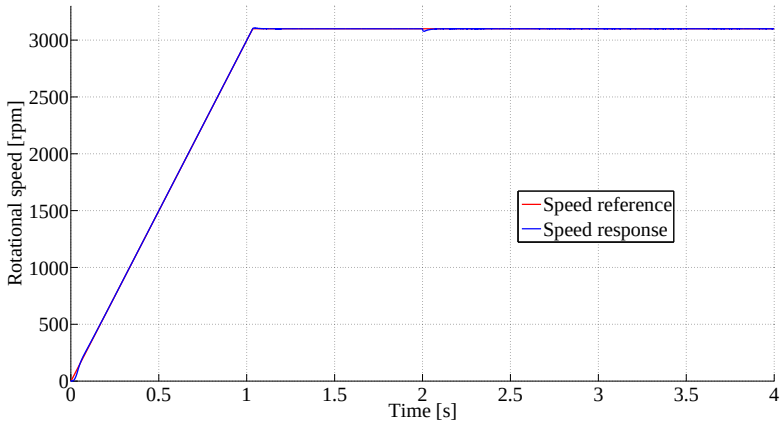

Figure 2.22: Reference speed and response during field weakening operation test.

Next, the electromotive torque together with the applied load torque are shown in Figure 2.23, where the load change is visible from 2 s onwards.

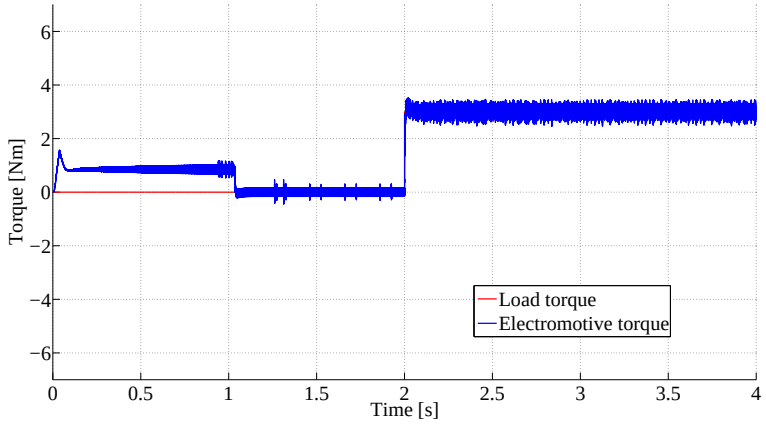

Figure 2.23: Electromotive and load torque during field weakening test simulation.

However, the more important quantities to be studied in this section are the flux and stator current i_{sx} that is responsible in creating it. Hence, Figures 2.24 and 2.25 show the simulated curves for these quantities respectively. As can be seen from these figures, the control system starts to decrease the flux after rotor speed increases above nominal speed of 2875 rpm slightly before 1 s marker. This decrease in flux amplitude is conducted by decreasing the current i_{sx}. This can be seen from Figure 2.25 where the current decreases from 2.0 A to approximately 1.85 A when the motor speed is at 3100 rpm.

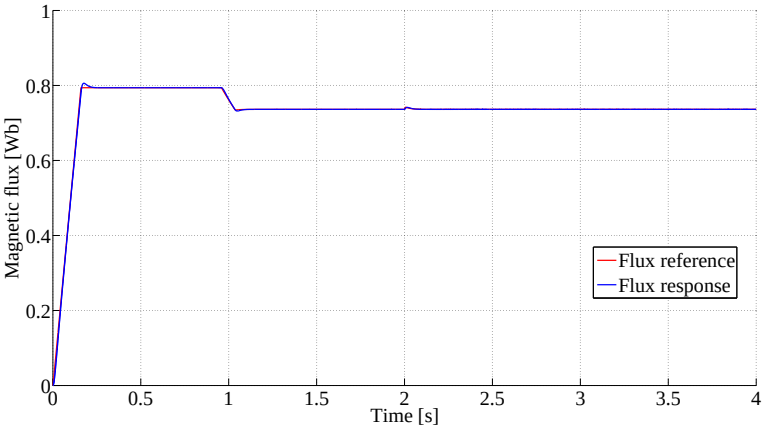

Figure 2.24: Simulated flux during field weakening test.

Some disturbances can be seen in the current waveform after applying the load which indicates that the controllers are not tuned to optimum. However, it does not affect the speed during the simulation and it is sufficient enough for testing the application after construction.

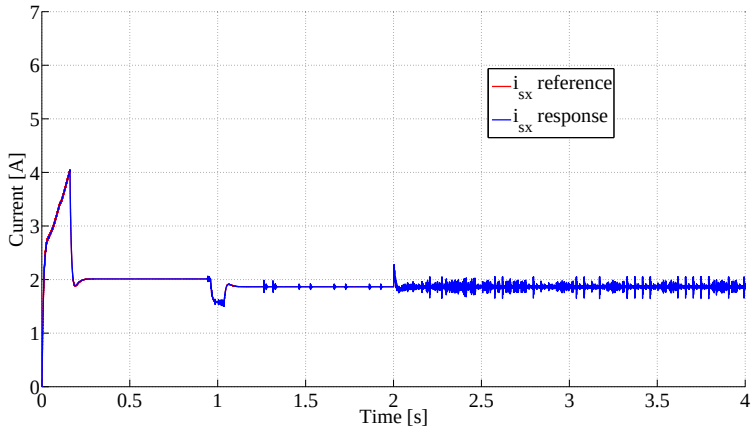

Figure 2.25: Simulated stator current real part in rotor flux reference frame during field weakening test.

Finally, Figure 2.26 shows the simulated three-phase current waveforms. Transition to field weakening operation can be seen from this figure as the amplitude of the currents decrease from slightly before 1 second marker onwards. At the 2 second marker, the load step is applied which increases the current.

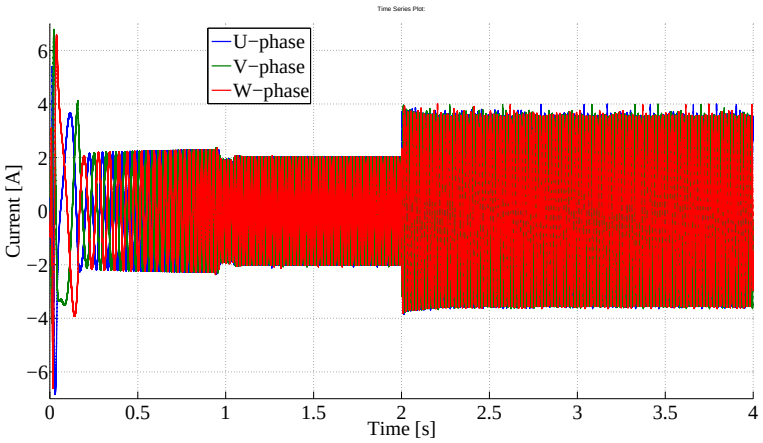

Figure 2.26: Simulated stator three-phase currents during field weakening test.

This concludes the simulation of the vector controlled induction motor drive model. These results were used as the basis for test bench construction presented in the next chapter. Furthermore, the control system designed in Simulink was used directly with the dSPACE system by replacing the induction motor drive model with real measurements from motor. However, more detailed description of this is introduced later on this thesis.

3. DESIGN AND CONSTRUCTION OF THE TEST SYSTEM

Primary purpose for this test system was to serve as laboratory equipment for students participating in the course DEE-34016 Modeling and Control of Electric Drives. During this course, they will build a mathematical model for an induction motor drive, design control and simulate operation of their model and control in Matlab Simulink environment. Until now, the design has included only verification by simulation. However, the objective of this system is to allow students to discover the real world responses of their design.

Some fundamental design objectives were made at the beginning of construction. The main objective was to build a test bench that would require little space in the laboratory and could be relocated with relatively small effort. The most limiting factor revealed to be the power of induction motors. Since, the size and weight of the motors grew very rapidly along the power.

The second fundamental criterion was to build a system that could also be used in other courses concerning motor, generator or grid converter applications. This lead to the demand of active grid side converters. Thus, allowing the power to flow both ways from the grid to the motor or vice versa. This chapter presents the physical structure and components of this system in detail. The first five sections present the different components of the test bench and the last section is devoted on describing the whole system.

3.1 Structure of the test system

The principles of desired system are described in Figure 3.1. The overall systems consists of two AC-AC frequency converters with active grid side bridges enabling two-way power flow. LCL-filters are included at grid side of both converters for current filtering.

The converters are both driving an induction motor. The other motor is working as a load and driven with torque control. Control of this motor is implemented by the system inside the purchased converter and only the torque reference is fed into it from dSPACE. In contrary, the other motor is operating as work motor, and control of this motor is implemented by using measurements of shaft speed/angle and motor currents which are fed to dSPACE. Hence, the control system inside

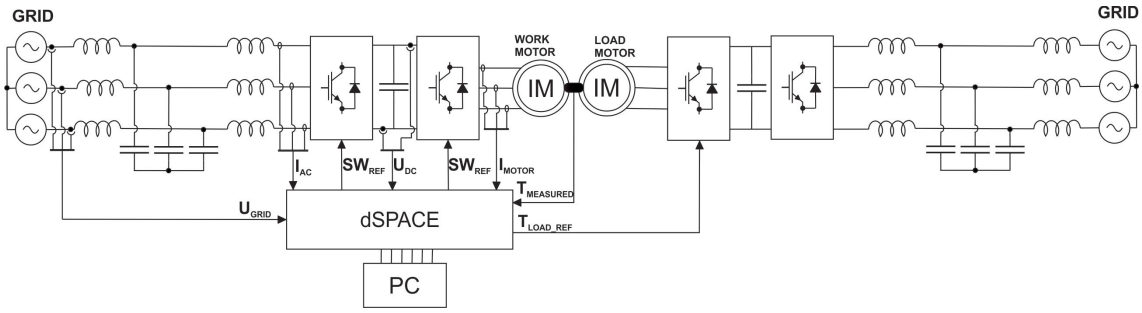

Figure 3.1: Graphical description of desired system.

the converter is bypassed, and instead the control system, created in Simulink, is used to drive the motor. The control of grid-side bridges of the converters are implemented similarly as the motor converter bridges. The other operates with the own software downloaded from manufacturer and the other utilizes control system created in Simulink.

As mentioned previously the work motor frequency converter is completely controlled with the control system created in Simulink. Hence, measurement of shaft speed, motor currents, grid currents, grid voltages and DC-bus voltage are required to implement the control. This produces a demand for measurement circuitry.

3.2 Motors and converters

The basic structure of the test bench consists of two frequency converters both with an active grid side three phase IGBT-bridge. Both of the converters drive an induction motor and the two motors are installed directly opposite each other and the shafts are coupled together. With this kind of set up, it is possible to drive the other motor as a load motor and the other motor as a working motor. When the electric motor operates as load it is possible to drive it with various load profiles such as constant or quadratically increasing torque load which enables the analysis of different motor drive phenomena existing in real industrial applications.

Two 2.2 kW aluminum frame three-phase induction motors were selected as the main components of this test bench. The selection was made based on the weight and size of the motors. Aluminium frame decreased the weight significantly compared to the iron frame, and the rather low 2.2 kW power resulted in a quite compact motor size. Furthermore, the higher nominal speed the motor had the lighter it was when motors with same power were compared. Figure 3.2 shows the purchased induction motor from different perspectives.

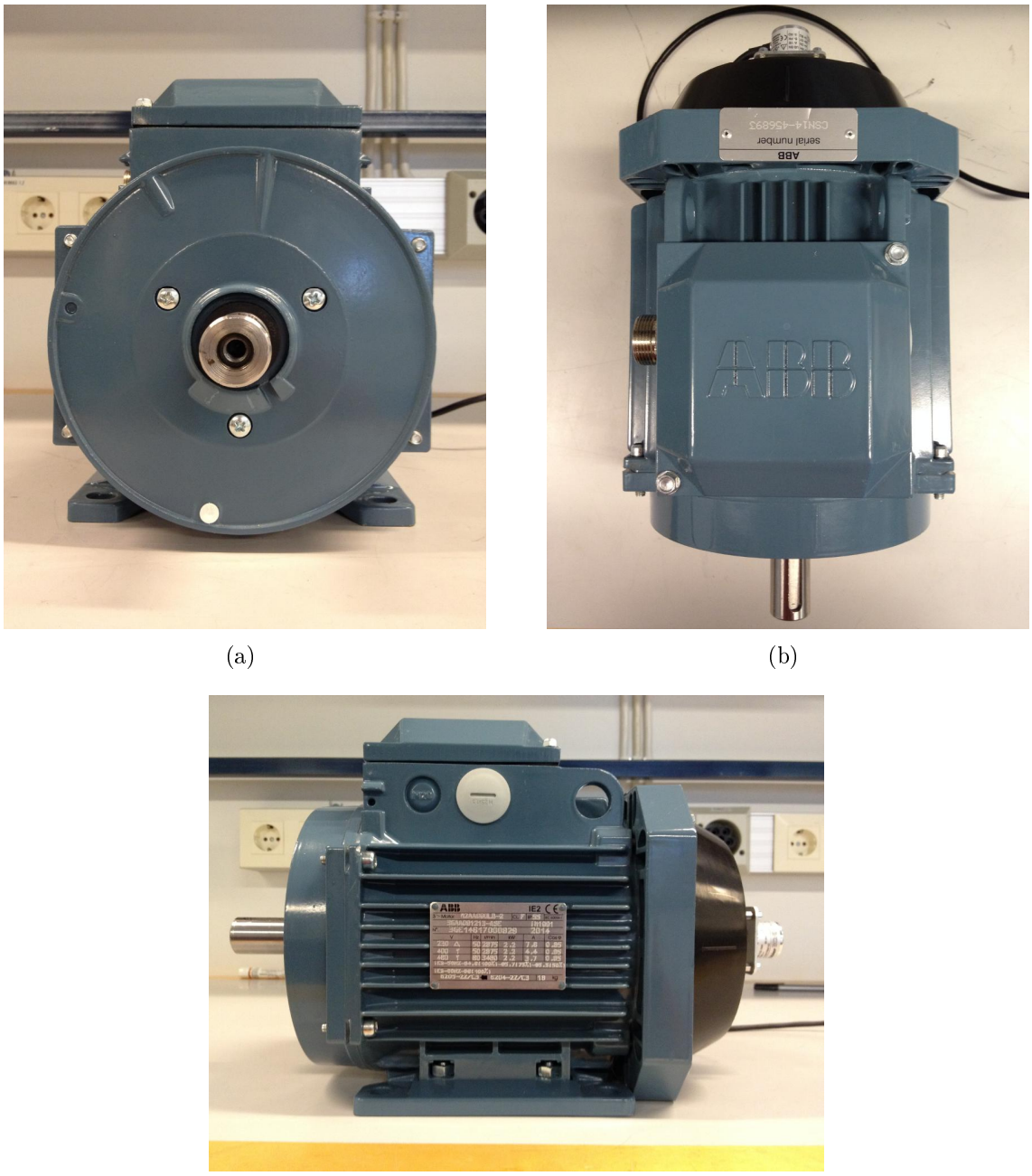

(a) (b)

(c)

Figure 3.2: ABB 2.2 kW induction motor (a) front (b) top (c) and side view.

Motors are manufactured by ABB and the product code is 3GAA 091 213-ASE. Table 3.1 presents the motor values from the nameplate. Since the nominal speed is 2875 r/min, the motor is two pole type. This can be verified using (2.1) and (2.2) presented in previous chapter. ABB supplied also the per-phase equivalent circuit values which are presented in Table 3.2. These values were used during the simulation and control system design presented in the precious chapter as well as in more detail in Appendix A.

Table 3.1: ABB 2.2 kW three-phase induction motor nameplate values

P_n	2.2 kW
n_n	2875 r/min
f_n	50 Hz
U_n	400 V
I_n	4.4 A (Wye)
$Cos\phi$	0.85

Table 3.2: ABB 2.2 kW three-phase induction motor per-phase equivalent circuit values

Stator resistance R_s	2.7 Ω
Stator leakage reactance $X_{s\sigma}$	3.1 Ω
Rotor resistance R_r	2.4 Ω
Rotor leakage reactance $X_{r\sigma}$	3.7 Ω
Iron loss resistance R_c	1449 Ω
Magnetizing reactance X_m	124 Ω

One Vacon NXP00135A2T1SSSA1A2000000 and three Vacon NXP00125A2H1SS SA1A2000000 frequency converters were selected as the drive elements in this test system. The decision was mainly based on the possibility of bypassing the control of converters relatively easily. In addition, Vacon was chosen as manufacturer due to previous similar projects successfully performed using dSPACE environment with Vacon drives. Hence, the literature regarding these projects could be found in the department. Furthermore, nominal power of these converters was selected as approximately double with respect to the motor power. This enables installation of slightly higher power motors in the future. Third reason for using Vacon converters was good contacts with the manufacturer which enabled support in problem solving.

Each of the Vacon frequency converters roughly consists of four fundamental parts; a three-phase diode rectifier in the grid side, a three-phase IGBT inverter in the motor side, capacitors in the DC bus and microprocessor based control system with measurement circuitry. In this application, DC-buses of a pair of converters were connected together. Thus, they formed a frequency converter with two active three-phase bridges. At this point the diode rectifiers were neglected since they do not enable power transfer into the AC grid. However, the diode bridges were used to charge the DC-bus capacitors.

Furthermore, the active converters demand filtering at grid side to filter down high frequency components in the grid current created by the switching of the grid side bridge. In this application, LCL-type filters were selected. They were a part of the hole order placed to Vacon. Hence, the sizes of the components were already designed by Vacon. The LCL-filters were manufactured by Platthaus GmbH and values of the components are presented in Table 3.3.

Table 3.3: LCL filter component values

Grid side inductors	3x 8.1 mH $\pm 10\%$
Capacitors (delta connected)	3x 2.2 μF $\pm 10\%$
Converter side inductors	3x 4.1 mH $\pm 10\%$

LCL-filter is a circuit that has a resonant frequency. At this frequency the impedance of the circuit approaches zero which may result in serious problems with control and harmonic currents. Thus, leading to the demand of damping, to avoid any undesired oscillation [11]. The filter in the load motor converter side does not require any passive damping since it is implemented actively in the software provided by Vacon. However, the work motor grid side converter LCL-filter damping is implemented passively with resistors in series with the capacitors. The sizing of these is implemented based on reference [11]. According to this, the resistance should be approximately 1/3 of the capacitor impedance at the LCL-filter resonance frequency [11].

The LCL-filter capacitors were connected in delta. Thus, first a wye-connected equivalent circuit needs to be calculated for the delta connected capacitors as presented in Figure 3.3.

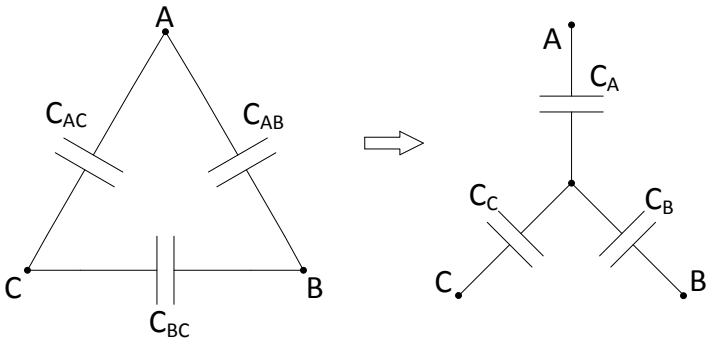

Figure 3.3: Delta-wye transformation for capacitors.

The transformation equations starting with impedances and ending with capacitances are presented in (3.1)-(3.3). The capacitor value in wye-connection corresponds to three times of the value in delta-connected circuit. However, this is only when all capacitor values are equal which is the case in this particular application and these equations could be used.

$$Z_A = \frac{Z_{AB} Z_{AC}}{Z_{AB} + Z_{AC} + Z_{BC}}, \tag{3.1}$$

since

$$C_{AC} = C_{AB} = C_{BC} = C_{\triangle}$$

also

$$Z_{AC} = Z_{AB} = Z_{BC} = Z_{\triangle}$$

and this yields

$$Z_A = Z_Y = \frac{Z_{\triangle}^2}{3Z_{\triangle}} = \frac{1}{3}Z_{\triangle} \tag{3.2}$$

and finally

$$Z_Y = \frac{1}{j\omega C_Y} = \frac{1}{3}Z_{\triangle} = \frac{1}{3j\omega C_{\triangle}} \Rightarrow C_Y = 3C_{\triangle} \tag{3.3}$$

Equivalent capacitor value for delta connection calculated with (3.3) is $3 \cdot 2.2\mu F = 6.6\mu F$. After this, the next task was to calculate the LCL-filter resonance frequency. This can be defined with (3.4) and calculated with values presented in Table 3.3.

$$\omega_{res} = 2\pi f_{res} = 2\pi\sqrt{\frac{L_c + L_g}{L_c L_g 3C_f}} = 2\pi\sqrt{\frac{4.1mH + 8.1mH}{4.1mH \cdot 8.1mH \cdot 6.6\mu F}} = 7461rad/s \tag{3.4}$$

In the equation, L_c is the converter side inductor inductance, L_g grid side inductor inductance, and C_f filter capacitor capacitance connected in wye. The answer 7461 rad/s equals to 1187 Hz. Next the capacitor impedance at the resonance frequency is calculated with (3.5). Where w_{res} is the resonant frequency calculated above and C_f is the wye-connected capacitor value.

$$Z_{cres} = \frac{1}{w_{res}C_f} = \frac{1}{7461rad/s \cdot 6.6\mu F} = 20.31\Omega, \tag{3.5}$$

Finally, the damping resistance connected in series with each capacitor is one third of Z_{cres}. However, the resistance must be transformed back to delta-connected, and the relation between these is $R_{\triangle} = 3R_Y$. Hence, this is inverse with respect to the capacitor value delta-wye transformation. Result is that each damping resistor has a physical value of 20 Ω. The final LCL-filter circuit, connected to the grid side of the load motor converter is presented in Figure 3.4.

The components presented in this section create the foundation for the system

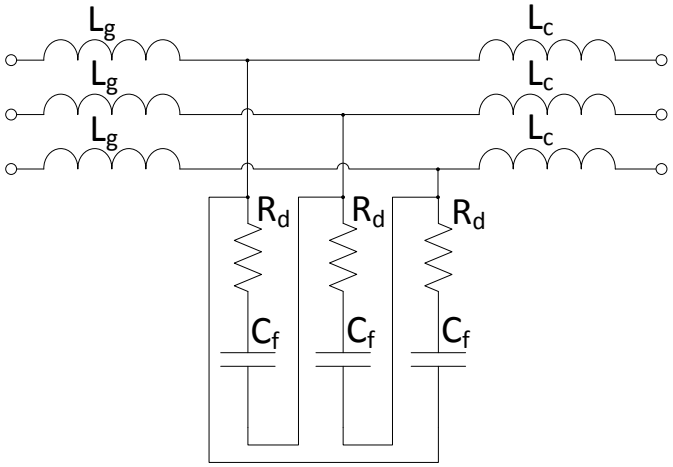

Figure 3.4: LCL-filter circuit with passive damping resistors.

constructed in this thesis. The following sections present the other additional components also vital for this design starting from the dSPACE system in the next section.

3.3 dSPACE DS1103 and CP1103

Control system design is one of the most time consuming and expensive areas in power electronics as well as in other engineering branches. The quick development in micro controller technology and the arrival of high-power digital signal processors (DSP) has enabled the use of high-level programming languages and software based control system development [14]. These factors have also influenced companies such as dSPACE to develop software and hardware to ease and speed up the control system design. Usually the design process begins by developing a simulation model of the controlled system or process. This is then used to design the control for the application. However, every mathematical model usually makes some assumptions regarding the modelled process and it differs from the actual system, and all of the responses can not be modelled using computers. This has led to the demand of quickly connecting the hardware to the designed control system for testing. Previously the testing had to be done by writing the code by hand for the microprocessor and then testing the functionality in real application [14]. However, this usually is very time consuming and probability for errors during this process is quite high. However, currently systems that enable automatic code building from simulation environment directly to DSP or other processor based real time simulation environment with interface to the real device have become more and more common among

control system developers in many engineering fields [14].

These type of systems are also beneficial for creating practical exercises for university level students in areas regarding control system development. At Tampere University of Technology, the Department of Electrical Engineering, Matlab is constantly used in simulations in various courses. Hence, a system providing Real-Time Interface (RTI) integrated with Matlab and Simulink environment was selected as the basis for this test bench. dSPACE is one of the manufacturers which provides these kind of systems. In this application, the DS1103 supplied with connector panel CP1103 was selected.

The DS1103 PPC Controller Board is a PowerPC based real-time control system supplied with a slave-DSP subsystem based on Texas Instruments TMS320F240 DSP microcontroller [15]. The CP1103 connector panel provides the interface to the hardware. It includes 20 analogue-to-digital converter (ADC) channels with BNC (Bayonet Neill-Concelman) connectors, 8 digital-to-analogue converter (DAC) channels with BNC connectors, a 37-pin Sub-D connector with 16 slave ADC channels, a 50-pin Sub-D connector with 35 digital I/O channels, a 37-pin Sub-D connector for slave digital I/O channels and signals such as PWM and clock, seven connectors for incremental encoder inputs and five RS connectors. More detailed description regarding the connections and signal mapping can be found in [15]. The CP1103 connector panel was connected to the DS1103 using three flat cables.

In addition to the DS1103 and the CP1103 a computer with Windows operating system, Matlab and Simulink installations were required. A desktop computer was selected as the host PC and it was connected to DS1103 using optical fibre supplied with an interface board that was connected to the computer motherboard. In addition to the hardware, the required dSPACE software had to be installed to the computer. This installation included software such as Real-Time Interface (RTI) for code generation, special RTI blocksets for Simulink and ControlDesk for real time monitoring and controlling purposes.

After all the required installations of hardware and software had been conducted, the next step is to construct the desired control system Simulink model. The process of building and testing the control system using dSPACE is quite straightforward if Simulink environment is previously familiar. The construction starts by creating the model of your control system using Simulink. During the dSPACE software installation packages that include interface blocks to the differenc outputs and inputs to CP1103 connector panel have been installed to Simulink block library. By using these blocks it is possible to use the connected measurement signalas a feedback for the control system. And similarly when control system calculates the reference value for the process it can be transformed to a digital or analogue signal and connect the selected channel to the real life process actuator. After the desired

model has been constructed, the next step is to build the model using C/C++ compiler found in Simulink. This then automatically compiles the model into C and uploads it into the DS1103 where the model starts to run. Next task is to open ControlDesk, create a new experiment, connect it to DS1103 platform and download the variable descriptions found in the same folder as the constructed Simulink model. Now ControlDesk provides the opportunity to change variables such as controller parameters in your model while it is running online without requiring to compile the model again. Furthermore, it is possible to plot and record the measured input values.

The control system model constructed for the test bench here is presented in more detail in the section where the complete system is presented and the model can also be seen in Appendix B. Now that the fundamental components are presented the next section introduces the measurement circuitry ans other additional components.

3.4 Measurement circuitry

First task was to create a list of necessary measurement components. Grid converter control requires measurements from grid currents, grid voltages and DC-bus voltage. Induction motor direct vector control requires motor current measurement, rotor speed and angle measurement. Furthermore, a torque sensor was decided to be installed since it is important to see the applied load torque and this also illustrates quite well the behaviour of the drive for students.

3.4.1 External power supply

The ADC inputs in dSPACE DS1103 support input voltages in the range of $\pm 10V$. With this knowledge an external DC power supply of $\pm 12V$ was designed for the measurement circuitry. This voltage range is sufficient enough to achieve voltages between $\pm 10V$ after voltage drops in the measurement circuits. However, it is also low enough not to cause voltages over the critical limits of dSPACE inputs. Figure 3.5 shows the schematic of the power supply. This supply is based on linear regulator technology and was selected because it provides extremely good quality DC voltage with wide range of output current. Hence, linear regulator based supply is good for measurement circuitry.

The circuit consists of a 1x230VAC to 2x15VAC step down transformer. High frequency components are filtered with capacitors before the full bridge diode rectifier. After rectification two higher value electrolytic capacitors act as filters and buffers before the linear regulators. In the regulator input and output, there are capacitors that are inserted based on the regulators' datasheets. Fuses are placed before the rectifier and sized according to maximum rated current of the regulators.

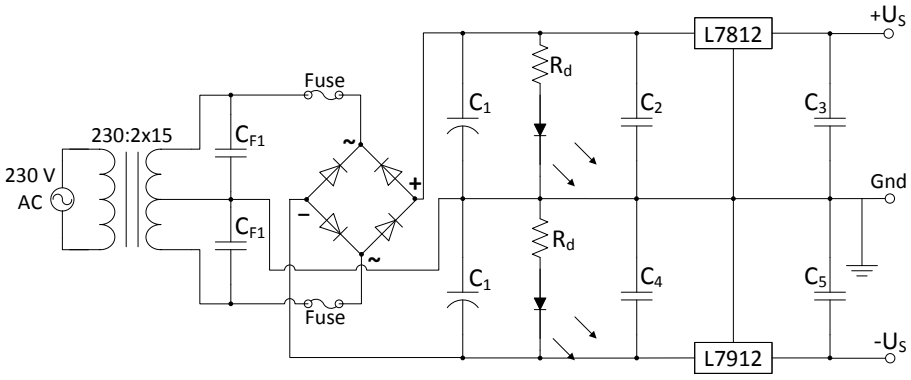

Figure 3.5: $\pm 12V$ DC linear regulator based power supply schematic.

Furthermore LEDs with resistors are placed parallel to the electrolytic capacitors to indicate on-state of the supply and to discharge the capacitors after switching off the power supply. Two equivalent DC supplies were manufactured since some measurement circuits required two voltage supplies for isolation purposes. Layout and picture of the soldered and finished power supply circuit boards installed into a plastic case can be seen in Appendix C.

3.4.2 Current measurement

Motor- and grid converters both required current measurement for control purposes. The measured currents are three phase and sinusoidal, and at least two out of the three currents had to be measured since third could be calculated from the two others. Three different options were considered when the measurement circuit was selected. First option was to purchase a ready built current probe from the market. However, this option was discarder on the early stage because either the price of one probe exceeded hundreds of Euros or it was not suitable due to other reasons such as wrong input current measurement range or unsuitable power supply range. Furthermore, it is not reasonable to use expensive current probes with over 1 MHz bandwidth for control purposes in a permanent installation that requires only under 10 kHz bandwidth. The probes with their power supplies were also rather large for this particular installation.

The second option was to find a suitable current measurement circuit board for this purpose from the market. However, this appeared to be a difficult task and I could not find any relevant circuit board. Therefore, the third option of building the measurement circuit yourself was only relevant solution.

This began by deciding a suitable current transducer. Fortunately the department

had spare LEM LA 55-P transducers in the storage. These transducers deploy hall effect and were rated to measure currents in range of $\pm 100A$ which it is sufficient enough for this test bench. Furthermore, supply voltage for the transducer could be in the range of $\pm 12V ... \pm 15V$. This enabled use of the built DC supply. Since there were more than six of these parts I decided to built two measurement circuits with three transducers, one for each phase current. Schematic of one measurement channel is presented in Figure 3.6.

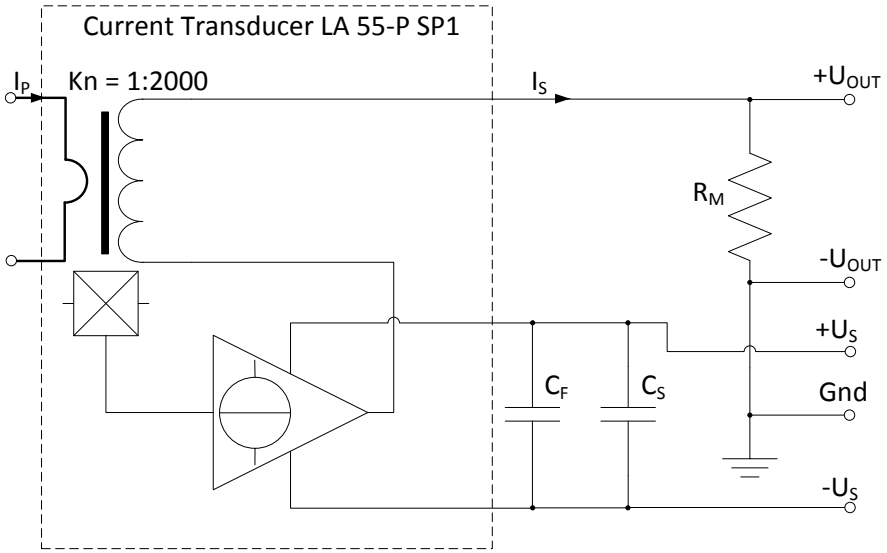

Figure 3.6: Schematic of one signal channel of current measurement circuit.

The LA 55-P transducer has a current output and the ratio between this and measured current is 1:2000. This means that 1A in primary corresponds to 0.5mA in secondary. This current output needs to be transformed to voltage and amplified for dSPACE ADC input. The transformation was performed with resistor R_M and the output voltage over this was transmitted into an amplifier and buffer circuit represented later in this section. Selection for resistor R_M value was based on the current ranges of the converters. From Vacon NXP manual, we got the maximum rms current of $I_S = 18A$, which corresponds to amplitude of $\sqrt{2} \cdot 18A = 25.46A$. Range of $\pm 24A$ was selected for the grid converter measurement circuit. As it will be explained later the measurements will be amplified with gain of 6.06 in the buffer circuit. To achieve measurement range of $\pm 10V$ in ADC input, the input of buffer circuit had to be in the range of around $\pm 1.65V$. This was achieved using resistor value $R_M = 133.2\Omega$. The motor converter current was chosen as $\pm 20A$. Although, an induction motor may draw 7-9 times the nominal current at start during the direct grid connection, the starting current can be controlled in frequency

converter drives. Hence, the selected range of above three times motor nominal current amplitude $\sqrt{2} \cdot I_n = \sqrt{2} \cdot 4.4A = 6.22A$ was sufficient enough. With this range the selected resistor value was $R_M = 162.1\Omega$. Furthermore, filter capacitors were inserted between each current transducer power supply pins. Pictures of the final PCB board together with the layout figures are presented in Appendix D. Two of these boards were made and they were installed into a metal box to reduce electromagnetic interference.

3.4.3 Buffer and filter circuit

Current measurement board designed above required an amplifier circuit in order to achieve the desired voltage range. At this moment the output range of the transducers was -1.65 V...+1.65 V. This had to be amplified with 6.06 to reach the range from -10 V...+10 V. This problem was solved using Texas Instruments INA126 instrumentation amplifier. In addition to amplifying the signal an instrumentation amplifier also reduces common-mode noise quite effectively making it a beneficial solution for this application. Furthermore, INA126 gain could be modified by changing only one resistor value. Figure 3.7 illustrates one channel of the combined amplifier and filter circuit.

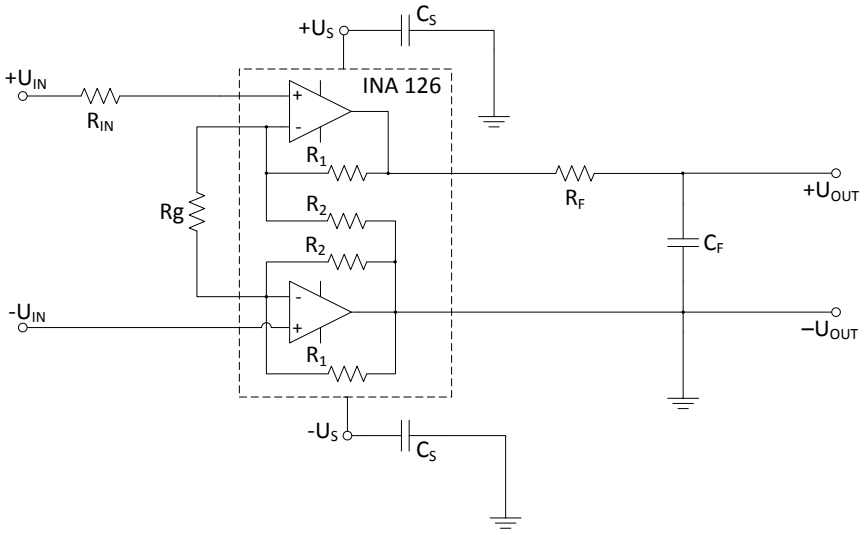

Figure 3.7: Schematic of one channel of combined buffer and filter circuit for current measurement.

The output from the current measurement board is fed between $+U_{in}$ and $-U_{in}$ where the resistor R_{in} is limiting the current in fault situations. R_g is the resistor that can be used to modify the gain of the INA126. The resistor value can be calculated using (3.6) obtained from the component datasheet.

$$G = 5 + \frac{80k\Omega}{R_g} \Rightarrow R_g = \frac{80k\Omega}{G - 5} \tag{3.6}$$

Since the selected gain for our circuit was 6.06 the value for the resistor had to be 75.47 $k\Omega$. A 75 $k\Omega$ resistor was then used. In addition to the amplification, also a passive low-pass RC filter circuit was added for each channel to damp the high frequency components from the measurement to prevent problems in the control. The cut-off frequency of the RC filter was chosen as 5 kHz which is half of the switching frequency. This was used since it is a standard procedure in many control design task regarding power electronics. 750 Ω was chosen for R_F. The capacitance value of can be calculated with (3.7) that defines the RC circuit cut-off frequency.

$$f_c = \frac{1}{2\pi R_F C_F} \Rightarrow C_F = \frac{1}{2\pi R_F f_c} \tag{3.7}$$

5 kHz and 750 Ω result in capacitor value of approximately 42.4 nF. Value 47 nF was found from the shelf and selected. This increases the cut-off frequency but only slightly. The completed layout figures and picture of the final circuit board are presented in Appendix E

3.4.4 DC-bus voltage measurement

In order to control the DC-bus voltage with the grid converter, measurement from the bus is required. Voltage level over the DC-bus in a three phase converter is above 540 V. With this high voltage level, insulation and voltage ratings of measurement components have to be considered more thoroughly. Furthermore, it is important to isolate measurement circuit from the measured DC bus for safety and operative reasons. Measurement circuit built during this construction is based on Texas Instruments ISO124 isolation amplifier that incorporates a capacitive isolation barrier. The schematic of this measurement circuit can be seen in Figure 3.8.

Bus voltage measurement was implemented using simple voltage divider based on resistors. This was used due to its robustness, linearity and wide measurement range. Output range was selected to be 0-10 V and since the gain of the isolation amplifier is one the input of the ISO124 had to be 0-10 V. Resistors were selected such that 1000 V in the DC-bus corresponded 10 V over resistor R_M. Six $100k\Omega$ resistors with voltage rating of 500 V and one $6.04k\Omega$ resistor with voltage rating of 250 V were selected for this configuration. Equation (3.8) shows relation between measured and actual voltage with these resistors.

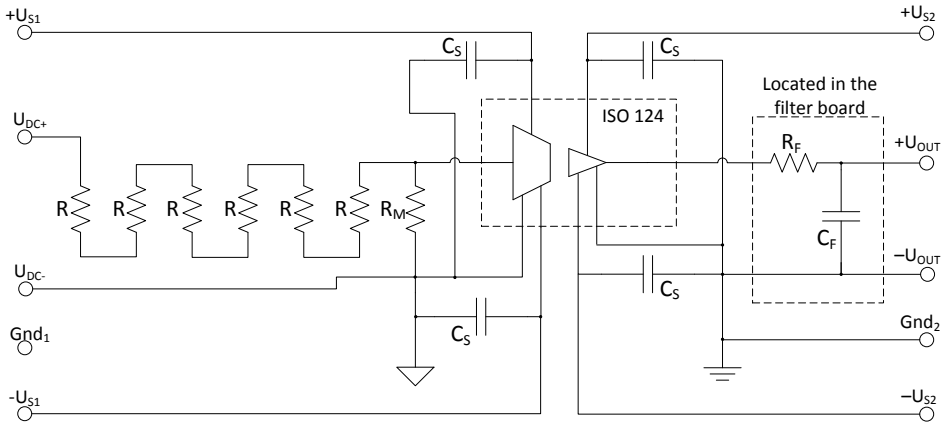

Figure 3.8: Schematic of converter DC-bus measurement circuit.

$$\begin{aligned} U_M &= \frac{R_M}{6R + R_M} U_{DC} \\ &= \frac{6.04k\Omega}{(99.1 + 98.7 + 98.8 + 98.7 + 99.1 + 98.8 + 6.04)k\Omega} U_{DC} \\ &= 0.0101 U_{DC} \end{aligned} \tag{3.8}$$

Values for the six R resistors were measured with a multimeter, and as can be seen from the result, the desired relation 1/100 was achieved. Voltage is divided over multiple resistors to decrease voltage stress in one resistor, thus reducing the risk for breakdown. A first order low-pass RC-filter is also inserted before ADC input to reduce noise induced from the switching of the converters. This RC-filter is placed on the buffer and filter board used with the current measurements and the design is same as described in the buffer-filter circuit section. From the schematic figure, it can be noted that the isolation amplifier required two different power supplies to succeed in isolation. Hence, the same supply that was used with the current measurement circuit was also used in the secondary side in this application. The other built DC supply was used in the primary side. The final layout figures together with the picture of the finished circuit board are shown in Appendix F.

3.4.5 Grid voltage measurement

Grid side converter requires grid voltage measurement because it has to be synchronized with them. Thus, a circuit for measuring grid voltages had to be constructed. The order from Vacon included two expander I/O boards for grid voltage

measurement both supplied with a measurement transformer. Since only the other converter was controlled with its own software the other measurement transformer could be used to construct the grid voltage measurement for dSPACE. A measurement transformer is beneficial for this purpose since it provides also galvanic isolation in addition to the measurement signal. The transformer had two primary and two secondary windings. Hence, two line voltages were decided to be measured and the third could be calculated with software. The transformers had a ratio of 60:1 which meant that 325 V amplitude in the primary corresponded to 5.42 V in the secondary. This was also verified by multimeter measurement. In addition to the transformer, a similar buffer circuit as in current measurements was decided to be constructed. A buffer circuit was added mainly to avoid over voltages in the dSPACE ADC input. Hence, the cheaper self built circuit would break before expensive dSPACE equipment in a fault situation.

Schematic of the grid voltage measurement circuit with the measurement transformer is presented in Figure 3.9. First the transformer steps down the sinusoidal grid voltage from amplitude 325 V to 5.42 V. After this the voltage signal is divided over resistors. This is done because the minimum gain using INA126 instrumentation amplifiers is 5 when no resistor is connected at R_g. Voltage input amplitude to dSPACE ADC was selected to be 7.5 V when grid voltage is 325. This meant that the voltage at the INA126 input had to be scaled down to $7.5/5 = 1.5$ V. Thus a voltage divider had to be implemented using resistors. These were calculated and selected values were $R_3 = 34.74\ k\Omega$ and $R_4 = 12.99\ k\Omega$. These resulted in instrumentation amplifier input voltage of $5.42 \cdot (12.99\ k\Omega / (34.74\ k\Omega + 12.99\ k\Omega)) = 1.48$ V when amplitude of grid voltage is 325 V. This in turn yielded in the desired voltage amplitude of 7.5 V at the ADC. This should have been done using buffer with lower gain and voltage division would have been avoided. However, there were no other instrumentation amplifiers available at the department and INA126 had been previously ordered for the current measurement buffer circuit purposes. Thus, it it was easy to use the spare amplifier to this circuit. RC filter seen in the schematic diagram was not connected to constructed the circuit but places were left for option if there was some disturbance visible in the measurements. One more factor to be noted at this stage is that the measurement transformer inverts the voltage at the secondary side. Hence, this needs to be inverted back in the dSPACE model. The layout figures, pictures of the finished circuit boards and picture of the measurement transformer are presented in Appendix G.

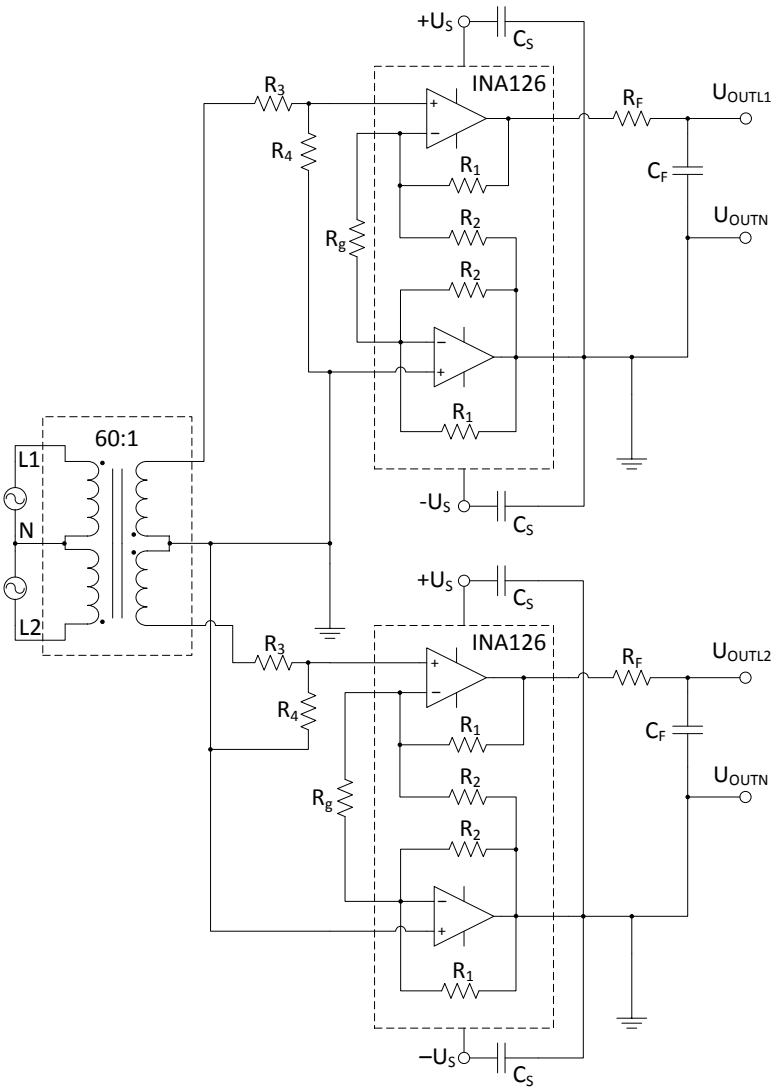

Figure 3.9: Schematic of grid voltage measurement circuit.

3.4.6 Torque transducer and incremental encoder

Now that all of the other measurement circuits were constructed, the next task was to select the components responsible for torque measurement and rotor angle/speed measurement. Both of these circuits require mechanical construction and special parts when they are built. Hence, these are difficult to construct without proper knowledge and they were purchased. The torque transducer selection was mainly based on the nominal torque of approximately 7.3 Nm of the 2.2 kW induction motor. Even though induction motor maximum torque is multiple times larger than the nominal value it is usually operated nearer to the nominal than to the maximum. Furthermore, with variable frequency drive it is possible to accelerate

the motor with constant nominal torque and no torque peak is shown as during the direct grid connection. Nevertheless, a 50 Nm Kyowa TPS-A torque transducer was selected. This transducer can be safely loaded with 120 % times the rated torque. Hence, it is more than sufficient for this application and can withstand even slightly larger motor. Picture of the transducer is presented in Appendix H. This torque component provides an analogue output signal ranging from -5V to +5V with input range from -50 Nm to +50 Nm. This gives the relation of 0.1V/Nm. In order to exploit the whole ADC range from -10 V to +10 V in DS1103 the torque transducer output voltage was scaled with resistors and then amplified using the same INA126 instrumentation amplifier as in the previous circuits. After this buffer the relation was 0.2V/Nm. This results in 10 V ADC input voltage if the measured torque is 50 Nm. Hence, now the whole ADC input range is employed.

In addition to the torque output, this transducer provides also pulsed speed output. At first this was planned to be used for the induction motor vector control speed feedback. However, the pulse output revealed to have only 4 pulses/rev resolution which is not sufficient enough. Furthermore, the inverter driving the load motor was used with torque control and in order to produce better load response it required feedback from an incremental encoder. These two reasons forced to purchase an encoder with higher resolution. However, since DS1103 can directly transform incremental encoder pulses to speed and angle no additional circuitry for transforming the pulses into speed and angle were required. The plan was to use the same encoder output for both applications: Vacon converter and dSPACE input. However the next issues emerged from the fact that the Vacon encoder expander board required 24 V encoder pulses whereas the dSPACE incremental encoder input worked on 5 V pulses. The solution for this problem was to purchase encoder that would work with 24 V supply provided from the Vacon encoder board and then build an interface circuit that would transform the 24 V pulses into 5 V pulses using optical isolation and dSPACE +5 V supply.

The result was that a Kubler incremental encoder with the resolution of 1000 pulses/rev and supply voltage range from 15 V to 24 V was purchased. This was connected directly to the Vacon encored board and to the 24 V supply it provided. Next an interface circuit that was planned to be connected in parallel with the Vacon encoder board was designed. The design was based on Avago ACPL-W480 optocoupler that has a GaAsP led at the input and a push-pull configuration at the output. This type of output was required since no pull-up resistors could have been used with the dSPACE encoder input. The voltage for the pulses in the output was provided by the dSPACE since it had a pin for +5 V supply at the encoder connector. A picture of the incremental encoder connected to the motor shaft, layout design of the encoder dSPACE interface and picture of the finished circuit board are presented

in Appendix I. It is not advisable to use the same encoder for both motor controller feedbacks because actually the shaft couplings are not completely rigid and this might cause problems in the control. Another encoder connected to the shaft of the work motor would be the first improvement for this test bench even though the control worked with only one encoder.

3.4.7 Optical transmitter circuit

The original plan was to bypass the Vacon control from the grid and the motor converter connected to the work motor. The solution for this problem was to order VaconBus adapter cards that enable the separation of the control part from the part including the power semiconductors [17]. These cards transfer the information between the two parts using optical fibres. There are seven optical fibres in total and the signals contents are gathered into Table 3.4.

Table 3.4: VaconBus optical fibre signal content [17]

Fibre no.	Signal content
1	Enable signal for the switches
2	Phase U upper switch PWM signal
3	Phase V upper switch PWM signal
4	Phase W upper switch PWM signal
5	Signal for AD conversion start at the power part
5	Serial data receiving
7	Serial data transmitting

In conclusion, the optical fibres 1-4 are responsible of the switching of the IGBTs and the fibres 5-7 transfer measurement data between the control part and the power semiconductor part. Hence, the signals 1-4 had to be bypassed and the information regarding these transmitted from dPSACE. dSPACE DS1103 slave DSP has built-in PWM signal generators and it can simultaneously supply seven separate PWM signals. This is sufficient enough for this applications because both of the converters required only the PWM signal for the upper switches of the IGBT bridge. Hence, total PWM signal count in this application is six. The ASIC-circuit in the VaconBus adapter card creates the inverted signals for the three lower switches and it also creates the dead time for each switch. Hence, the ideal PWM signals can be transmitted from dSPACE. In addition to the PWM signals an enable signal which is needed to start the modulation of the IGBTs is also required from dSPACE. The digital signals supplied by DS1103 are TTL (Transistor-transistor logic) type which means that logical low is between 0 V-0.8 V and logical high between 2.2 V-5 V. These voltage signals need to be transformed into optical and the next task was to construct this optical transmitter circuit.

The first task at this stage was to select a suitable optical transmitter component. The selection for this was based on observing the VaconBus adapter card and a similar transmitter was chosen as the basis for this circuit. The selected transmitter was Avago HFBR-1521Z. Furthermore, a Texas Instruments SN75451 peripheral driver was selected to be the switching component for the transmitter. The schematic diagram of the designed optical transmitter is presented in Figure 3.10.

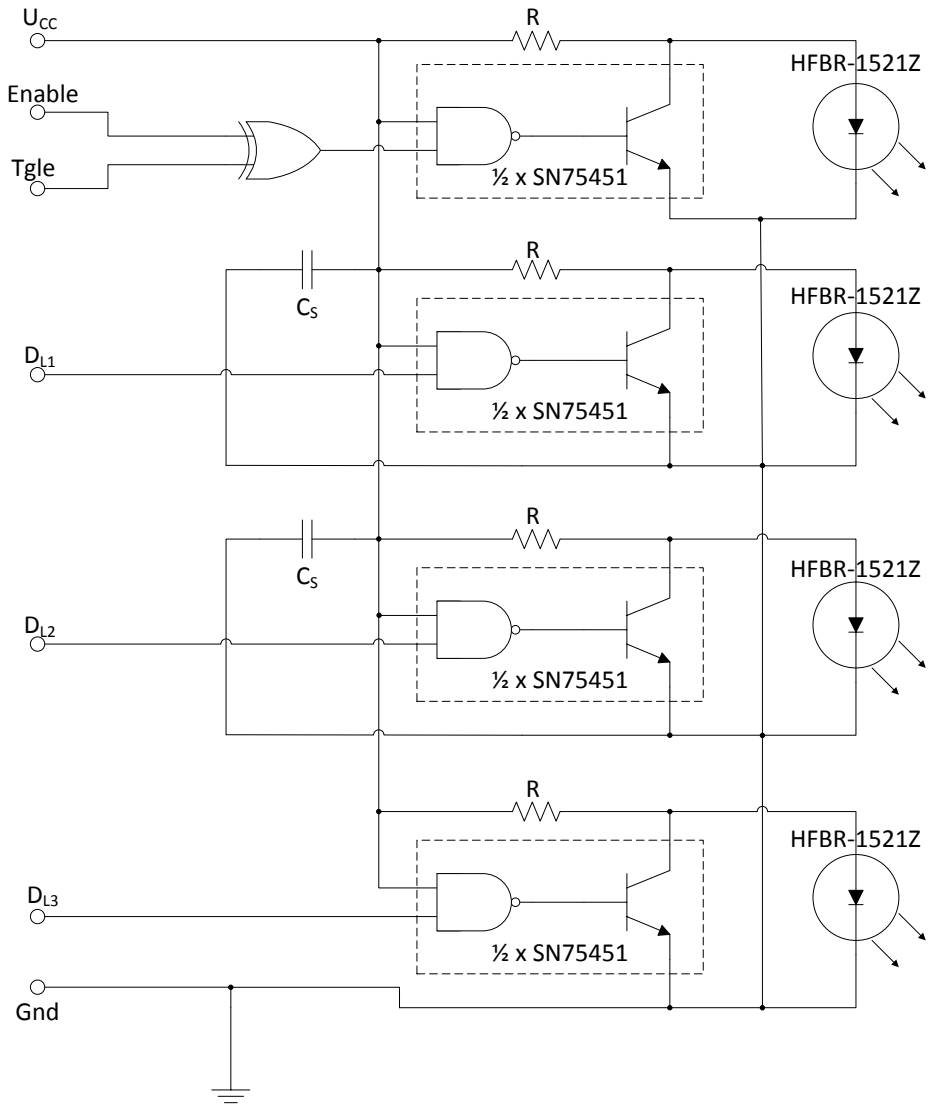

Figure 3.10: Schematic of optical transmitter circuit.

The inputs D_{L1}-D_{L3} are for the PWM signals. When a logical high is inserted to these inputs the optical transmitter in that channel gives out logical high and the led is illuminated. The enable signal is additionally supplied with a XOR-gate. The gate has two input signals: enable and toggle. This is implemented because

during the model compilation the I/O pins of the DS1103 are switching states and if nothing would be done the enable signal would also switch states and cause the power semiconductors to switch uncontrollably. Now that the XOR-gate is inserted the fibre enable is at logical high only when the dSPACE enable and toggle have different states. The layout design and picture of the finished circuit board are presented in Appendix J.

3.4.8 Load motor control circuit

The final required circuit to build was for the control signals from dSPACE to the converter which control the load motor. The purpose for this circuit is to rise the TTL level signal to be suitable for the Vacon converter basic I/O board which requires 24 V supply based digital I/O signals. The signals conducted through this circuit are on and off commands for the load motor converter and grid side converter. Schematic of the designed load motor control board is presented in Figure 3.11. In this circuit, the control signal is transmitted into a XOR-gate again to avoid unnecessary switching during the model compilation. The XOR-gate output is then transmitted to a operational amplifier that operates as a comparator. If the positive input of the op amp is greater than the reference in the negative input the 24 V supplied by Vacon converter is fed to the U_{out+} connected to the start signal input in the converter.

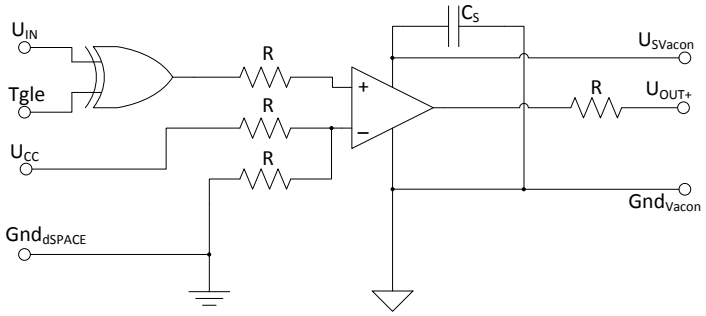

Figure 3.11: Schematic of load motor control signal circuit.

In addition to the start and stop signals, also the load motor torque reference signal is transmitted to the converter. However this is done directly from dCPACE DAC ouput since the reference signal input for Vacon basic I/O board accepts voltage range 0-10 V which is possible to obtain with dSPACE. Furthermore, another DAC signal is fed to the motor converter to supply a speed limit for the motor, because during torque control it would accelerate infinitely until something would break if there was no speed limit.

3.5 Complete system

After completing the construction of the components they were installed to the bench and a lot of testing was conducted between every installed component. Furthermore, each of the components had to be tested also separately before installation. Figure 3.12 presents the completed system after installation of all the necessary components. In this figure the test bench construction is located on the left. The dSPACE DS1103 and CP1103 are located on the table in the centre of the figure. And on the right is the host PC with the user interface containing Simulink and ControlDesk.

Figure 3.12: Figure of the complete induction motor test bench.

The test bench on the left contains all of the drive elements. The most top left is the grid converter for the work motor drive and next to it is the motor side converter both with the bypassed control. The grey cases below these are the DC bus measurement circuit and measurements for both grid and motor currents. The larger grey case in the top middle with a transparent cover contains switches and contactors for starting the converters as well as over current protection. Below this slightly on the left are the external DC supply circuits in the case with a transparent cover and the transformers for them in the grey metal case. Directly on the right from these is the case for measurement transformers for Vacon and for dSPACE. On the top right is the grid converter for the load motor drive and next to it on the left is the load motor converter. Below these is first the control board for these two and

also the optical transmitters for the bypassed converters. At the bottom are the two ABB 2.2 kW induction motors. Work motor is located on the left and load motor on the right. Between these is the torque transducer. The large metal case with a transparent top behind the motors contains the grid side LCL-filters for both grid converters. On the back, not seen in this figure, are the amplifier/filter circuits from where the signals are transmitted to dSPACE using coaxial cables.

When all the installations had been done the next step was to implement the control system in Simulink. This was implemented using the same model that had been used previously in the simulations. Induction motor model was removed from the system and replaced with RTI blocks for current, speed and angle measurements. At this stage the control for grid converter was not implemented due to lack of time. However, all the necessary measurements are implemented so only the control system Simulink model needs to be constructed. More thorough description of the motor control model is presented in Appendix B.

When the control system had been finalized, the last task was to calibrate the measurement signals. The current measurements were calibrated using a DC voltage source and a multimeter. One ampere of DC current was conducted through each measurement transducer simultaneously measuring the current with the multimeter and scaling the parameters in dSPACE model so that the correct scaling factor was achieved. After this also higher currents were tested for verification. Similar calibrating process was also implemented with the DC-bus and grid voltage measurement circuits. The motor speed validity was verified using Vacon converter that had an output for monitoring the motor speed calculated from the encoder input. After all the necessary calibrations and verifications were conducted the next step was to verify the operation of the drive by measurements. This is performed in the next chapter.

4. MEASUREMENT RESULTS AND EVALUATION

After completing the test bench construction, the final task was to verify the control system operation. Similar test drives were conducted as in the simulations presented in the theory part of this thesis. The measurements were obtained directly from the measurement circuits presented in the previous chapter. The data acquisition was executed using ControlDesk software that transferred measurements from dSPACE DS1103 via optical fibre as described in the previous chapter. The measurement data was then transferred to Comma Separated Values File that could be directly used in Matlab to extract matrices containing the data points. The matrices were then used to draw figures shown in this section.

As described in the construction part, the current measurements were filtered with a passive RC low-pass circuit with cut-off frequency at approximately 5 kHz. Furthermore, the DS1103 measurements were synchronized with the PWM-modulator so that every measurement point was stored during time the period when none of the six switches was changing their state. Hence, the ripple in the motor currents caused by the switching was minimized in the measurements. One measurement was conducted at every switching period of the inverter which resulted in a data acquisition frequency of 10000 kHz. These factors above result in a situation where current measurements shown here present the waveforms that are used for control purposes. hence, the actual current waveforms differ slightly by containing more of the switching ripple caused by the semiconductor switching. This is important to notice before evaluation of the results presented in this section.

The speed and torque measurements presented here were also obtained using ControlDesk. Hence, the torque transducer and incremental encoder presented in the construction section provide the measurement signals for these. The data acquisition frequency with these measurements was also 10000 kHz.

Three different test cases were conducted in this section. Each of them were then used to evaluate motor drive responses in different operation regions. The cases were constructed in a similar manner as the simulations previously to enable comparison between the model and real life system. First section presents measurement results from acceleration/deceleration test under no-load operation, in the next section a step change in load torque is applied during constant speed, then in the third section

operation in motor field weakening region is tested and finally the obtained results are evaluated in the fourth section.

4.1 Acceleration and deceleration

In this section, the first a speed ramp reference from 0 to 2000 rmp was given with a slope of 1000 rpm/s. After the motor had achieved a constant speed of 2000 rpm it was kept for few seconds. And finally the speed reference was decreased back to zero with slope of -1000 rpm/s. The motor was load was kept at zero during the entire test run. Figure 4.1 shows the speed reference value and the actual measured speed response of the motor during the whole test period. When observing this the system seems to response quite well for the given speed reference.

However, if more detailed view shown in Figures 4.2(a) and 4.2(a) is observed, some small oscillation seems to occur around the steady-state reference value. This oscillation has an amplitude of 1.5 rpm which is still within acceptable range, since it is only fractions of the reference speed value.

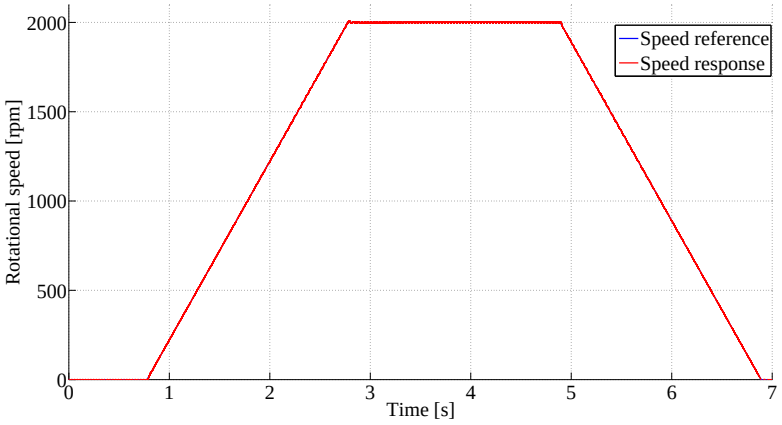

Figure 4.1: Speed reference and measured speed during entire acceleration and deceleration test.

There might be multiple reasons for this oscillation phenomena. One reason could be disturbances induced to the speed measurement itself. However, since the speed measurement is implemented using incremental encoder with pulsed signals probably the disturbance affected by this would seem greater. Other reason could be that the mechanical structures have some resonance frequency which affects the speed around this rotational speed. This might be one good explanation, since the oscillation frequency is rather low approximately 30 Hz calculated from these figures. The third possible reason could be not optimally tuned speed controller.

However, if these measurement results are compared with the results obtained by simulation they seem to correspond fairly well. The overshoot in both during the

acceleration is approximately the same: 5 rpm in simulation and 7 rpm in measurements. With deceleration the simulation differs slightly from the measurements and the response is little faster in simulation. In conclusion, the major difference is the small oscillation that occurs at the steady-state speed.

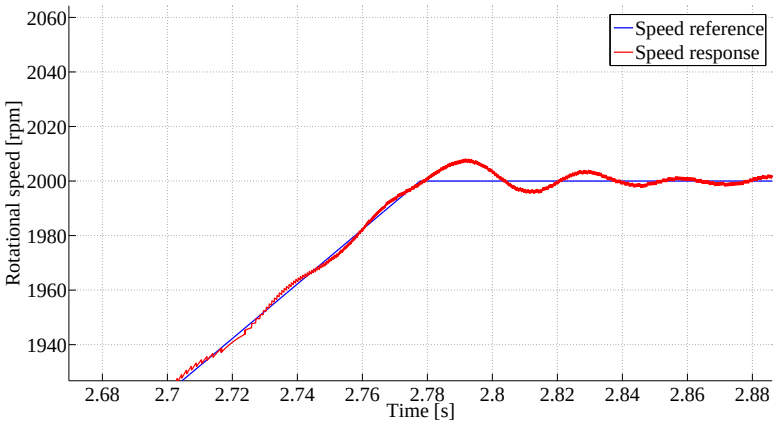

(a)

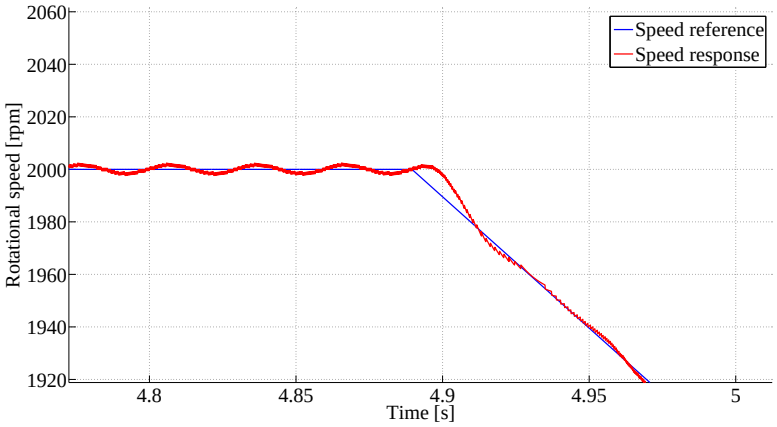

(b)

Figure 4.2: Speed reference and measured speed during (a) acceleration ramp and (b) deceleration ramp.

Figure 4.3 shows the measured shaft torque. Closer inspection reveals some disturbances at the measurement. There is also a DC-offset of approximately 0.1 Nm, since at the beginning from 0s to 0.8 s no torque was applied to the shaft. However, if these factors are taken into account when evaluating the results it can be seen that during the acceleration ramp measured torque is approximately 0.3 Nm, during the constant speed zero and during the deceleration ramp it is -0.3 Nm. These results are also quite well comparable with the simulation results.

Figure 4.4 shows the measured three-phase motor currents. Figure 4.4(a) is the measurement from the entire time period whereas Figure 4.4(b) illustrates the accel-

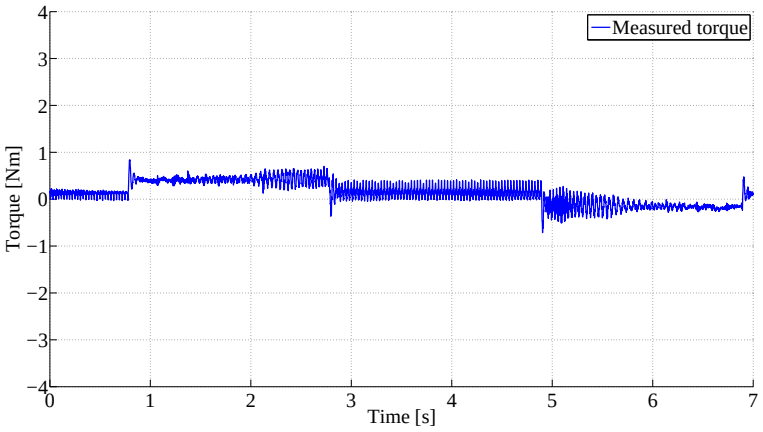

Figure 4.3: Measured torque at the shaft during acceleration and deceleration test.

eration part currents. From the beginning to approximately 0.8 s, the phase current have constant values. The reason for this is that when the modulation of inverter is started, the speed reference is still zero, but the flux reference starts to increase with a ramp right after inverter is started. Hence, the DC current is for magnetizing the motor. In the future, this should be changed and it is possible to implement in the Simulink model. Even though, the current levels in the windings are quite small and probably no harm will be caused, since the speed is usually increased right after start.

If the measurements are investigated more thoroughly, it can be stated that the current amplitude stays at 2 A during the whole measurement period with speeds from 0 to 2000 rpm. The only quantity that is changing during this measurement is frequency of the current. This can be noticed better in the extended view shown in Figure 4.4(b) where it is obvious that frequency is increasing during the acceleration but the amplitude remains unchanged. Again when these results are compared with the simulations, they are quite consistent. The only difference exists at the start up situation where there is no higher transients noticeable in the measured currents. This is due to the fact that during the measurement, the motor is already magnetized before starting of the rotation whereas in simulation everything starts in the beginning.

These current measurements present the waveforms that are used by the control system. Hence, they do not show the actual currents flowing in the motor. However, this is still extremely educational for the students. Furthermore, it is rather easy to attach a current probe to one phase conductor leading to the motor and demonstrate the difference of real current and the one used in the control purposes by showing both of them in oscilloscope window. This is possible, since the dSPACE current measurement can be taken out from one DAC channel and attach it to oscilloscope.

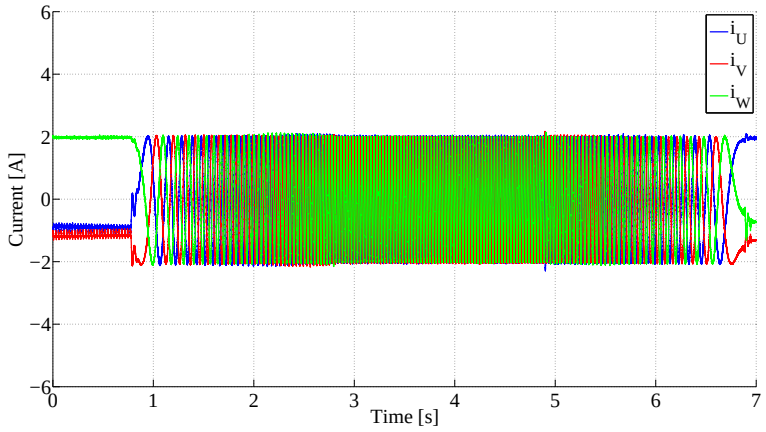

(a)

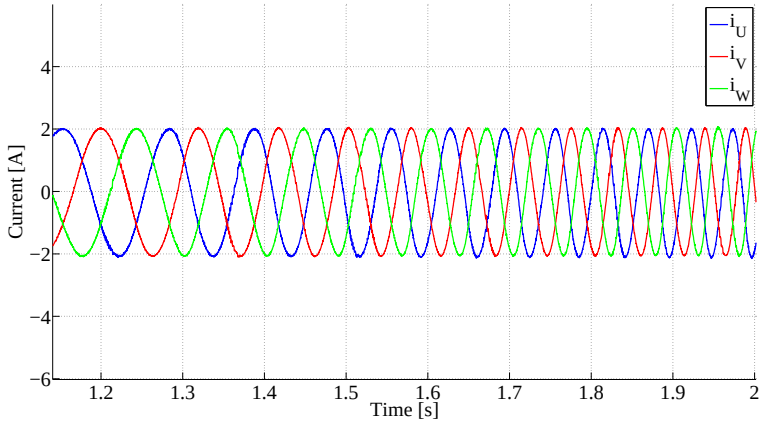

(b)

Figure 4.4: Measured three-phase currents during (a) the entire test period, (b) acceleration ramp.

Finally, Figure 4.5 ends this section by illustrating the stator current space vector components i_{sx} and i_{sy} calculated in rotor flux reference frame using the measured three-phase currents together with the measured rotor angle. It can be seen that the transformation is successful, since the components are both DC values. The blue curve is staying constant during the whole time as is supposed to, since it is the component that is responsible of magnetization. Whereas, the red curve is the stator current component that is responsible for motor torque. When the red curve is compared with the torque measurement it is obvious that they have a relation. If we once more compare these measurements with simulations it can be stated that they correspond rather well. Of course the measurements have more disturbance but overall there is quite good correlation even with the magnitudes of the currents.

This first acceleration test conducted without any load torque proved that the constructed test bench worked fine without any major problems at least when the

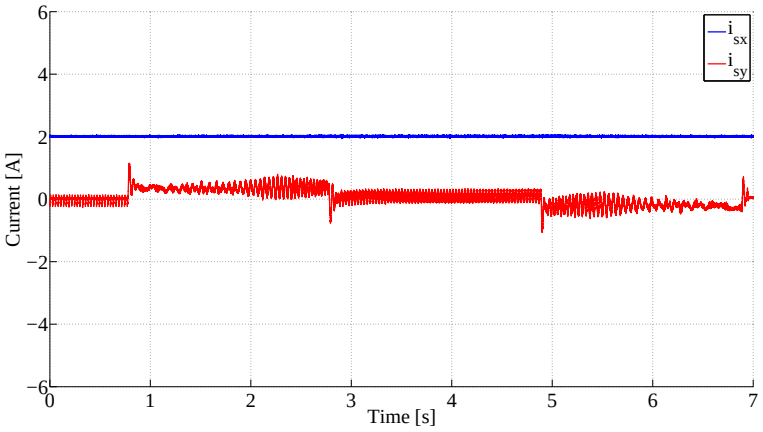

Figure 4.5: Measured stator currents expressed in rotor flux reference frame.

motor was not loaded. The next step was to examine how the load motor worked and how the load torque affected the motor operation, response and stability. This was conducted in the next measurement section.

4.2 Load torque step change

As in the previous section these, test drive settings were arranged similarly as in the simulation. However, since the grid converter control was not yet implemented the generator operation was not tested in this section. During this test, the motor was driven at a constant speed of 2000 rpm and then a a torque step of 3 Nm was applied to the shaft with the load motor. After the speed had stabilized a torque step back to zero was conducted.

Figure 4.6 shows the measured shaft torque. As can be seen the step change at the load is applied at approximately 1.2 s and step back to zero at 6.2 s.

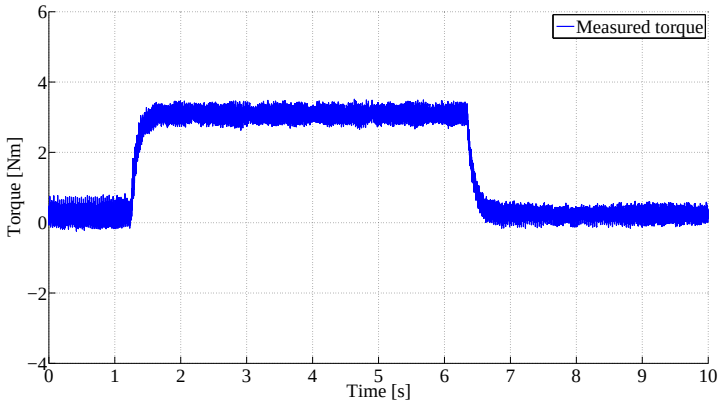

Figure 4.6: Measured torque at the shaft during load step test.

The step increases quite accurately to 3 Nm. However, the step is not infinite either when increasing or decreasing, but rather it seems to have some kind of filtering. The fact that the load torque is generated using another induction motor will always have effect on the torque response. The load step increase rate will mostly be affected by the control of the inverter driving the load motor. However, it is almost impossible to physically create an ideal step torque load without overshoot and actually the step response in load created by the load motor in this measurement was rather good. Furthermore, the filtering time for torque reference input signal measurement in Vacon can be decreased and even completely removed and this would make the response faster. During this measurement case the filtering time was 100 ms.

Figure 4.7 shows the extended view of reference and measured speed during the complete measurement period. From the measurements it can be stated that the control manages to retain the reference speed quite accurately as in the simulation results. However, the time from the torque step back to steady-state value demands almost 1 s compared to the 0.2 s in simulation. One reason for this might be the fact that in the simulation only the moment of inertia of one motor was taken into account, whereas during the real situation there was two motors and the torque transducer as well as couplers connected to the same shaft. During transition back to zero load the response is notably faster.

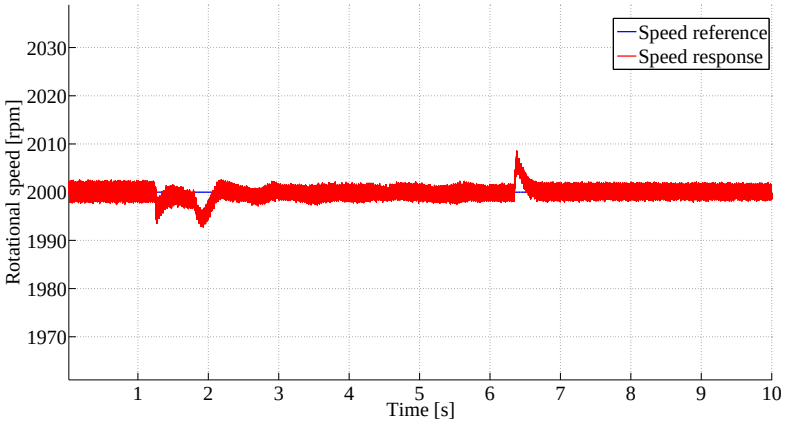

Figure 4.7: Speed reference and measured speed during load step test.

Figure 4.8(a) shows the measured three-phase stator currents during the complete period and Figures 4.8(b) and 4.8(c) show the currents during transition from no-load to 3 Nm load and vice versa respectively. As can be noticed from these figures applying load torque increases the current. The rather slow response can also be seen in here since it takes approximately 1 second before current has reached the higher value required to compensate the 3 Nm load. The amplitude of the current under loaded situation is slightly below 4 A and this corresponds to the simulations

quite well.

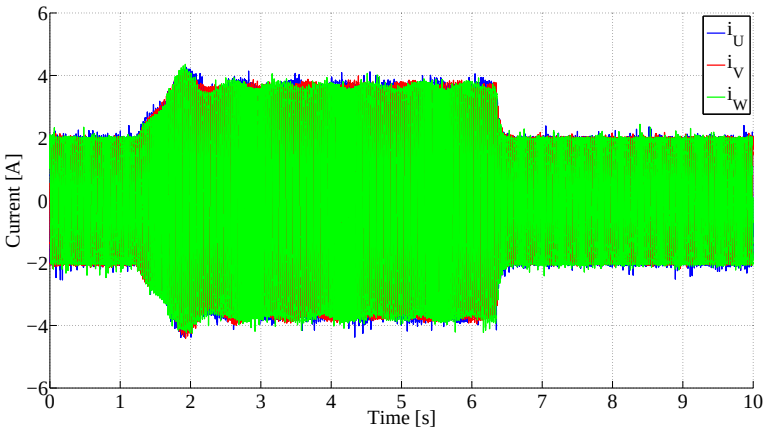

(a)

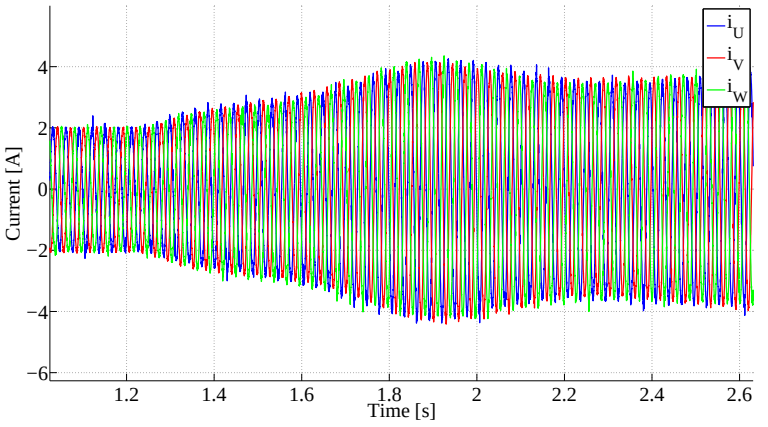

(b)

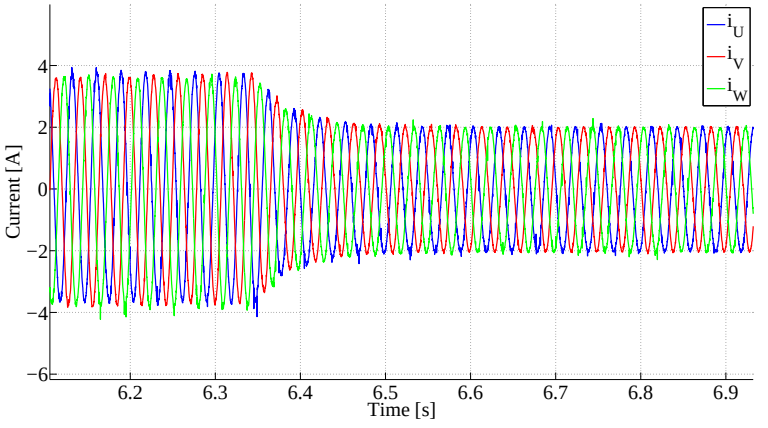

(c)

Figure 4.8: Measured three phase currents during (a) entire measurement period, (b) load step from 0 Nm to 3 Nm and (c) load step from 3 Nm to 0 Nm.

Figure 4.9 presents the stator current transformed into space vector components in rotor flux coordinates. Blue is i_{sx} and red i_{sy}. Again the blue is staying constant the whole measurement period because the rotational speed is below nominal and motor operates at constant flux region. The effect on load step can be seen in the i_{sy} current measurement. This current starts to increase immediately after the load has been applied in order to retain the reference speed. The response seems quite slow and the reason for this might be either too slow speed controller or current controller. The magnitudes here correspond well with the simulations but the response differs quite drastically.

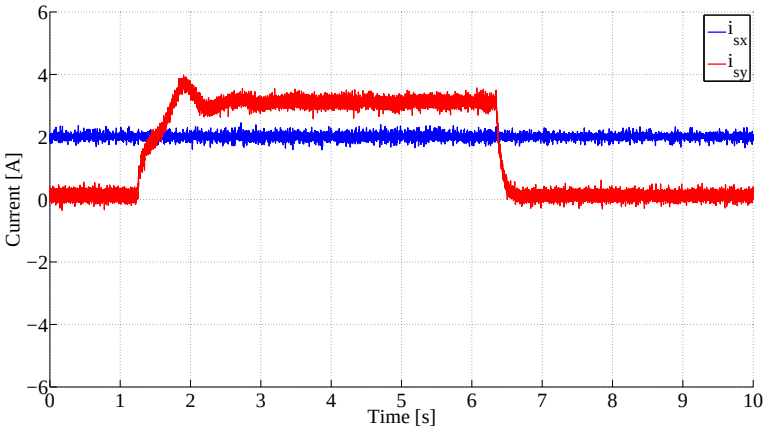

Figure 4.9: Measured stator currents expressed in rotor flux reference frame.

Even though there was some differences with simulations and the measurements, the test system itself functioned quite well. The load motor operated as supposed to and, furthermore, the control system could operate the motor well in loaded situation. In addition, the switching of the load converters did not cause any major disturbances. Next the motor operation with higher speeds could be tested and this is conducted in the next section.

4.3 Operation in field weakening region

This third section of this chapter presents the measurement results obtained from testing the motor drive above the nominal speed of the motor. First the motor was accelerated under no-load situation from stand still to 3100 rpm with a slope of 1000 rpm/s. When the motor had achieved the correct speed a load step from zero load to 3 Nm was conducted. And finally the torque was stepped down back to zero. This again follows the same type of test procedure as in the simulation but in this case the acceleration ramp was only 1000 rpm/s, whereas in the simulation it was 3000 rpm/s. The measured speed response with reference speed can be seen in

Figures 4.10(a) and 4.10(b). The first figure shows the whole period and the second is focused closer to enable better view.

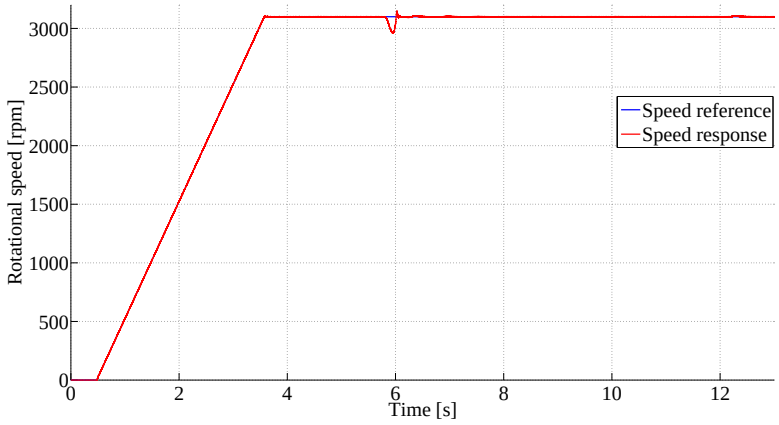

(a)

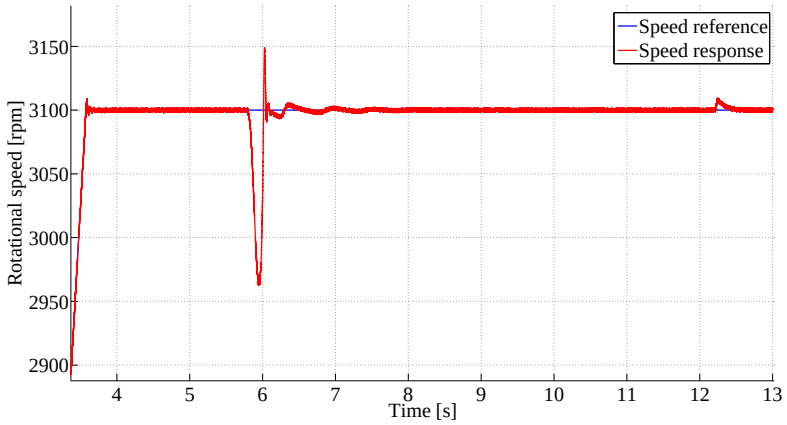

(b)

Figure 4.10: Speed reference and measured speed (a) during entire test period and (b) focused view during load torque changes.

The result is that control system is able to achieve the reference speed 3100 rpm without problems. However, the applied load step produces almost 140 rpm decrease on the speed before controller starts to react. Hence, this is significantly higher decrease compared to the simulation. However, the controller is able to recover and achieve the reference speed eventually after approximately 1 second. On the contrary, the step back to zero load does not affect the speed much and only increase of 8 rpm occurs after load change. Furthermore, reference speed is again achieved in 0.2 seconds. It seems that the simulation model becomes more inaccurate when the speed of the motor increases.

Figure 4.11 shows the measured shaft torque. The overshoot occurring at the speed can also be seen at the torque measurement. It is apparent during the peak

of slightly above 5 Nm at the torque measurement. By investigating the speed and the torque figures it seems that the load motor works as desired and the peaking is mainly due to the work motor control. Hence, there is room for improving the controllers.

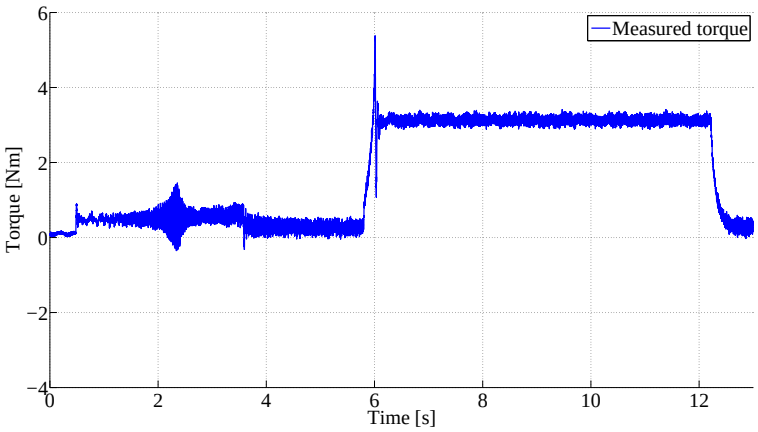

Figure 4.11: Measured torque at the shaft during field weakening region test.

Figures 4.12 - 4.13(b) present the measured three-phase stator currents. (a) presents the waveforms during the whole period, (b) during transition to field weakening area and (c) shows the currents after the load is applied. The overshoot noticed in both speed and torque measurements is also apparent in the measured currents. During the transition from no-load to 3 Nm current amplitudes hit 7 A shortly and this can be noticed more closely in Figure 4.13(b). Other remarkable thing occurs between 3 and 4 seconds when the motor moves to field weakening region. This is noticeable in the current as the amplitude decreases from 2.1 A to 1.9 A. The phenomena is shown closer in Figure 4.13(a).

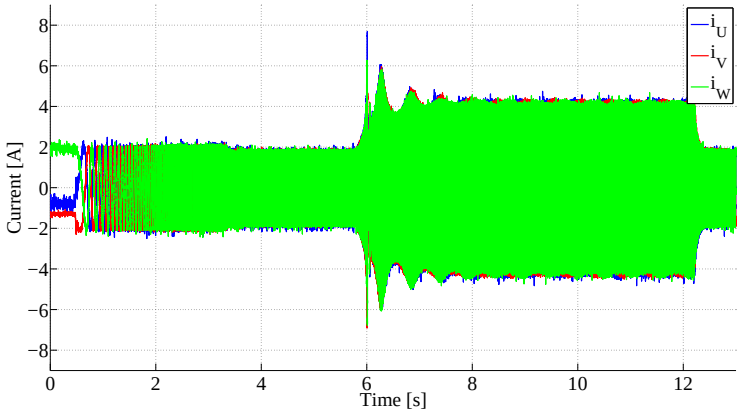

Figure 4.12: Measured three phase currents during entire field weakening region test.

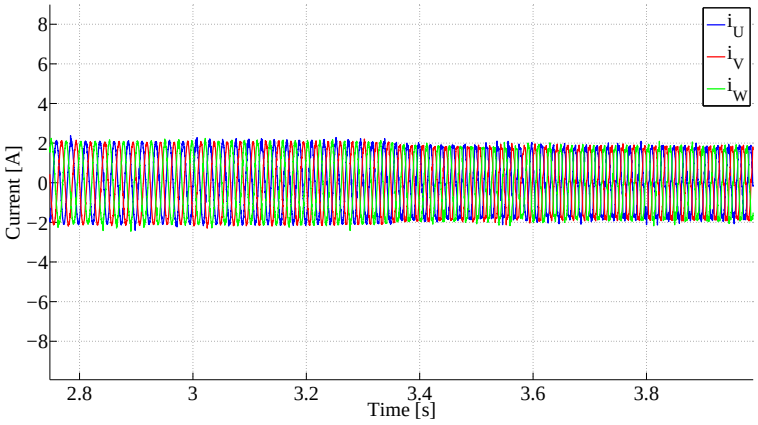

(a)

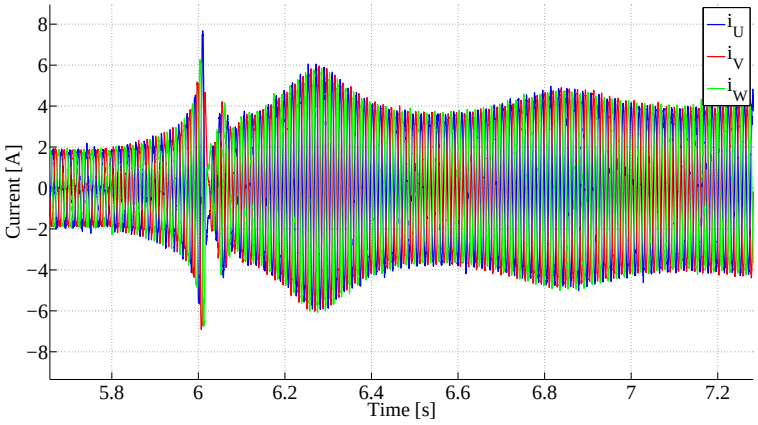

(b)

Figure 4.13: Measured three phase currents during (a) the transition to field weakening region and (b) load step at the field weakening region.

Figure 4.14 concludes the measurement results by presenting the stator current space vector components in rotor flux reference frame. During this test case, the current component i_{sx} responsible for flux generation does not stay constant, because the motor is operating in field weakening region. The change in this current is not significant but it can still clearly be seen from the figure. The large deviations that were noticed in the three-phase currents can mainly be detected in current i_{sy}. Apart from the higher deviation in the measured quantities, the results obtained from this section are still quite similar with the simulation results. The measurement results presented here conclude the measurements conducted with this test bench. Next section will finalize this chapter by evaluating the obtained measurements and giving some conclusions.

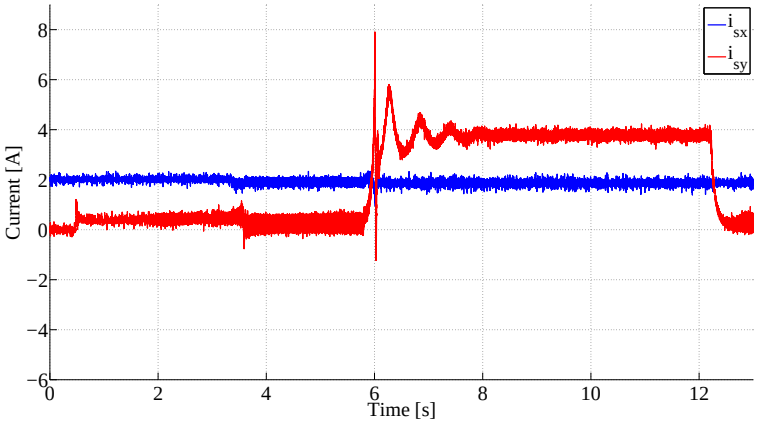

Figure 4.14: Measured three-phase currents expressed in space vector components in rotor flux reference frame.

4.4 Evaluation

The results obtained from the measurements indicate that this test system is working as expected. Of course as almost always, there is room for improvements. This section evaluates the functionality of three main measurement regarding the electric motor operation. These include motor current, speed and torque measurements.

As already stated in the beginning of this section, the currents obtained from dSPACE measurements are filtered with passive low-pass circuit with corner frequency at approximately 5 kHz. This combined with fact that the measurements are synchronized with the PWM modulator switching produces results suitable for control purposes. On the other hand if more research is desired for instance on the harmonic content of the motor currents, should this be conducted with an oscilloscope. However, during the control system teaching, the dSPACE measurements provide useful information of the practical design issues of control system design. For example the behaviour caused by not synchronizing the current measurements with the PWM on the operation of the control system can be studied in practice.

The speed measurement provided also good results. Since the control was able to work with the feedback and achieve the desired speed, there was no problems regarding incremental encoder operation. Furthermore, the angle calculated from incremental encoder pulses was correct since the control system was able to calculate the stator currents to space vector form and transform them into rotor flux reference frame for use for the current controller. During this measurement the 10000 kHz model update/measurement frequency did not produce problems since dSPACE actually reads each pulse from the encoder input regardless of the model update frequency. Therefore, the speed measurement was quite accurate with the

1000 puls/rev encoder.

The torque measurements obtained in this section seemed to include some noise. However, this measurement was a little difficult to verify due to the lack of any reference device. Hence, the measurement results provided by the manufacturer had to be trusted. However, during this section, the torque value obtained by measurements corresponded well with the reference value fed to the load motor inverter. Furthermore, the offset value seen at the torque was removed after the measurement tests.

These measurements indicated that the model used with the simulations worked mostly as predicted during the steady-state operation. However, slight difference between measurements and simulation results occurred during transient situations. One reason for this might be the fact that model used in this thesis was designed for induction motor with wound rotor structure. However, this probably induced only small differences. More significant differences between the model and the real system were probably caused by the simplifications made in the model. These were the neglect of iron losses, core saturation, harmonic content and the assumption that resistances and reactances remain constant. The two latter simplifications probably cause the most significant errors since the motor current actually contains a lot of harmonics and the rotor resistance is extremely temperature dependent. Furthermore, during the simulation, the three-phase inverter was ideally modelled which causes also differences compared to the real world system due to dead time, switching losses and non-finite rise time of the voltages.

In conclusion, the system itself functioned well. Furthermore, the motor model used in the course gives satisfying results when compared with the measurements. Even though differences occur, this laboratory test bench gives good experience for the students from the practical point of view and still the measurements are comparable with the simulations they perform with the models.

5. CONCLUSIONS

The objective for this thesis was to design and implement an induction motor drive test bench mainly for educational and also research purposes. The main purpose for this test system was to provide laboratory equipment for course DEE-34106 Modeling and Control of Electric Drives.

The work started by defining the fundamental features that the test bench had to fulfil. The most important factor is safety, since the system is used by students. This had to be considered during every step. Next important was that the test bench had to be small enough to enable easier relocation. And the final criterion was the integration with Matlab Simulink to enable effortless use for students.

With these criteria, small 2.2 kW induction motors were chosen together with Vacon converters as the main components. Furthermore, dSPACE DS1103 and CP1103 were selected for the control interface due to integration with Simulink and user friendly experiences of using. The next step was to simulate the operation of the system using parameters from the main components. This was conducted with the induction motor model and vector control system model which are used in the course mentioned above. In addition of giving results to support the test bench design, the use of the same model as in the course provided the confirmation that is possible to design the real control using the model. Hence, students would be able to successfully test their design with the test system.

Design and construction was then implemented based on these simulations. This included the fabrication of current measurement circuits for the grid and motor side, DC-bus and grid voltage measurement circuits and DC power supply for these. Furthermore, incremental encoder and torque transducer were purchased. In addition to the measurement circuitry, also the PWM control signals required an optical transmitter circuit and load motor controller board was also constructed. Finally these components were installed into a single test bench structure and connected to dSPACE system. After the hardware construction phase had been completed, the dSPACE control system was designed based on the previously built Simulink model by replacing the induction motor vector model with real life current, speed and angle measurements using the proper RTI blocks. At this stage the control for grid converter was neglected and postponed for later.

After everything above had been successfully implemented, three different tests

were conducted. These included tests for validating motor operation during the speed reference change, load torque change and field weakening situations. Measurements were done and the results were studied and compared with the simulations. At this stage, the test bench was noticed to work as expected. However, some differences with the simulations were also stated.

As a result, a valid induction motor test system was developed. In my opinion, this test bench provides effortless testing equipment which will offer students a possibility to broaden their knowledge regarding motor drive control design and verification in practice. In addition to teaching purposes, this system also provides potential to motor control research. Now that the complete system has been implemented the verification of different control algorithms is easy and requires very little time. In the future, this system is quite easy to be further developed and for example, due to its modularity, different components can be added and replaced with small effort. Regarding the future usage of the test bench, I think the it will be focused mainly on teaching purposes and less research is conducted. However, in conclusion my opinion is that this test system provides a nice addition to the laboratory teaching equipment repertoire of the Department of Electrical Engineering at Tampere University of Technology.

REFERENCES

[1] Waide, P., Brunner, C.U., 2011, Energy-Efficiency Policy Opportunities for Electric Motor-Driven Systems, International Energy Agency, 128 p.

[2] Hughes, A., Drury, B., 2013, Electric Motors and Drives (Fourth Edition), Newnes, Boston.

[3] Binns, K.J., Dye, M., 1970, Effects of slot skew and iron saturation on cogging torques in induction machines, Proceedings of the Institution of Electrical Engineers, vol.117, no.7, pp.1249-1252.

[4] Bastman, J., TEL-1130 Sähkökoneet Opintomoniste, 2011, Tampereen teknillinen yliopisto.

[5] Espinoza, J.R., 2011, Power Electronics Handbook (Third Edition), by Muhammad H. Rashid, Chapter 15 - Inverters, Butterworth-Heinemann, Boston, 357-408 p.

[6] Veltman, A., Pulle, D.W.J., De Doncker, R.K. 2007. Fundamentals of Electrical Drives, (Second Edition), Dordrecht, Springer. 356 p.

[7] Bennett, N., Wang, J., Shimmin, D.W., Binns, K.J., 1993, A new vector control scheme for an adjustable speed AC drive system utilising a high field permanent magnet synchronous machine, Sixth International Conference on Electrical Machines and Drives, (Conf. Publ. No. 376) , vol.121, no.126, pp.8-10.

[8] Vas, P., 1998, Sensorless Vector and Direct Torque Control, Oxford University Press, Inc., New York, p. 729.

[9] Vas, p., 1992, Electrical Machines and Drives: A Space-Vector Theory Approach, Oxford University Press, Inc., New York, p. 799.

[10] Liserre, M., Blaabjerg, F., Dell′Aquila, A. 2004. Step-by-step design procedure for a grid-connected three-phase PWM voltage source converter, International Journal of Electronics, pp.445-460.

[11] Liserre, M., Blaabjerg, F., Hansen, S., 2005. Design and control of an LCL-filter-based three-phase active rectifier, IEEE Transactions on Industry Applications, vol.41, no.5, pp.1281-1291.

[12] Vinay Kumar, T., Srinivasa Rao, S., 2010, Switching State Algorithm for Space Vector Pulse Width Modulation (SVPWM), 7th Mediterranean Conference and Exhibition on Power Generation, Transmission, Distribution and Energy Conversion, vol. 1, no. 6, pp. 7-10.

[13] Zhou, K., Wang, D., 2002, Relationship between space-vector modulation and three-phase carrier-based PWM: A comprehensive analysis, IEEE Trans. Ind. Electron., vol. 49, pp. 186-196.

[14] Monti, A., Santi, E., Dougal, R.A., Riva, M., 2003, Rapid prototyping of digital controls for power electronics, IEEE Transactions on Power Electronics, vol.18, no.3, pp.915-923,

[15] dSPACE GmbH, 2013, DS1103 PPC Controller Board: Hardware Installation and Configuration For Release 2013-B, Paderborn, Germany.

[16] dSPACE GmbH, 2013, RTI and RTI-MP Implementation Guide For Release 2013-B, Paderborn, Germany.

[17] Hemminki, P., 2005, Vaihtosuuntaajan ohjaus dSPACE:lla, Diplomotyo, Tampereen teknillinen yliopisto, Tehoelektroniikan laitos, 86 s.

A. INDUCTION MOTOR DRIVE SIMULINK MODEL

The voltage equations in an arbitrary reference frame introduced in (2.23) and (2.24) can be divided into real and imaginary components presented in (A.1)-(A.4).

$$u_x = \frac{R_s}{L'_s}\psi_x - \omega_k\psi_y + \frac{d\psi_x}{dt} - k_r\frac{R_s}{L'_s}\psi_u \tag{A.1}$$

$$u_y = \frac{R_s}{L'_s}\psi_y - \omega_k\psi_x + \frac{d\psi_y}{dt} - k_r\frac{R_s}{L'_s}\psi_v \tag{A.2}$$

$$u_u = \frac{R_r}{L'_r}\psi_u - (\omega_k - \omega)\psi_v + \frac{d\psi_u}{dt} - k_s\frac{R_r}{L'_r}\psi_x \tag{A.3}$$

$$u_v = \frac{R_r}{L'_r}\psi_v + (\omega_k - \omega)\psi_u + \frac{d\psi_v}{dt} - k_s\frac{R_r}{L'_r}\psi_y, \tag{A.4}$$

where subscripts x, y, u and v denote stator real, stator imaginary, rotor real and rotor imaginary components respectively. Furthermore, the stator and the rotor inductances, L'_s and L'_r, are defined by (A.5)-(A.6).

$$L'_s = L_s - \frac{L_m^2}{L_r} \tag{A.5}$$

$$L'_r = L_r - \frac{L_m^2}{L_s}, \tag{A.6}$$

where self-inductances of the stator and the rotor are

$$L_s = L_{s\sigma} + L_m \tag{A.7}$$

$$L_r = L_{r\sigma} + L_m, \tag{A.8}$$

which by substituting L_s with (A.7) and L_r with (A.8), yields (A.9) and (A.10).

$$L'_s = L_{s\sigma} + \frac{L_{r\sigma} L_m}{L_{r\sigma} + L_m} \tag{A.9}$$

$$L'_r = L_{r\sigma} + \frac{L_{s\sigma} L_m}{L_{s\sigma} + L_m} \tag{A.10}$$

These inductances can be then calculated with the known leakage and magnetizing inductances. Furthermore, the variables k_s and k_r are stator and rotor coefficients respectively and defined by (A.11) and (A.12).

$$k_s = \frac{L_m}{L_s} \tag{A.11}$$

$$k_r = \frac{L_m}{L_r} \tag{A.12}$$

Similarly as the voltage equations also the flux equations introduced in (2.25) and (2.26) can be divided into real and imaginary components.

$$\psi_x = L_s i_x + L_m i_u \tag{A.13}$$

$$\psi_y = L_s i_y + L_m i_v \tag{A.14}$$

$$\psi_u = L_s i_u + L_m i_x \tag{A.15}$$

$$\psi_v = L_s i_v + L_m i_y \tag{A.16}$$

Furthermore, equation of motion and equation of electromechanical torque are presented in (A.17) and (A.18) respectively.

$$t_e = \frac{3}{2} p(\psi_x i_y - \psi_y i_x) \tag{A.17}$$

$$J\frac{d\omega}{dt} = t_e - t_l - B\omega, \tag{A.18}$$

where t_e is the electromechanical torque, t_l load torque applied to the motor shaft, J the moment of inertia, p number of pairs of poles, ω rotor rotational velocity and B damping coefficient. During simulations in this thesis, zero damping coefficient was used.

Equations (A.1)-(A.18) were used to construct the induction motor space-vector

model in stator reference frame in Simulink environment. Direct space-vector control in rotor flux reference frame was then implemented to the same model. Figure A.1 present the complete Simulink model and Figures A.2-A.11 the subsystems included in the model.

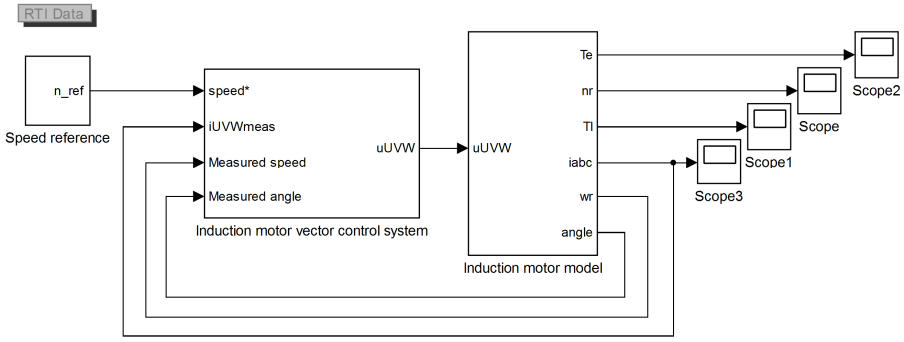

Figure A.1: Induction motor drive model Simulink implementation.

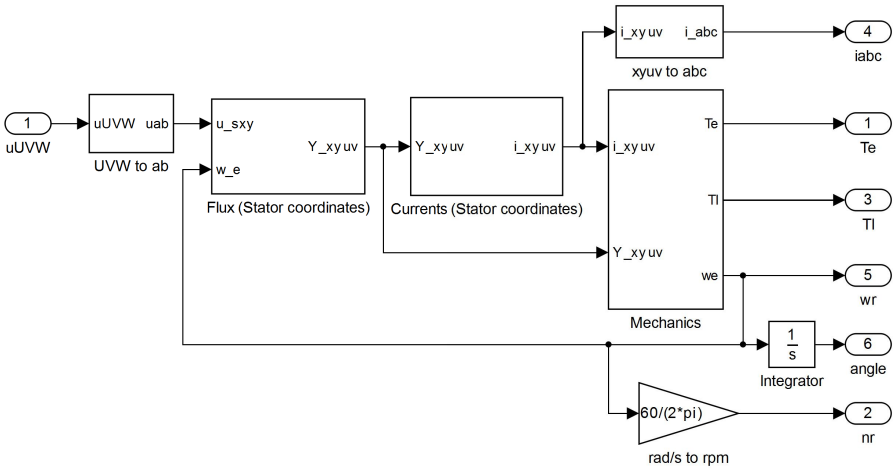

Figure A.2: Extended view of the 'Induction motor model'-subsystem which contains induction motor space-vector model implementation in stator reference frame.

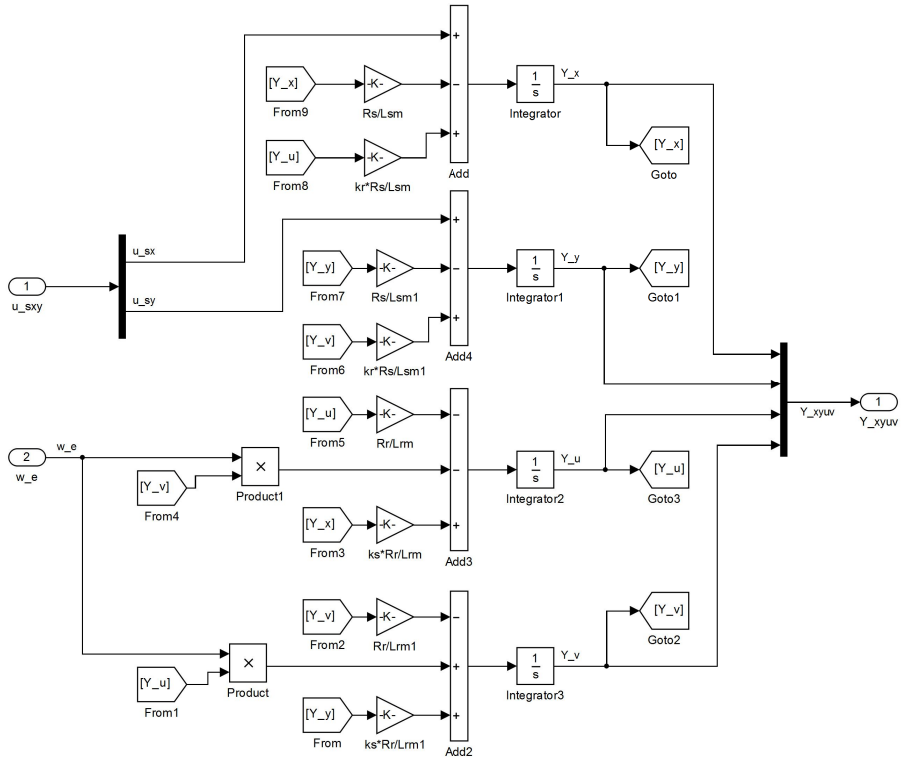

Figure A.3: Extended view of the 'Flux (Stator coordinates)'-subsystem.

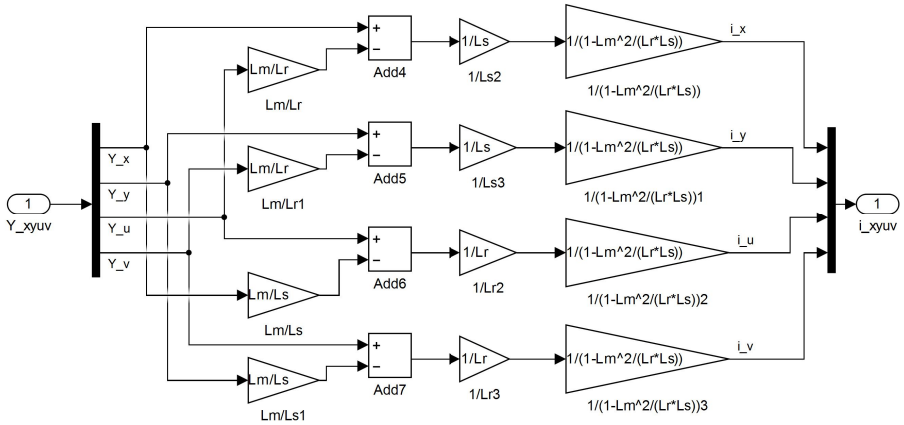

Figure A.4: Extended view of the 'Currents (Stator coordinates)'-subsystem.

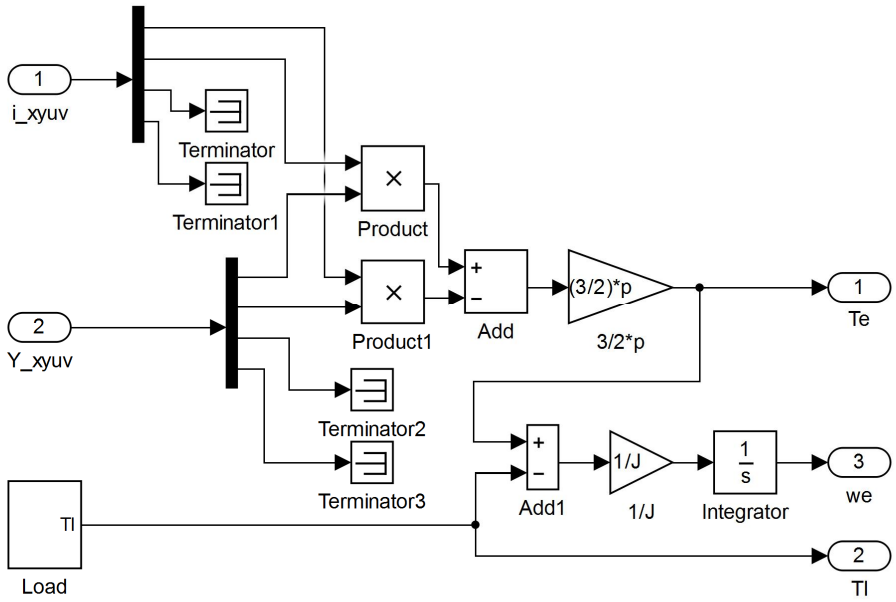

Figure A.5: Extended view of the 'Mechanics'-subsystem.

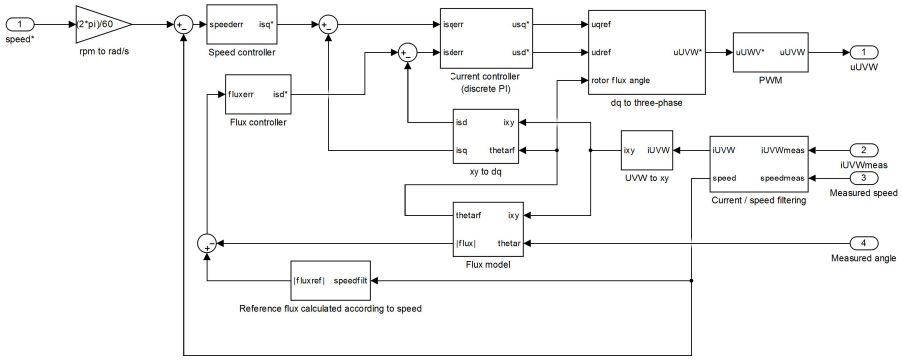

Figure A.6: Extended view of the 'Induction motor vector control'-subsystem. Contains implementation of the induction motor space-vector control system in rotor flux reference frame.

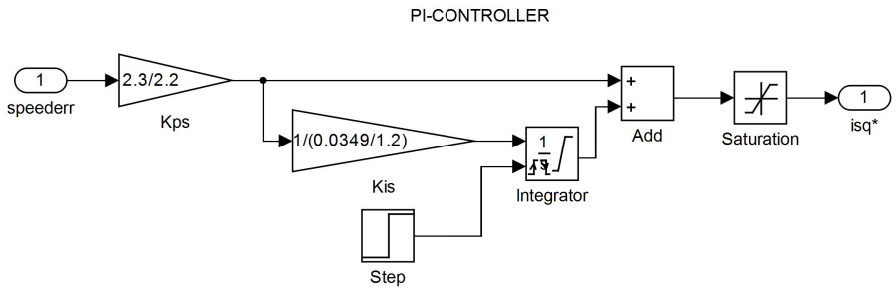

Figure A.7: Extended view of the 'Speed controller'-subsystem. Contains implementation of the PI controller used as speed, flux and current controller (different Kp and Ki).

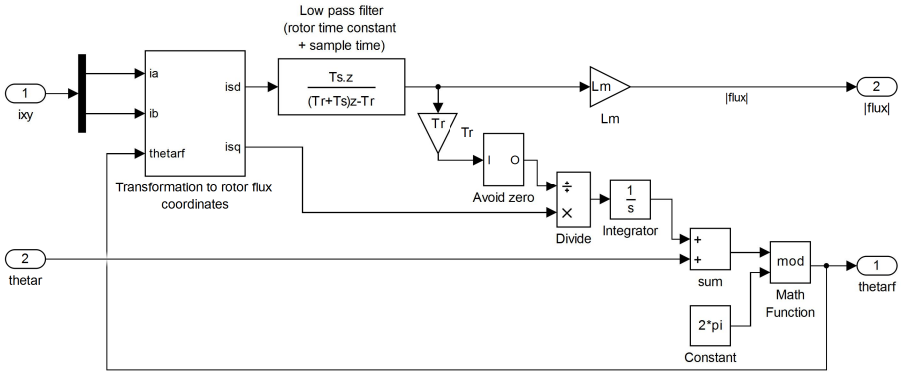

Figure A.8: Extended view of the 'Flux model'-subsystem. Used to calculate flux absolute value and flux angle by using measured currents ans measured rotor position.

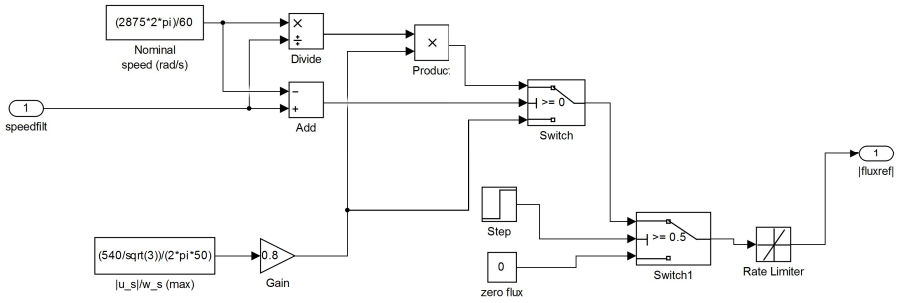

Figure A.9: Extended view of the 'Reference flux'-subsystem which is used to calculate the reference flux absolute value according to the measured speed.

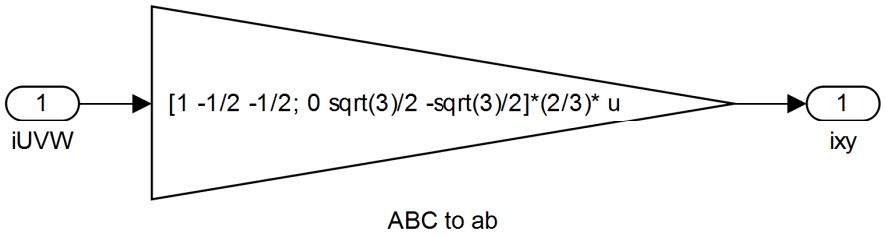

Figure A.10: Extended view of the 'UVW to xy'-subsystem which is used to perform Clarke's transformation.

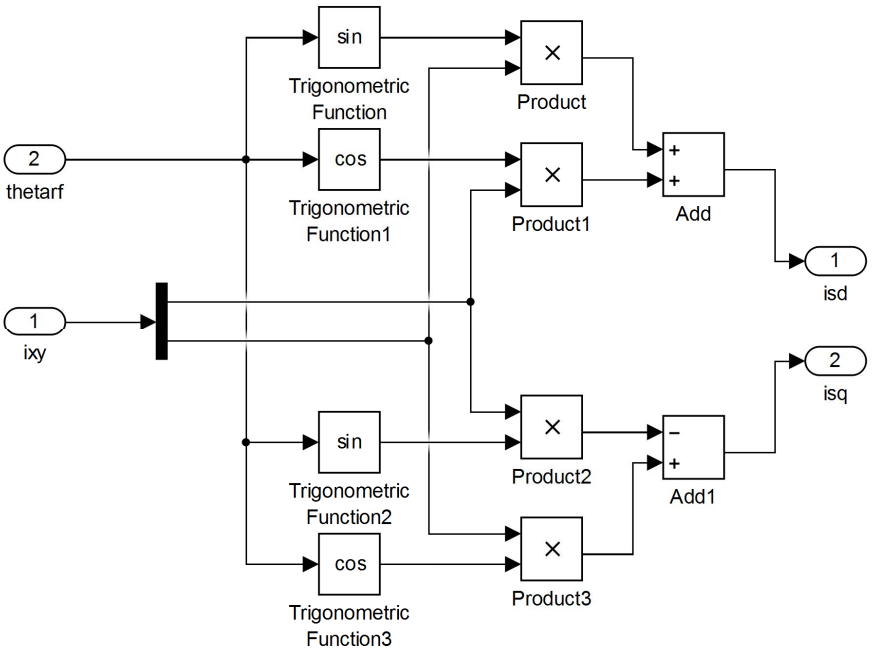

Figure A.11: Extended view of the 'xy to dq'-subsystem which is used to perform Park's transformation.

B. INDUCTION MOTOR DRIVE SIMULINK MODEL USED WITH DSPACE

After the test bench had been constructed, the Simulink model used to perform simulations had to be changed to make it function with the real-time measurements from the actual induction motor. The modified Simulink model is presented in Figure B.1. Subsystems for the grid converter control were also inserted, however, they were not used in this thesis.

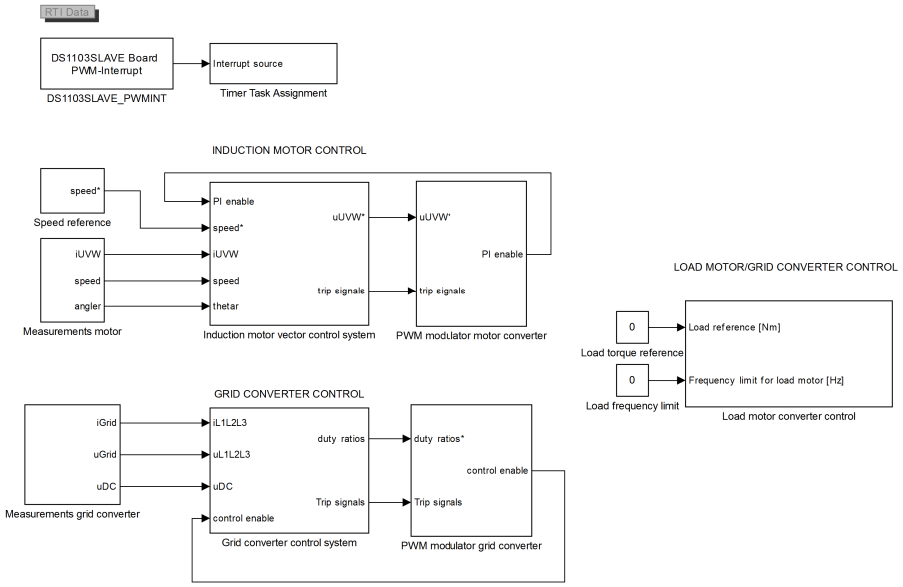

Figure B.1: Induction motor Simulink model used in the test bench with dSPACE DS1103.

The induction motor space vector model subsystem was removed and replaced with the subsystems 'Measurements motor' and 'PWM modulator motor converter'. The measurement subsystem contains the RTI blocks and coefficients required to scale the ADC input values to suit the control system. In addition to the current and torque ADC measurements, also the incremental encoder RTI blocks, which provide rotor angle and speed measurements, were added. Figure B.2 presents this subsystem.

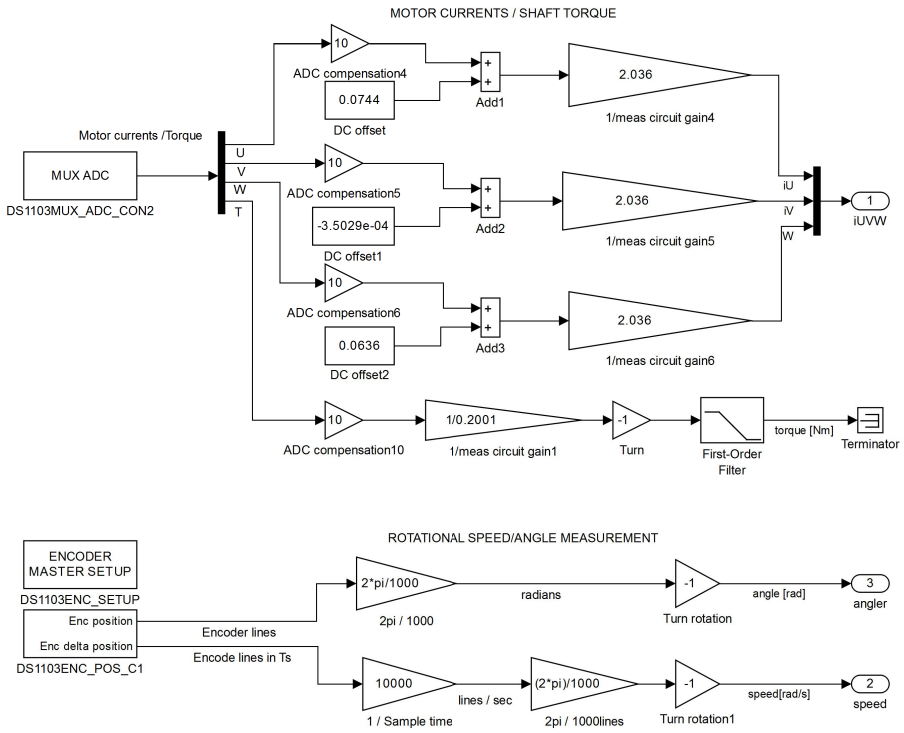

Figure B.2: Extended view of 'Measurements motor'-subsystem containing the RTI blocks for stator currents, shaft torque, rotor speed and rotor angle measurements.

The measurements provided feedback for the control system whereas the 'PWM modulator motor converter' was implemented to provide the pulses for the semiconductor switches. Hence, the control system output is transmitted to this subsystem and it will transform the control signals to suit the DSP PWM modulator. Furthermore, this subsystem contains the digital I/O interface for the Vacon enable signal. Figure B.3 presents this subsystem. The trip signal input seen in the figure is a safety feature which stops the converter modulation in case of over current or over speed. After tripping the model has to be built again with the C/C++ compiler to reset the trip signals. Furthermore, the 'PI enable'-output is providing start signal for the PI controllers (flux, speed, current). This is used to start the control system in the beginning of modulation, because else the controllers would saturate to their limits before the start up and problems would occur.

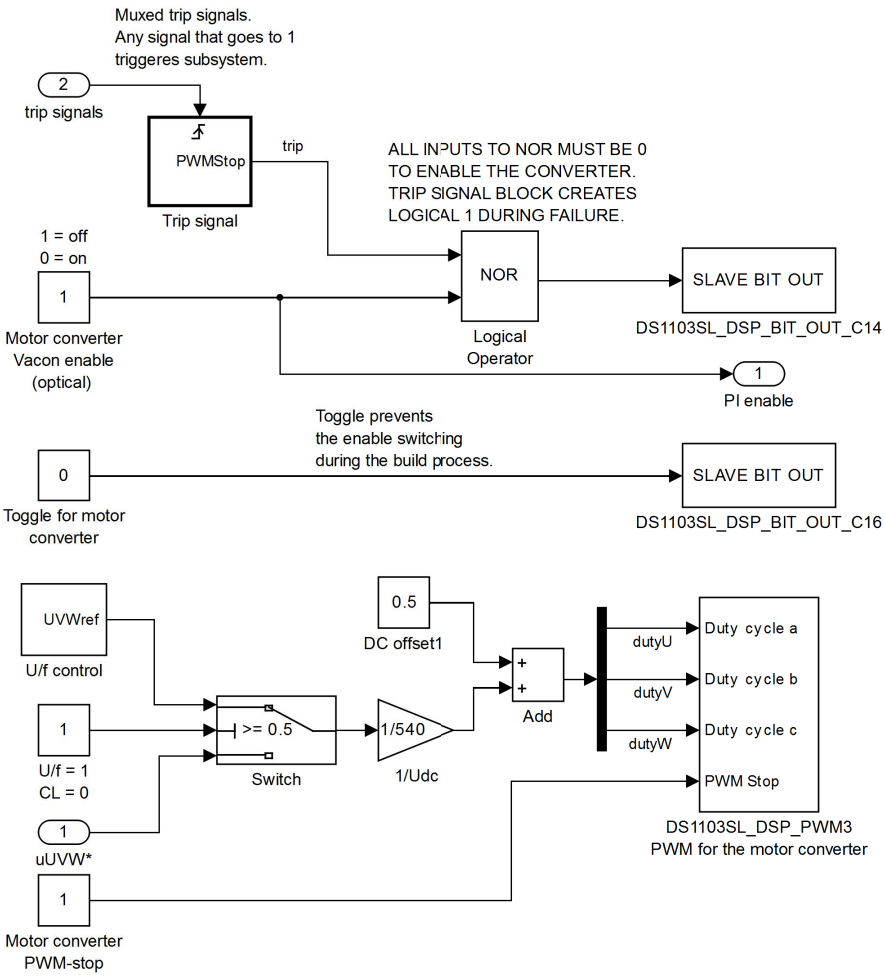

Figure B.3: 'PWM modulator motor converter'-subsystem containing the input for the DSP PWM modulator and enable signal for the converter.

Figure B.4 presents the over current and over speed detectors. The implementation is based on a simple comparator which sends a trip signal if either measured current or speed exceeds the limit set to the switch block. This signal is then transmitted to 'PWM modulator motor converter' subsystem which sets the enable signal to zero and modulation in the converter stops. However, the DSP modulator still continues to modulate but the references do not reach the IGBTs.

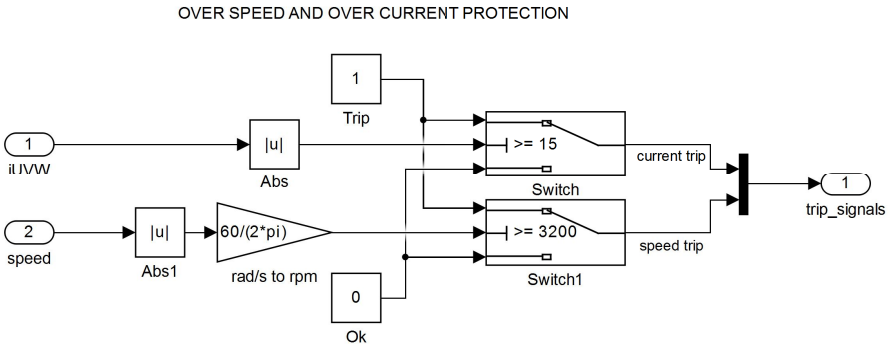

Figure B.4: Over current and over speed detection Simulink implementation.

Figure B.5 presents the 'Load motor converter control'-subsystem. This provides analogue load torque reference and speed limit reference for the load motor converter using dSPACE DAC RTI blocks. Furthermore, digital I/Os are used for start and stops signals of the motor and gird-side converters.

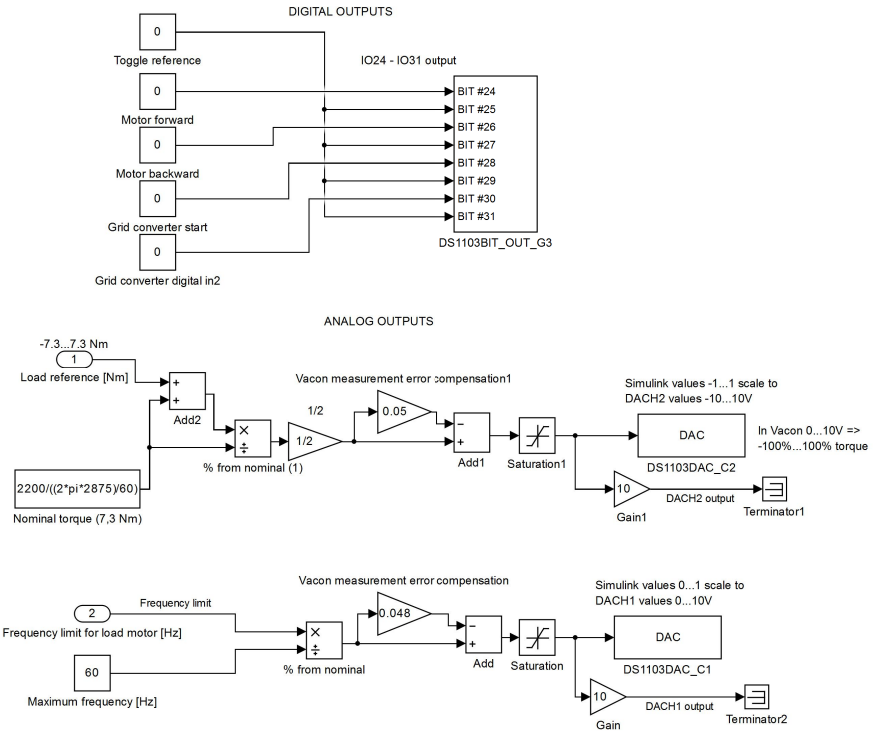

Figure B.5: Extended view of 'Load motor converter control' subsystem which provides load torque reference, speed limit, start and stop signals for the load motor converters.

C. EXTERNAL POWER SUPPLY LAYOUT DESIGN AND PHOTOGRAPH

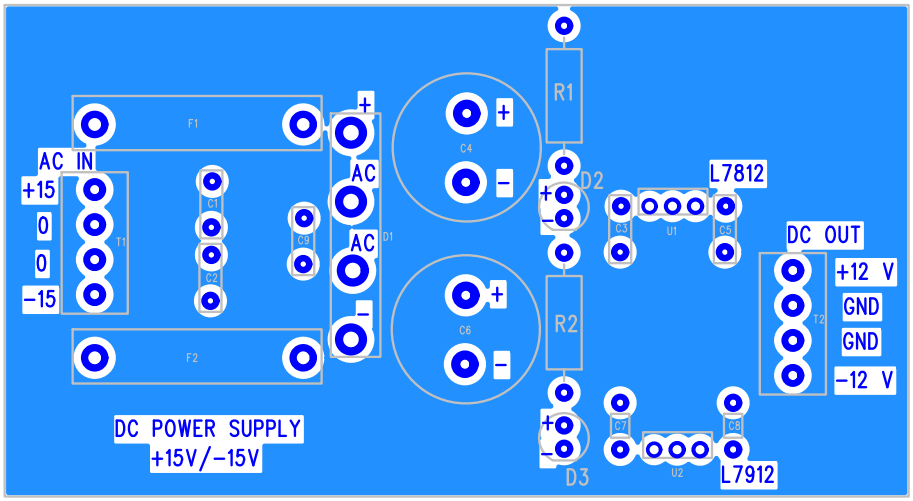

Figure C.1: $\pm 12V$ DC power supply board layout top view.

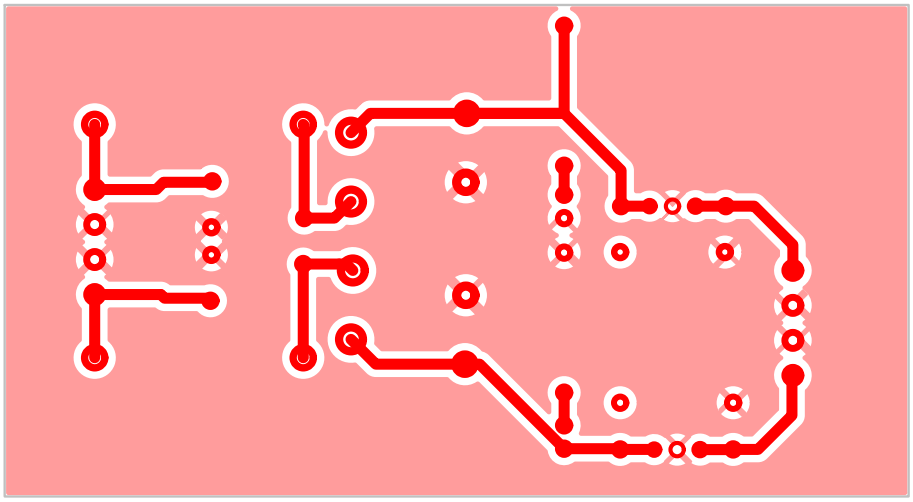

Figure C.2: $\pm 12V$ DC power supply board layout bottom view.

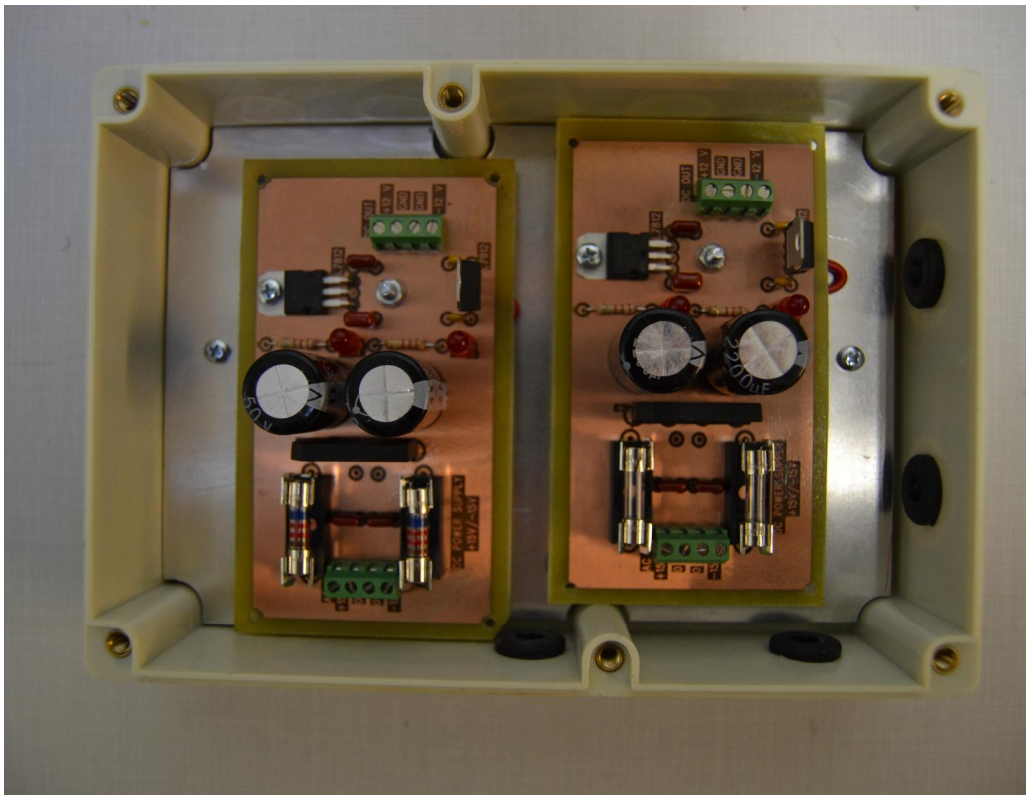

Figure C.3: Two soldered and finished $\pm 12V$ DC supplies without transformers.

D. CURRENT MEASUREMENT CIRCUIT LAYOUT DESIGN AND PHOTOGRAPH

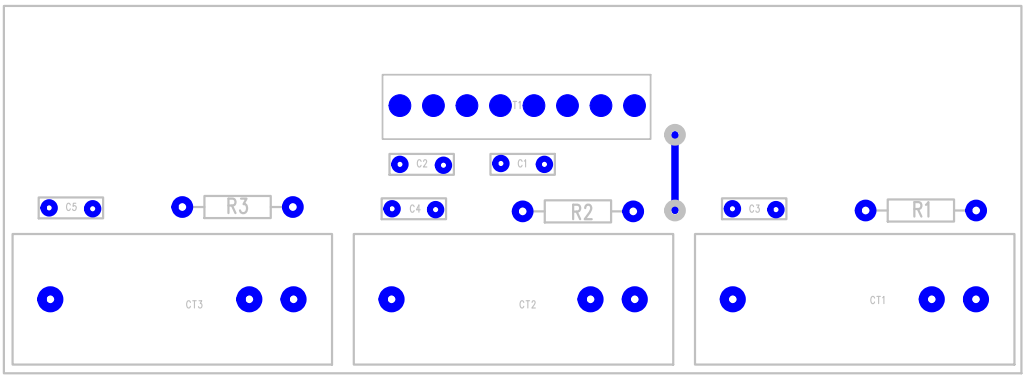

Figure D.1: Current measurement board layout top view.

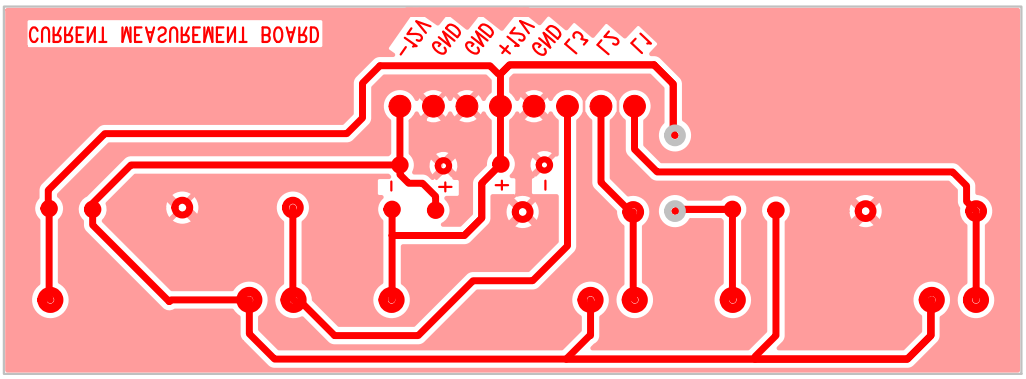

Figure D.2: Current measurement board layout bottom view.

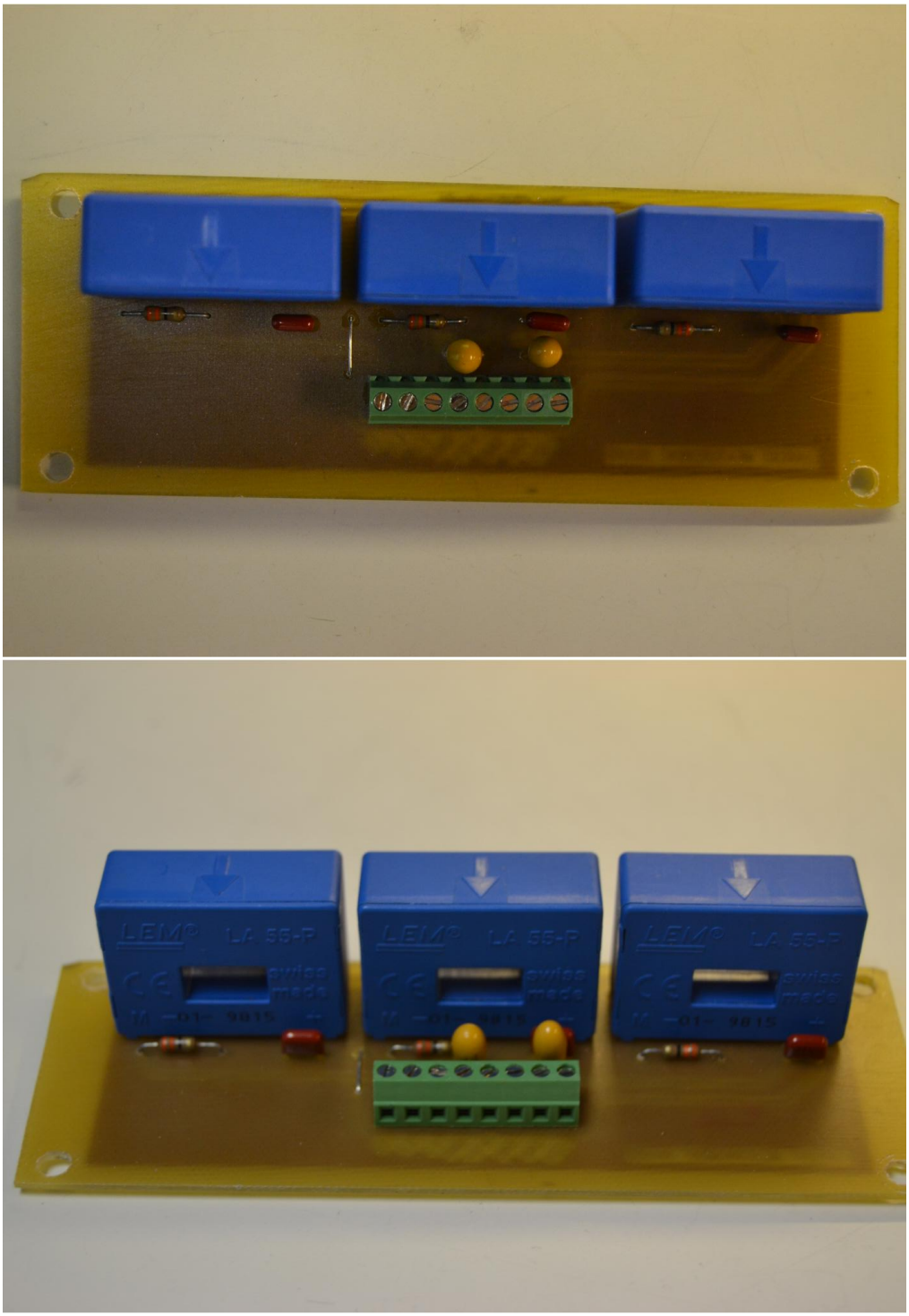

Figure D.3: Soldered and finished current measurement PCB top and front view.

E. BUFFER AND FILTER CIRCUIT LAYOUT DESIGN AND PHOTOGRAPH

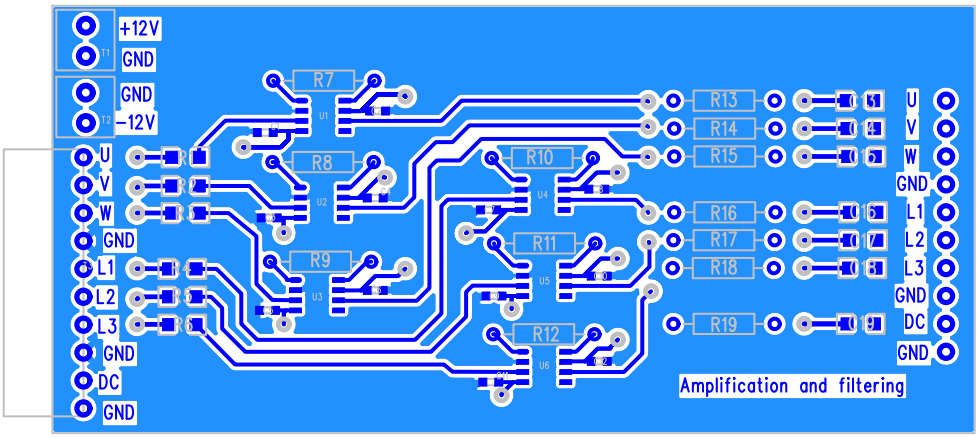

Figure E.1: Current and DC-voltage measurement buffer and filter board layout top view.

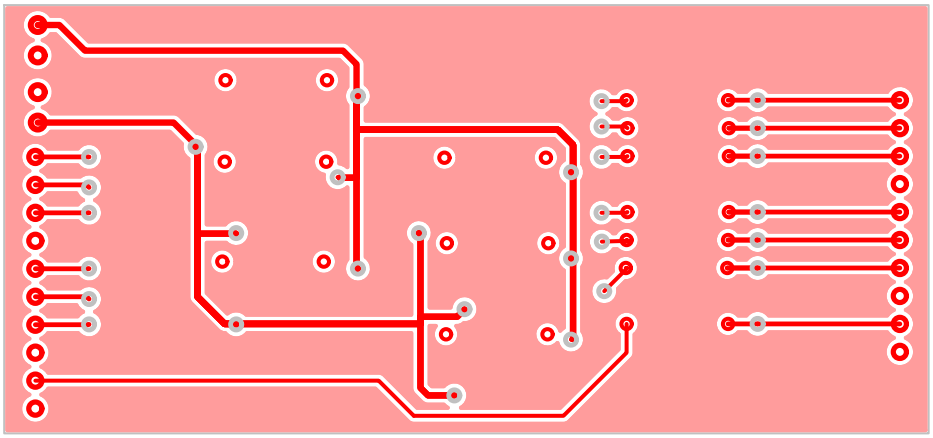

Figure E.2: Current and DC-voltage measurement buffer and filter board layout bottom view.

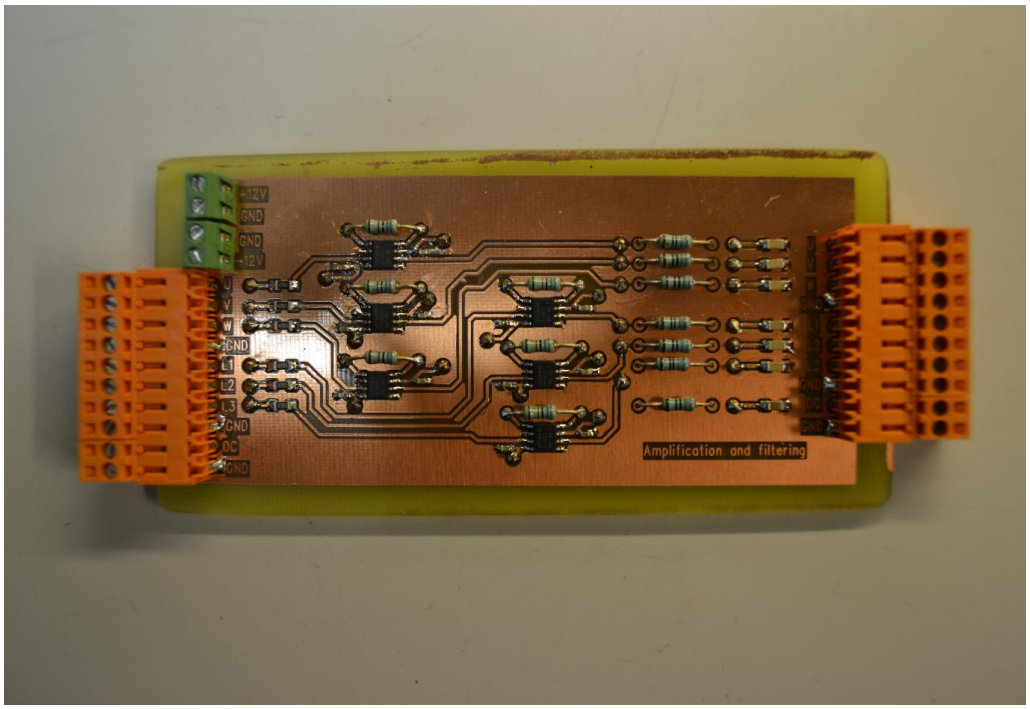

Figure E.3: Soldered and finished buffer and filter PCB.

F. DC-BUS VOLTAGE MEASUREMENT CIRCUIT LAYOUT DESIGN AND PHOTOGRAPH

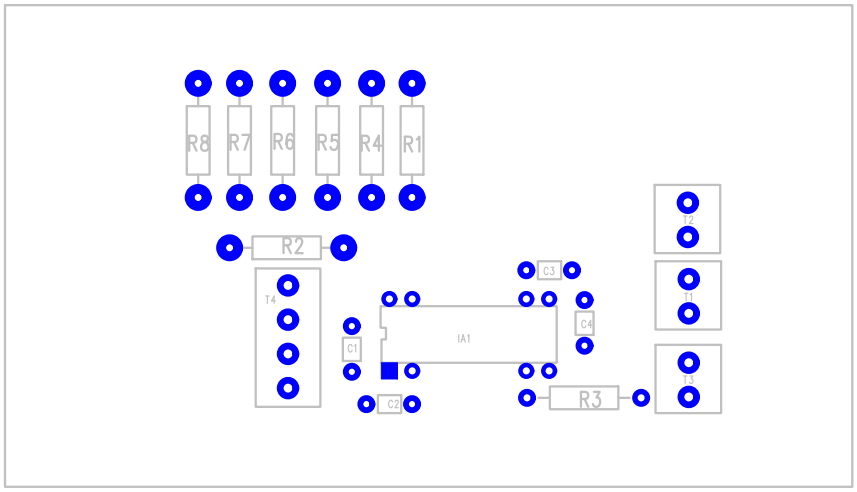

Figure F.1: DC-voltage measurement board layout top view.

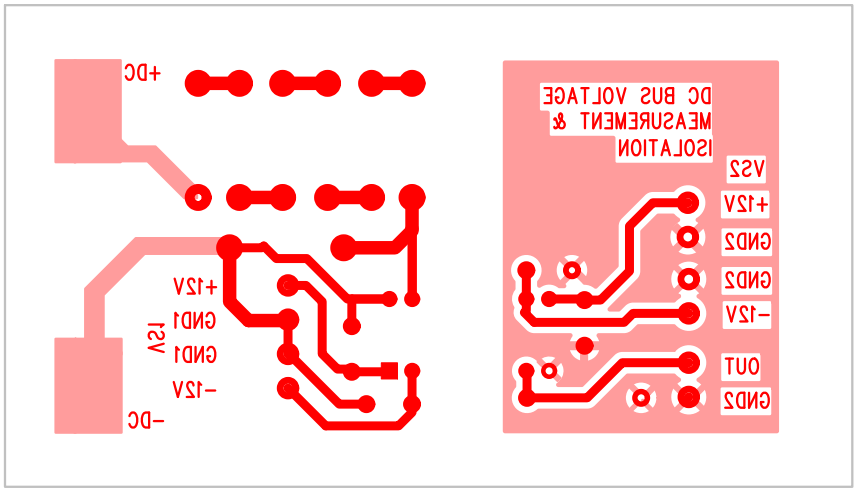

Figure F.2: DC voltage measurement board layout bottom view.

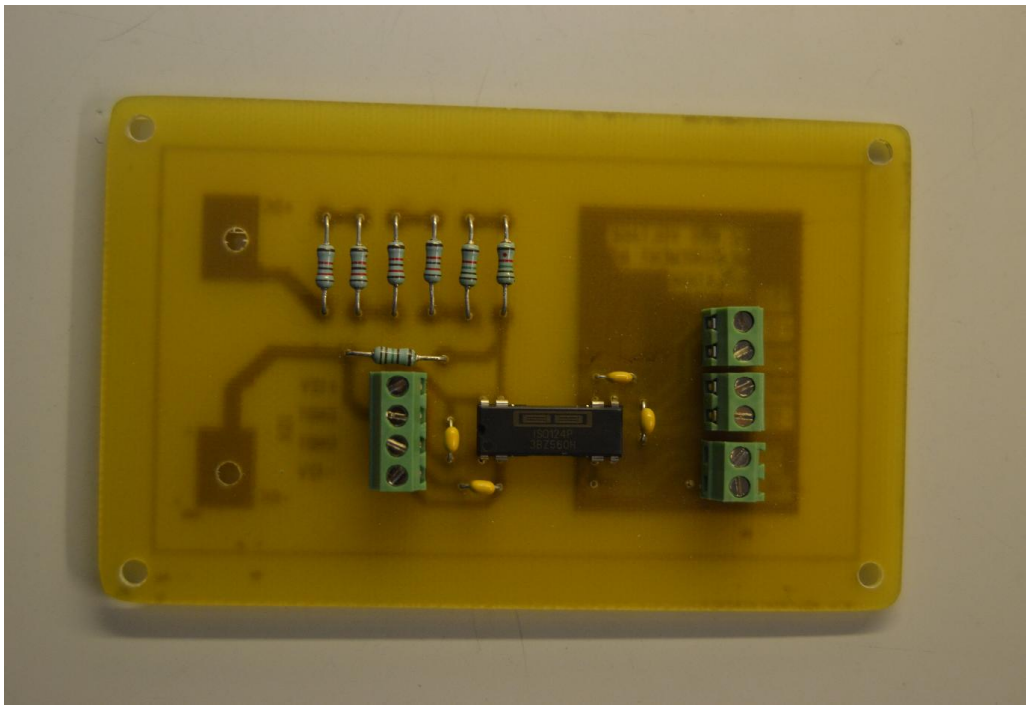

Figure F.3: Soldered and finished DC voltage measurement PCB.

G. GRID VOLTAGE MEASUREMENT CIRCUIT LAYOUT DESIGN AND PHOTOGRAPH

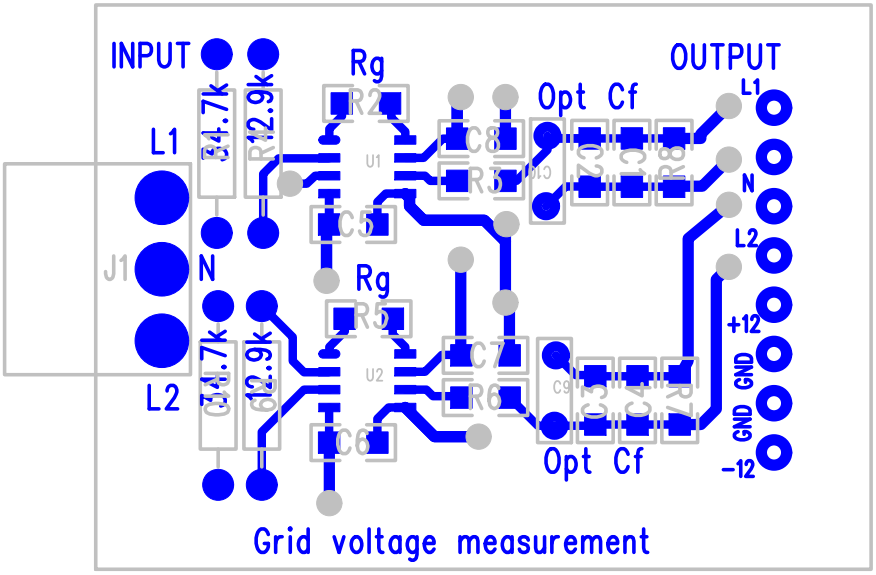

Figure G.1: Grid voltage measurement board layout top view.

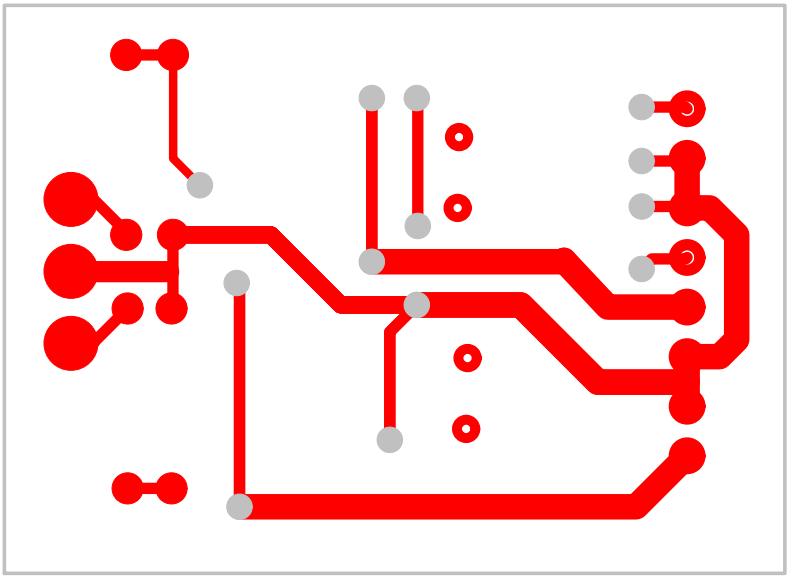

Figure G.2: Grid voltage measurement board layout bottom view.

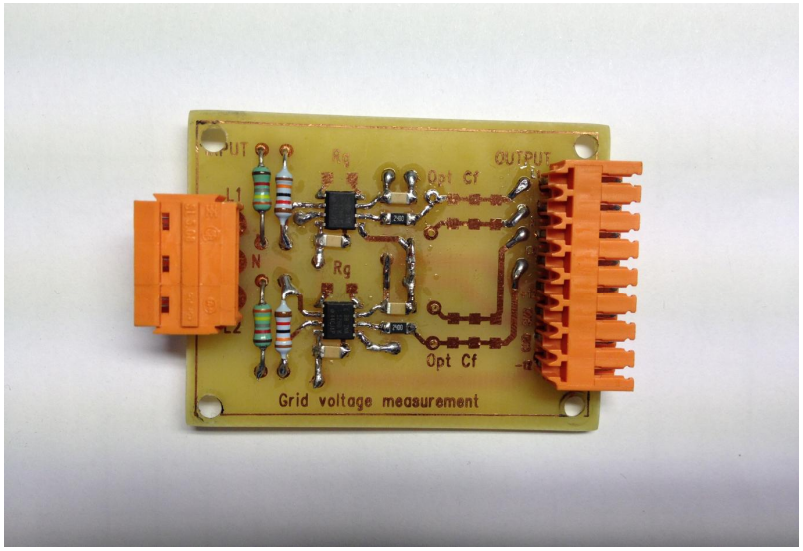

Figure G.3: Soldered and finished grid voltage measurement PCB.

Figure G.4: Measurement transformer used in grid measurement circuit.

H. TORQUE TRANSDUCER PHOTOGRAPH

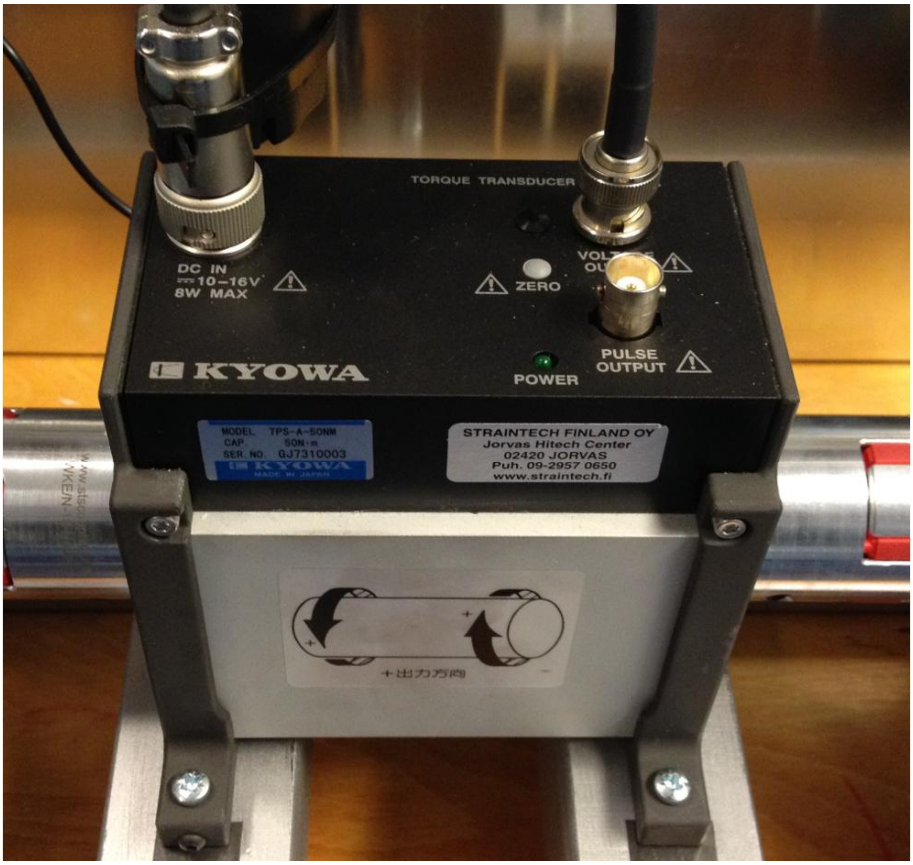

Figure H.1: Purchased torque transducer installed between the motors.

I. INCREMENTAL ENCODER PHOTOGRAPH AND INTERFACE LAYOUT DESIGN AND PHOTOGRAPH

Figure I.1: Purchased encoder connected to the motor shaft.

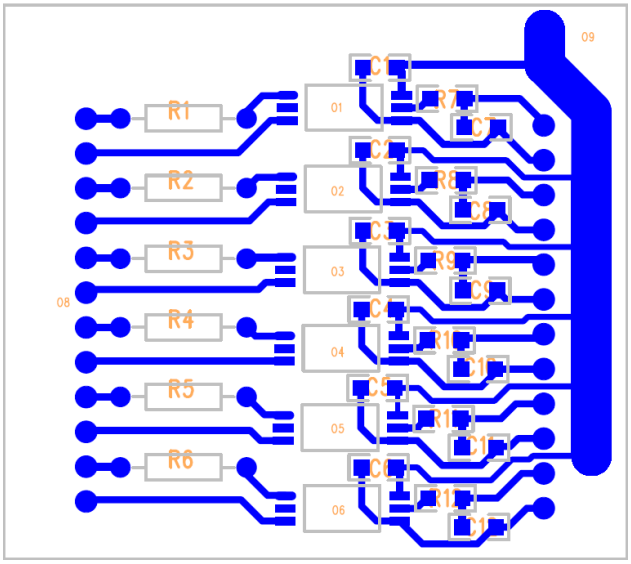

Figure I.2: Incremental encoder dSPACE interface board layout top view.

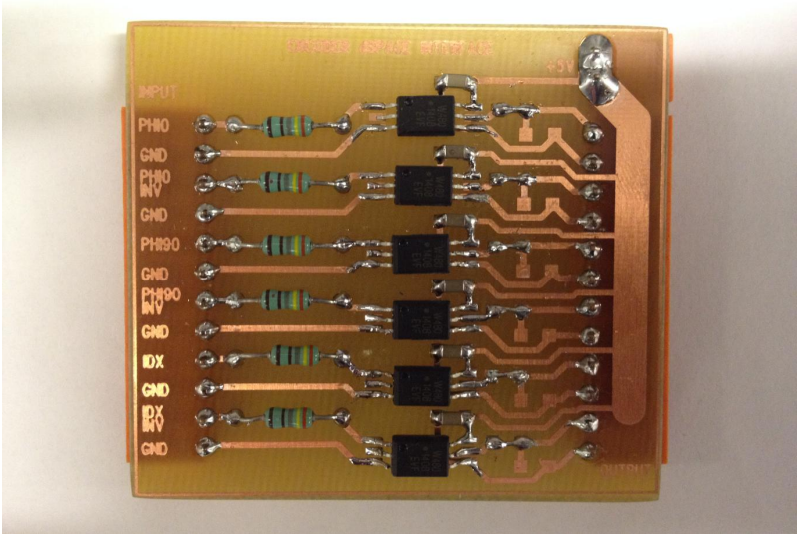

Figure I.3: Soldered and finished incremental encoder dSPACE interface PCB.

J. OPTICAL TRANSMITTER LAYOUT DESIGN AND PHOTOGRAPH

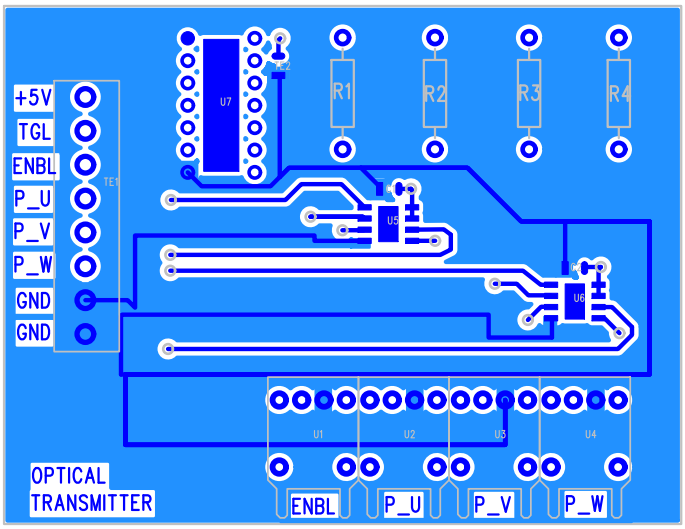

Figure J.1: Optical transmitter board layout top view.

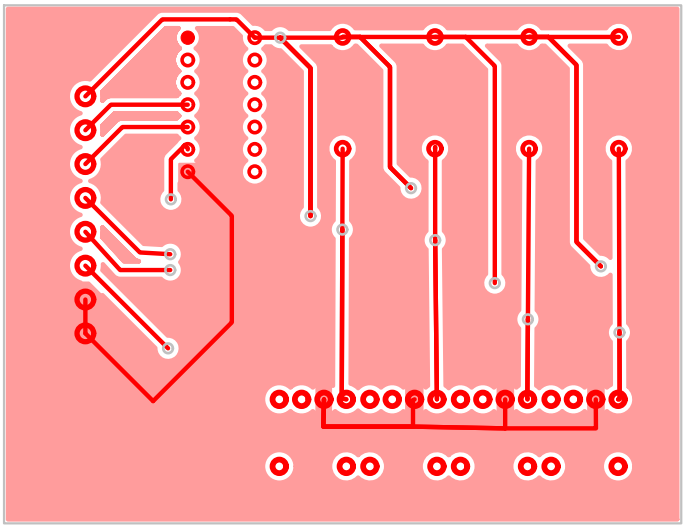

Figure J.2: Optical transmitter board layout bottom view.

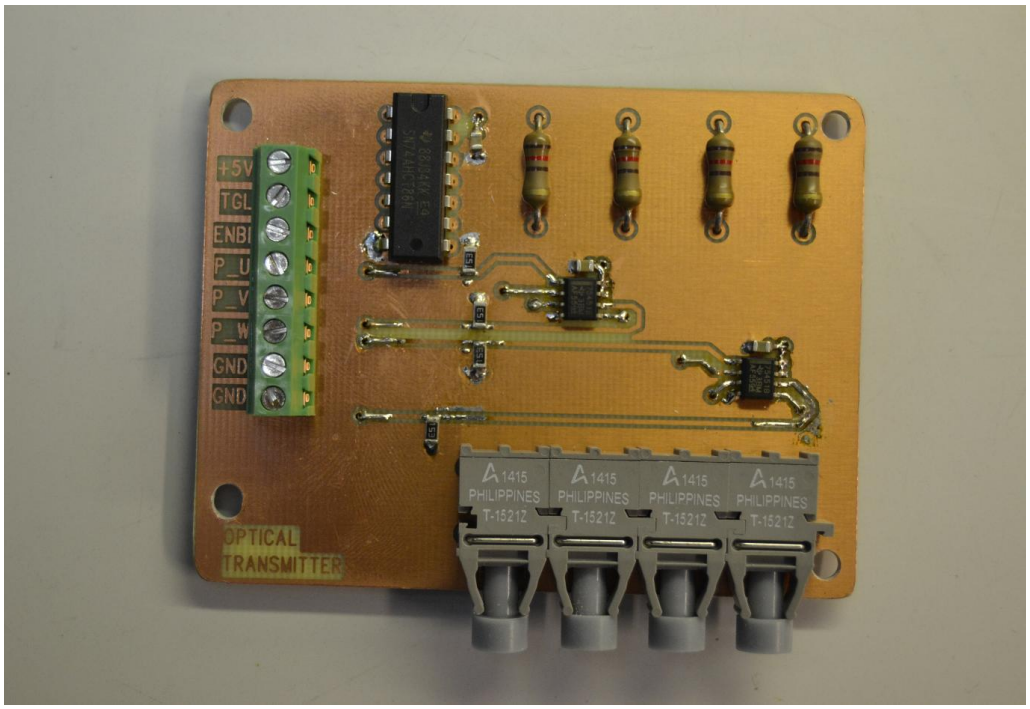

Figure J.3: Soldered and finished optical transmitter PCB.

K. LOAD MOTOR CONTROL INTERFACE LAYOUT DESIGN AND PHOTOGRAPH

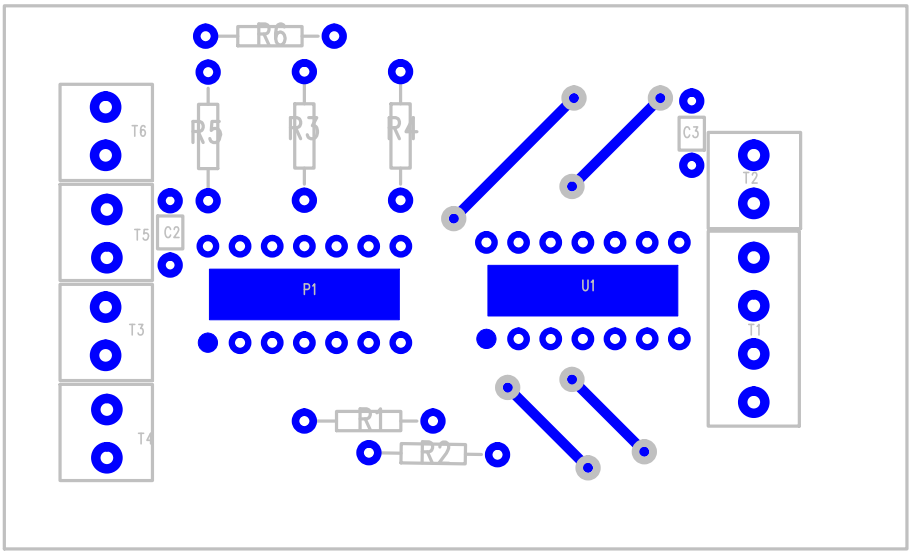

Figure K.1: Load motor control circuit layout top view.

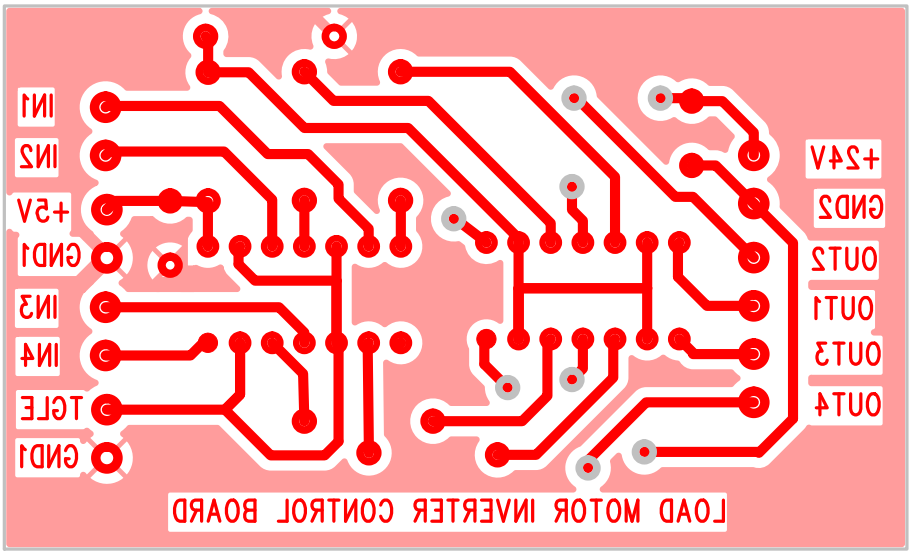

Figure K.2: Load motor control circuit layout bottom view.

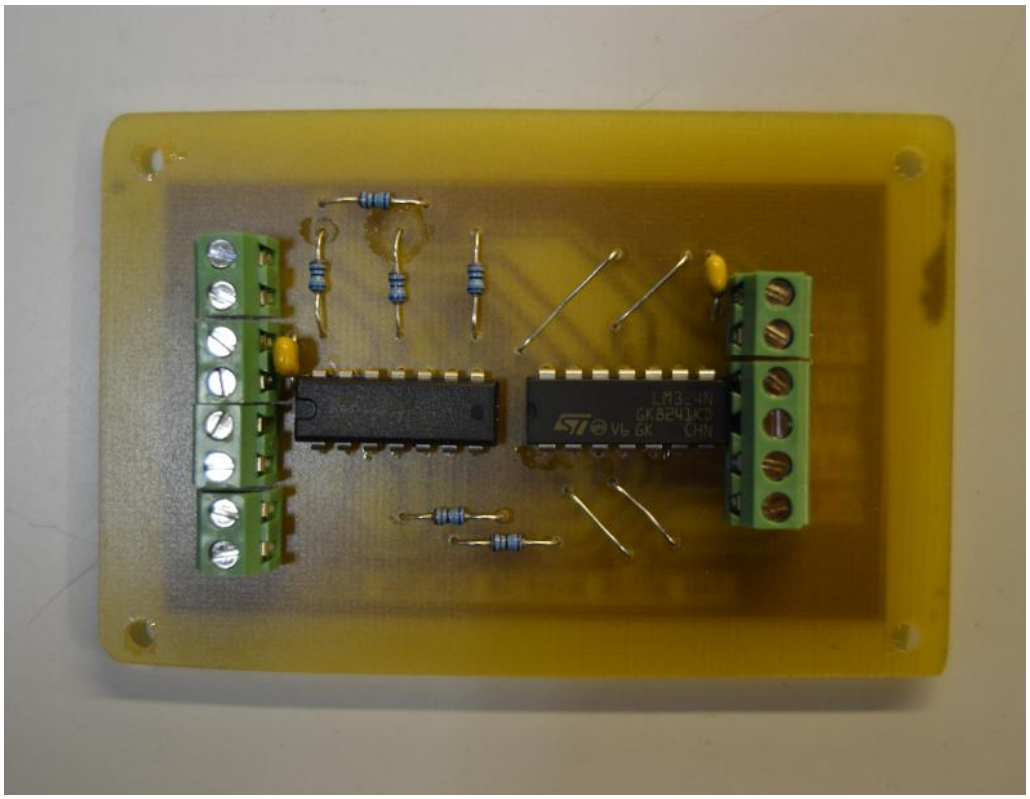

Figure K.3: Soldered and finished load motor control PCB.

L. COMPLETE TEST SYSTEM PHOTOGRAPH

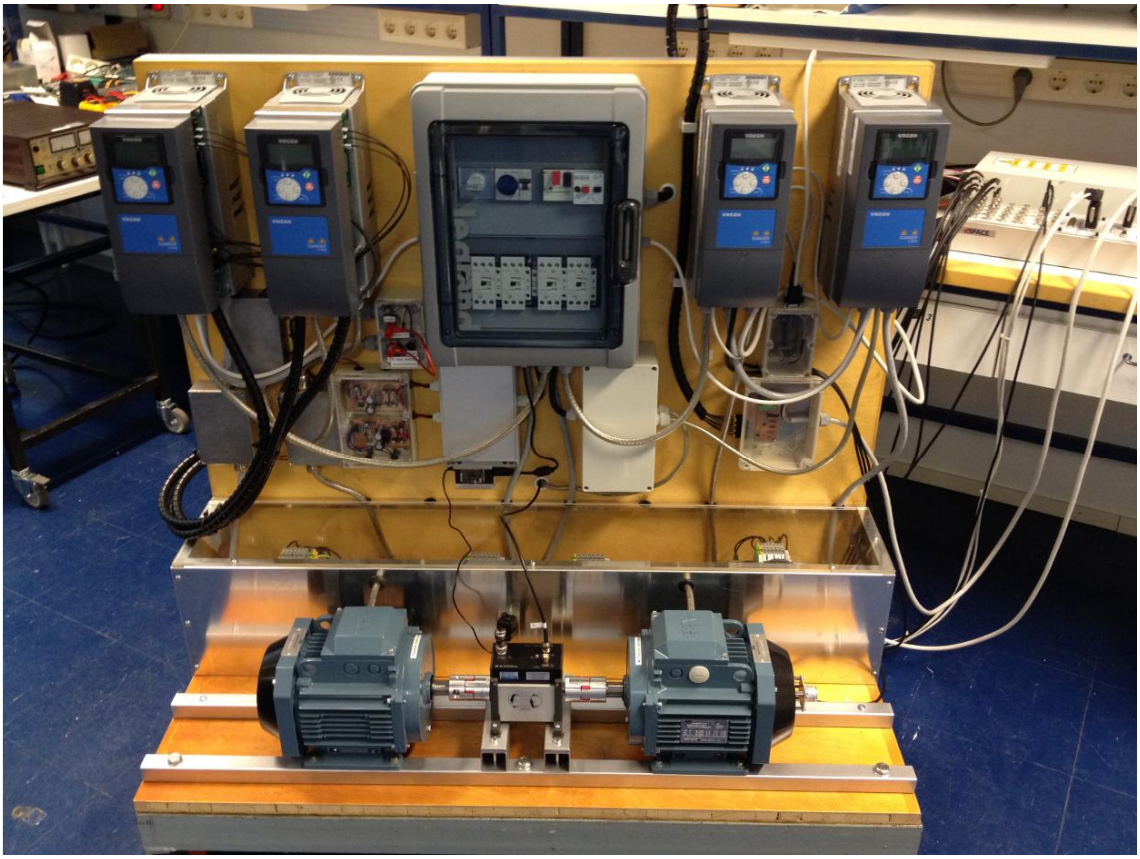

Figure L.1: Completed induction motor test bench including motors, converters, LCL filters and the additional circuits.

Figure L.2: dSPACE DS1103 and CP1103 connector panel.

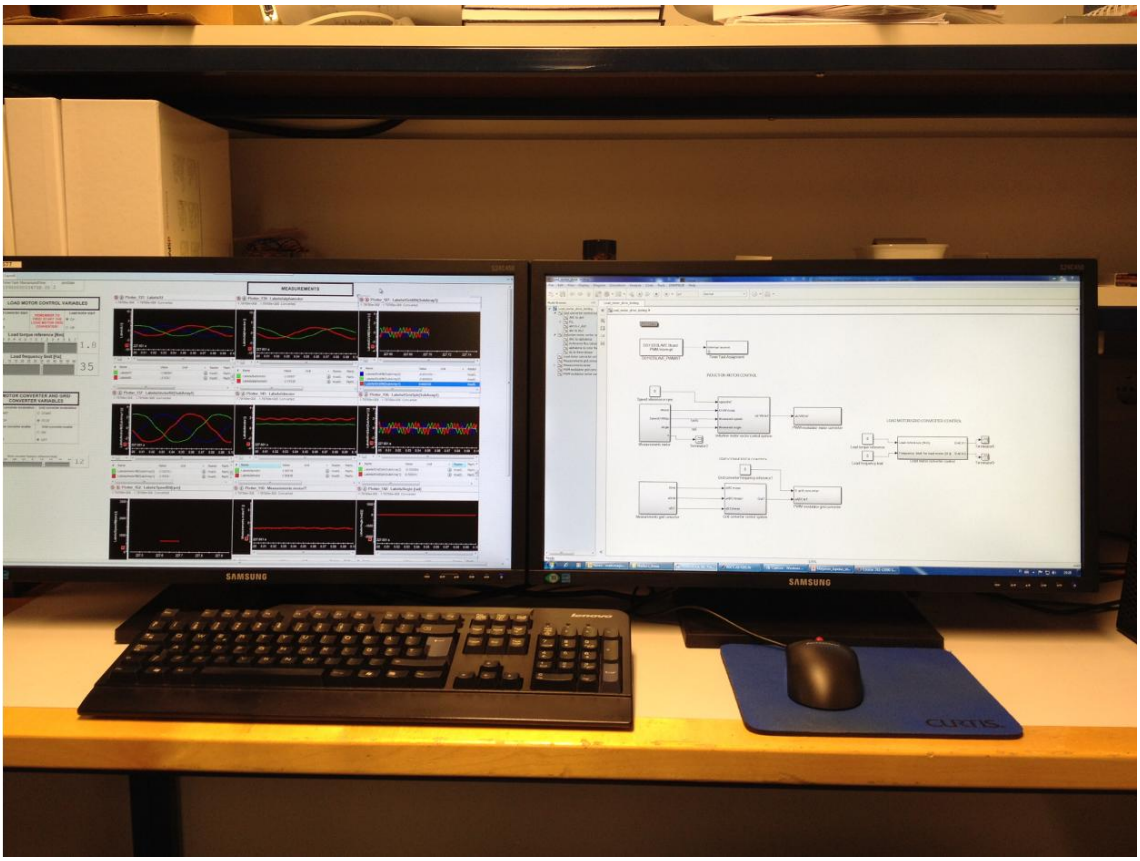

Figure L.3: Induction motor drive test bench PC user interface.